Technische Universität München

Department of Chemistry

Lehrstuhl für Physikalische Chemie

# Development of an experiment for the investigation of intrinsically chiral metal clusters in the gas phase

Kathrin Lange

Vollständiger Abdruck der von der Fakultät für Chemie der Technischen Universität München zur Erlangung des akademischen Grades eines

Doktors der Naturwissenschaften

genehmigten Dissertation.

Vorsitzender: Univ.-Prof. Dr. Ulrich Kaspar Heiz

Prüfer der Dissertation:

1. apl. Prof. Dr. Ulrich Boesl-von Grafenstein
2. Univ.-Prof. Dr. Klaus Köhler

Die Dissertation wurde am 31.07.2014 bei der Technischen Universität München eingereicht und durch die Fakultät für Chemie am 09.09.2014 angenommen.

*„People do their best when they do the thing they love, when they are in their element.*
*The evidence is absolutely persuasive, when people connect to this powerful sense of talent in themselves, discover what it is they can do, they become somebody else."*

Sir Ken Robinson

*„ Life is an ever-flowing process and somewhere on the path some unpleasant things will pop-up-it might leave a scar – but then life is flowing on, and like running water, when it stops, it grows stale.*
*Go bravely on, my friend, because each experience teaches us a lesson. "*

Lee Jun-fa

# Acknowledgements

My thanks are dedicated to all persons who have contributed to the creation of this thesis. In particular I would like to thank Prof. Dr. Ulrich Heiz for giving me this great opportunity and the trust to work on such a highly challenging project. I want to thank him for his support during the last four years and his open mind in many discussions. I want to thank Prof. Dr. Ulrich Boesl for his supervision of my thesis and excellent expertise in regards to laser mass spectrometry.

I have to thank Dr. Martin Tschurl who supported me from the first day in all regards. I respect him for his broad expertise, his will to continue even when nothing is working, his lovely humour and his sense of fairness. I thank him for encouraging me every time I had doubts and guiding me through my thesis, with all the ups and downs, success and failures. He made a large contribution to this work and therefore, I have to thank him a lot. In the same regard I have to thank Dr. Bradley Visser who supervised me in the lab. I thank him for sharing his expertise in experimental work and problem solving with me. With his enormous patience and analytical thinking we were able to overcome many problems. I thank him for pushing me further, even when I thought I was running out of motivation. Thank you for your trust and your friendship.

Daniel Neuwirth and Jan Eckhart also contributed greatly to the creation of my thesis. We worked together on the experiment for so long and I thank them for their working spirit, their teamwork and the ability to support and encourage me. Both are excellent PhD students and I wish them all best for their future, in their professional as well as in their personal life.

I want to thank the whole Heiz group for the great spirit of teamwork and the kind working atmosphere. There was always somebody around to help. This is something very valuable and is unfortunately not a matter of course. Therefore, a big thank you to all of the PhD students.

Without the generous help of the mechanical and electronical workshops this experiment would not have existed. In order to build up an experiment from scratch a reliable workshop is essential. I have to thank all of them putting a lot of working hours and patience in this work. They did a great job.

I have to thank Eduardo Alonso for a lot of philosophical discussions about the work performed as a PhD student. To have somebody as a good friend who understands your work and the process you are going through is a valuable gift. I have the deepest respect for him. Be like water my friend.

Finally I have to thank the persons who have put me into this life, my parents, who never doubted my way and potential. Having such strong family support means a lot to me and helps to overcome almost every critical situation. I thank them for their love and trust. My brother Andreas I want to thank for being such a generous person with an impartial mind. It is great to have you around.

The last thank is dedicated to my best friend Xenia Grosse. We went through a lot of hard times together and I want to thank her for being around no matter for what reasons and when. We have both made our way so far. I am sure we will continue on our ways no matter what other people might think.

# Table of Contents

# 1. Introduction

Clusters are an ensemble of several atoms or molecules which are bound to each other and can exist of various stoichiometries and nuclearities. The term “cluster” was coined in the 1960s and referred mainly to metal-metal bond containing species.[1] Metal clusters can comprise a few metal atoms up to several thousands, which are also called nanoparticles. Two types of metal cluster are distinguished; a) bare metal clusters and b) ligand stabilised metal clusters. These clusters are at present in the focus of heterogeneous catalysis, as they have a high catalytic potential.[2] Such nanostructures show unique size-dependent catalytic properties which differ considerably from the bulk.[3]

In this chapter a brief overview of the various applications of the metal clusters, bare or ligand stabilised, and their importance in asymmetric heterogeneous catalysis is presented. In the last sub-chapter laser spectroscopy techniques are introduced, which are used to probe chiral organic species. The main aim of this and future work is to apply these spectroscopic techniques to probe chiral metal cluster-complexes, to study their properties and to use them as catalysts in asymmetric heterogeneous catalysis.

## 1.1 Metal clusters in heterogeneous catalysis

Heterogeneous catalytic reactions are in great demand at present and this demand will only increase in the future. Many chemical transformations of fossil resources (methane, oil, coal etc.) into highly relevant products influence and will influence our civilisation.

Catalysts are responsible for the production of 60 % of industrial chemicals[4] and therefore, have a significant meaning for the economy. But more importantly, especially for the future, is the development of green chemistry, which promises a strategy in addressing environmental issues. If a catalyst can be the key step to achieve these ambitious aims, a well developed strategy is required to guarantee high selectivity of the reactions. Metal nanoparticles could be one potential catalyst that could be used in such catalytic reactions.

In many cases industrial catalysts contain an active component in the form of metal nanoparticles with sizes smaller than 20 nm. The catalytic activity of such nanostructures and clusters has stimulated strong attention in their synthesis and characterisation, which is today an integral part of nanoscience.[4] The two main goals of investigations in the field of nanoparticle-driven catalysis are: at first the fundamental understanding of the structure and reactivity of such structures and secondly the implementation of this knowledge in future heterogeneous catalyst design.[4]

Important fields of applications for nanoparticles or clusters in catalysis are **dehydrogenation**, **hydrogenation** and **oxidation reactions**. In many reactions noble metal catalysts or transition metal catalysts are used.

*McCrea and Somorja et. al*.[5] presented results of hydrogenation and dehydrogenation rates of cyclohexene dependent on the symmetry of the platinum single crystal face. Hydrogenation was increased on Pt(111) and decreased on Pt(100) compared to dehydrogenation. A mechanistic difference could have led to these results. This is a first good example to underline the high potential of nanostructures that influence reaction pathways by their unique geometric structures. In the same group a first preparation of well-defined shaped metal nanoparticles embedded in ordered mesoporous silicas was performed. For platinum three different structure types were found, cubic with (100), tetrahedral with (111) and cubo-octahedral with both types of faces. This leads to a new approach of specific particle design which has a high relevance for catalysis. *Wilson et al.*[6] studied the size related reactivity of palladium nanoparticles (1.3 – 1.9 nm) in the hydrogenation of allyl alcohols. It was demonstrated that hydrogenation rates depended on the particle diameter. For diameters smaller than 1.5 nm the size effect is driven by the electronic properties, whereas for larger particles the geometric structural differences dominated the size effect.[6] Geometric dependent effects were also found in homogeneous catalysis. The famous Heck[7] and Suzuki[8] coupling reactions showed a dependence on the structure of the utilised colloidal palladium catalyst.

A very interesting phenomenon was found for the oxide-surface promoted alkene hydrogenation. Vanadium complexes showed a self-dimerisation that led to the formation of a unique chiral conformation.[9] By using these vanadium complexes for asymmetric

coupling reactions like 1,1-binaphtol, a 100 % selectivity of the product was obtained. Instead, the monomer species was found to be completely inert to this reaction.

Studies on $Au^0$-nanocolloids which showed a high chemoselectivity in hydrogenation reactions of α, β-unsaturated aldehydes and ketones to allylic alcohols, were performed by *Mertens et al.*[10] Colloids with nearly spherical structure and diameters of 7 nm displayed the highest allyl alcohol yields. Even higher reactivity was found for $Pt^0$ and $Rh^0$.[10] The selective hydrogenation of dienes is an important process in heterogeneous catalysis as dienes are unwanted by-products of thermal cracking of petroleum cuts. For example 1,3-butadiene would be preferentially transformed into 1-butene in the course of polymer production or into 2-butene for petrochemical production. Studies on model catalysts have shown that Pd(110) was observed to have a higher selectivity for the formation of butane than Pd(111).[4]

The third important class of catalytic reactions are oxidation reactions. This field shows the most promising potential for green chemistry processes. For reactions like CO oxidation or propylene epoxidation, gold is a favourable metal to be used as it becomes highly reactive for particle sizes between 1.5-3 nm.[4] Gold clusters with 55 atoms are efficient and robust catalysts for selective oxidation of styrene without any co-oxidant. These “magic number” clusters are suggested to be highly stable which makes them suitable for applications in catalysis.[4] Additionally to monometallic catalysts, bimetallic catalysts can also be used and in the case of Pd-Au they show an even higher activity than the corresponding monometallic catalysts.[4]

Noble metal and transition metal particles have been employed in a wide range of catalyst driven reactions, as presented previously. These nano-sized structures are useful in a large variety of potential catalytic systems due to their electronic and geometric structures. Many of the investigated catalysts are highly selective in the target reactions. For future research it will be highly important to fully understand the nature of these catalytically active complexes to be able to predict specifically the catalytic behaviour under realistic conditions.[4]

## 1.2 Chiral metal clusters in heterogeneous catalysis

The development of a heterogeneous catalyst for the enantiopure conversion of a prochiral reactant is extremely important for the chemical and pharmaceutical industries[11] for the production of highly pure products. However, applications in optoelectronics and electronics are additionally possible.[12]

For the preparation of catalysts containing small and highly stable metal nanoparticles various stabilizers (amines, phosphines etc.) were utilised.[12] For the creation of chiral catalysts the metal-nanoparticle can be modified by adsorption of a chiral organic compound. These chiral nanoparticles are used in numerous relevant heterogeneous enantioselective reactions including: a) hydrogenation of α-keto esters over supported platinum catalysts[13] and the dehydrogenation of β-keto esters over supported nickel catalysts.[14] Enantioselectivity is only obtained when the metal-nanoparticles were modified with a chiral compound. For the dehydrogenation of α-keto esters, cinchona alkaloids[13] were used and for the dehydrogenation of β -keto esters, α-hydroxy acids or α-amino acids[14] were used.

Carbon-carbon bond-forming reactions are also an important field in asymmetric catalysis. The most famous reaction of this type is the Suzuki-Miyaura coupling reaction. This reaction is catalysed by palladium nanoparticles which are stabilised with chiral ligands such as 1,1′-binaphthyl derivates or mono-and bisphosphines. Enantioselective excesses of over 95 % have been obtained using this method. [15]

To understand the transfer of chiral information from the modifier to the metal surface, studies were performed on Cu(110) with adsorbed *R,R*-tartaric acid. It was found that under certain experimental conditions the 2-dimensional order of the *R,R*-tartaric acid adlayer destroyed all symmetry elements at the copper surface to create an extended chiral surface.[11] In other studies it is described that the adsorption of chiral compounds lead to a local chiral environment near the metal surface, which might leave a “chiral footprint” on the metal surface.[16] Chirality might also be transferred onto the electronic structures.[17] *Bürgi et al.*[16] studied small gold nanoparticles protected with *N*-isobutyryl-D-cysteine/*N*-isobutyryl-L-cysteine to investigate their optical activity in the infrared (IR) and ultraviolet-visible (UV-Vis). Additionally vibrational circular dichroism (VCD) spectra were recorded. Density functional theory (DFT) calculations were performed, which revealed that the VCD

spectra show a strong dependence on the conformation of the adsorbed *N*-isobutyryl-cysteine. It is believed that the carboxylic acid group of *N*-isobutyryl-cysteine interacts with the gold nanoparticle. This leads to a two point interaction which causes a "chiral footprint" on the metal surface and therefore the observed optical activity. [16]

The preparation of a chiral catalyst from the adsorption of chiral organic compounds on achiral metal particles and surfaces is one possibility to create an enantioselective system for asymmetric catalysis. The other possibility is based on the structure of metal surfaces and clusters that show inherently chiral features. For example an Ag (643) surface is intrinsically chiral and undergoes different interactions with enantiomers of chiral compounds.[18] As gold nanoparticles are of general interest in catalysis, especially because of their interesting size effects in CO oxidation,[2] many groups have performed DFT calculations on various gold cluster sizes. *Kappes et al.*[19] used various methods (i.e. trapped ion electron diffraction, photo-electron spectroscopy and time dependent DFT) to investigate the geometric structures of gold cluster ions. The results obtained suggest that the lowest energetic structure of $Au_{34}^-$ was potentially chiral, with $C_3$ point symmetry. In this case the chirality arises due to the helical arrangement of the edge atoms (see Figure 1.1).[19] Other studies indicated several more potential intrinsically chiral gold clusters, i. e. $Au_{32}^-$, $Au_{55}^-$, and $Au_{64}^-$, due to their low or even zero symmetry.[20]

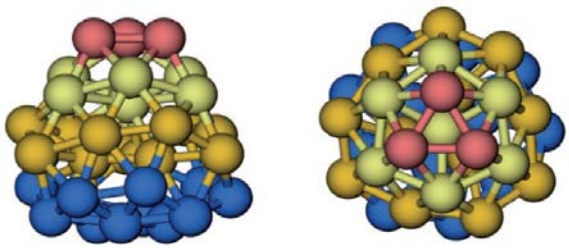

**Figure 1.1:** *Minimum energy structure of $Au_{34}^-$ with $C_3$ symmetry calculated with DFT.*[19]

The relevance of these intrinsically chiral clusters in nanotechnology and catalysis will be driven by the capability to separate enantiomers from racemic mixtures of chiral clusters. The development of a highly selective analysis method is demanded and not trivial to obtain. Once the development succeeds, access will be given to new strategies, which homogeneous asymmetric catalysis cannot achieve.

## 1.3 Probing chirality by laser spectroscopy in the gas phase

Chiral recognition is a fundamental process in life sciences. In the field of heterogeneous catalysis, the differentiation of enantiomers is in great demand, as described earlier in this chapter. Several methods were developed over the last decades which offer a good approach for the chiral recognition of different organic compounds. *Boesl et al.*[21] and *Compton et al.*[22] performed multiphoton ionisation with circularly polarised laser light in combination with mass spectrometry in the investigation of chiral molecules (i.e. camphor or 3-methylcyclopentanone). This experimental method is called circular dichroism (CD) resonance-enhanced multiphoton ionisation (REMPI) and is a powerful tool for mass-selective probing of chirality.[21] The CD effect discriminates between two enantiomers of chiral compounds by the different adsorption strengths of both handednesses of circularly polarised light. This difference in adsorption is called circular dichroism. REMPI allows species selectivity by laser wavelength (mostly UV) and molecular mass. The asymmetry g-factor is a quantity that specifies the extent of the CD for a system and is determined from the measured ion currents for left and right polarised light.[21]

With CD in combination with REMPI, enantiomers can be analysed and mass information is simultaneously obtained. Complexes consisting of two chiral species are called diastereomers and have different chemical and physical properties, e.g. ionisation threshold and spectral shift. This is in counterpoint to enantiomers, which differ only in the adsorption behaviour of circularly polarised light. Studies on the discrimination between diastereomers were performed by *Speranza et al.*[23] and *Zehnacker et al.*[24] This group studied chiral recognition of molecular complexes consisting of chiral monofunctional alcohols ((R)-2-butanol, (S)-2-pentanol) and a chiral chromophore ((R)-1-phenyl-ethanol) in the gas phase by REMPI spectroscopy combined with time-of-flight mass spectrometry (TOF-MS). As only one enantiomer of the chromophore was used (R), two different complexes were created with the alcohols (RR or RS configuration). The diastereomeric complexes were ionised by one-colour resonant two-photon adsorption and their fragmentation patterns were analysed by TOF-MS. At first the differentiation of the chiral monofunctional alcohols was realised by using the different spectral shifts of the band origin of the molecular complexes (alcohol plus chromophore) relative to that of the bare chromophore ((R)-1-phenyl-ethanol). A spectral blue-shift occurs due to the complexation of the chromophore which leads to an

increased stabilisation of the ground state with respect to the excited state in the complex. This shift can be assigned to repulsive interactions between the chromophore and alcohol. A red-shift occurs due to a decreased stabilisation of the ground state and is assigned to attractive interactions between chromophore and alcohol. The work was then extended to differentiation of the chiral monofunctional alcohols using the differing fragmentation patterns of the diastereomeric adducts.[23]

In this chapter the preparation and applications of chiral metal clusters were presented. Research into the intrinsic chirality of metal clusters is important as clear experimental evidence of the existence of these species is still missing. The established spectroscopic techniques presented here, can build the basis for applications on metal cluster containing complexes. Instead of a chiral alcohol, a chiral cluster can be complexed by a chiral chromophore. The resulting diastereomers potentially show spectral differences in REMPI experiments and allow enantio-selective discrimination of these chiral metal clusters. CD-REMPI may help to identify the handedness of the produced chiral clusters and possible chiral products of asymmetric catalysis. It was the aim of the present work to construct an experiment in which chiral metal clusters can be produced, identified and used to perform enantioselective reactions in the gas phase.

# 2. Theoretical background

## 2.1 Time-of-flight mass spectrometry

A time-of-flight mass spectrometer (TOF-MS) accelerates ions from a so called ion source (spatial position of the ion extraction) to a detector (in most cases micro channel plates) where the ions arrive separated in time according to their mass ***m*** to charge ***q*** ratio.[25] TOF-MS instruments work in pulsed mode. High potential differences applied to the TOF electrodes, cause the acceleration of the ions.[26] By using constant acceleration fields all ions formed at one position obtain the same kinetic energy.[26] After leaving the acceleration field the ions pass through a field-free drift region and arrive at the detector after a time that depends on their velocity. The ion velocity is reciprocally proportional to the mass/charge ratio as shown in Equation 7[26] Therefore, lighter ions arrive sooner at the detector than heavier ones. The basis of the theoretical descriptions given here is a publication of *Boesl et al.*[27] In a TOF-MS with an ion source consisting of two electrodes and a linear drift tube the total flight time is given by the sum of acceleration time $t_A$ and the drift time $t_B$ in the field free region:

$$t = t_A + t_B \tag{1}$$

If the field in the ion source $E_A$ is considered to be homogeneous, then the kinetic energy $E_{kin,A}$ of the ions can be expressed such that:

$$E_{kin,A} = m \cdot a \cdot x_A = qU \tag{2}$$

with $m$ as the ion mass, $a$ as the acceleration, $x_A$ as the ion path length in the acceleration field, $q$ as the elementary charge and $qU$ the final kinetic energy of the ion. The ion path length is defined as:

$$x_A = \frac{1}{2} \cdot a \cdot t_A^2 \tag{3}$$

with $a$ as a constant ($a = \frac{qU}{mx_A} = \frac{qE_A}{m}$) due to the assumed homogeneous field $E_A$.

From Equation 3 the time which the ions spend in the acceleration region can be derived as:

$$t_A = \sqrt{\frac{2x_A}{a}} = \sqrt{\frac{2x_A m}{qE_A}} = 2x_A\sqrt{\frac{m}{2qU}} \quad (4)$$

With $x_A$ the flight path in the acceleration region, $m = M \cdot m_p$, $M$ as the ion mass in atomic mass units, $m_p$ as the proton mass. By substitution of $m$ the following equation results:

$$= 2x_A\sqrt{\frac{Mm_p}{2qU}} = 2x_A C\sqrt{\frac{M}{U}} = 2C\sqrt{x_A}\sqrt{\frac{M}{E_A}} \quad (5)$$

with *C* as a constant ($C = \sqrt{\frac{m_p}{2q}} = 0.71986\mu s V^{1/2} cm^{-1}$ ) for singly-charged ions.

The kinetic energy $E_{kin,D}$ of the ions in the field-free drift region remains constant and is given by Equation 6:

$$E_{kin,D} = \frac{1}{2}m \cdot v^2 = qU \quad (6)$$

Thus the velocity of the ions in this region also remains constant:

$$v = \sqrt{\frac{2qU}{m}} \quad (7)$$

The velocity $v$ is equal the length of the ion path in the drift region $x_D$ divided by the time $t_D$ the ions need to travel this length. Therefore, the time ions spend in the field-free drift region can be described by:

$$t_D = \frac{x_D}{v} = x_D\sqrt{\frac{m}{2qU}} \quad (8)$$

$$= x_D \sqrt{\frac{M m_p}{2qU}} = x_D C \sqrt{\frac{M}{U}} = x_D C \sqrt{\frac{M}{x_A E_A}} \quad (9)$$

The mass resolution of a TOF-MS is limited by the uncertainty in the time of flight, which consists of three contributions: the initial temporal, spatial and velocity distributions of the ions. The temporal distribution corresponds to the finite time of ion formation and originates from a finite ionisation laser pulse length. Independent of the mass of the ion, the temporal uncertainty remains constant across the entire mass range. By laser ionisation a reduction in the temporal distribution could be achieved by using shorter laser pulses. In the case of pulsed ion extraction a temporal distribution may also be caused by the temporal behaviour of the high voltage pulse. The second contribution is caused by the laser focus size which influences the volume of ion formation. This spatial distribution causes a difference in ion potential energies for ions of the same mass. Therefore, the kinetic energies differ after acceleration, which leads to different times of flight.

The component of the uncertainty in the time of flight caused by the spatial distribution $\Delta x_A$ can be separated into two fractions, the acceleration fraction:

$$\frac{dt_A}{dx_A} = \frac{d}{dx_A} \sqrt{\frac{M x_A}{E_A}} 2C = \frac{1}{2} x_A^{-1/2} \sqrt{\frac{M}{E_A}} C = \frac{1}{2} \frac{t_A}{x_A} \quad (10)$$

and the drift region fraction:

$$\frac{dt_D}{dx_A} = \frac{d}{dx_A} x_D \sqrt{\frac{M}{E_A x_A}} C = -\frac{x_D}{2} x_A^{-3/2} \sqrt{\frac{M}{E_A}} C = -\frac{1}{2} \frac{t_D}{x_A} \quad (11)$$

The sum $\Delta t_{sum}$ of both fractions equals the total uncertainty in time of flight caused by spatial distribution:

$$\Delta t_{sum} = \left(\frac{1}{2} t_A - \frac{1}{2} t_D\right) \frac{\Delta x_A}{x_A} \approx -\frac{1}{2} t_D \frac{\Delta x_A}{x_A}; \quad t_D \gg t_A \quad (12)$$

A minimisation of the influence of the spatial distribution could be achieved through the use of a smaller laser focus and a weaker extraction field. A so-called first order space focus which is described later can additionally help to minimise the uncertainty.

The third relevant contribution for the uncertainty in the time of flight is the initial velocity distribution, which causes a pseudo displacement of the ions. The initial velocity distribution can be divided into a pseudo-spatial and a pseudo-temporal effect. The pseudo-spatial effect leads to different kinetic energies of the ions after they have been accelerated. The initial velocity causes a velocity distribution $\Delta v_i$ of the ions in the ion source of the TOF-MS. This corresponds to an additional potential energy $U_i$ of the ions, which can be presented by an energy difference due to a pseudo-spatial distribution $\Delta x_i$:

$$U_i = \frac{1}{2} m \cdot \Delta v_i^2 = \Delta x_i q E_A \qquad (13)$$

The pseudo-spatial uncertainty is given by:

$$\Delta t = -\frac{1}{2} t_D \cdot \frac{\frac{1}{2} m \Delta v_i^2}{q E_A x_A} = -\frac{1}{2} t_D \frac{U_i}{U} \qquad (14)$$

The pseudo spatial uncertainty can be minimised similarly to the uncertainty in time of flight caused by the normal spatial distribution by using a first-order space focus. The use of a supersonic expansion also reduces the pseudo-spatial contribution. However, it is not sufficient to describe the effect of a velocity distribution by a contribution to ion kinetic energy or pseudo-spatial effect, respectively. Also the pseudo-temporal effect has to be included, which is defined by:

$$\Delta t = 2\frac{\Delta x_i}{\Delta v_i} = 2\frac{\frac{1}{2} m \Delta v_i^2}{q E_A \Delta v_i} = \pm 2 \frac{\sqrt{\frac{1}{2} m}\sqrt{\frac{1}{2} m \Delta v_i}}{q E_A} = \pm 2 C \frac{\sqrt{M U_i}}{E_A} \qquad (15)$$

As Equation 15 shows, this effect is reduced by using a strong extraction field $E_A$in the ion source.

The **first-order space** focus (SF) is a point in the drift region where ions of equal mass but formed at different positions in the ion source, arrive at the same time. At this point the linear term of the energy spread *ΔU* vanishes. Ions that start further towards the repeller electrode have a higher kinetic energy, arising from a higher potential energy ($\Delta U = \Delta x q E$). For ions with lower kinetic energies the acceleration length is shorter. Due to this relation all ions of equal mass arrive simultaneously at the first-order space focus. At this point in a two electrode ion source the effect of the spatial distribution disappears:

$$\frac{dt}{dx_A} = \left(\frac{1}{2}\frac{t_A}{x_A} - \frac{1}{2}\frac{t_D}{x_A}\right) = \frac{1}{2x_A}(t_A - t_D) = 0 \qquad (16)$$

with $t_A = 2x_A C\sqrt{\frac{M}{U}}$ and $t_D = x_D C\sqrt{\frac{M}{U}}$ Equation 17 results:

$$= \frac{1}{2x_A}\left(2x_A C\sqrt{\frac{M}{U}} - x_D C\sqrt{\frac{M}{U}}\right) = 0\,;\;\; x_D = 2x_A = x_{SF} \qquad (17)$$

The position of the space focus is fixed at $2x_A = x_{SF}$ for a single stage ion source. The short drift region and acceleration distances of $x_A + x_{SF}$ result in a low mass resolution. In order to change $x_{SF}$ and improve resolution of the TOF-MS a second electric field is used. Figure 2.1 illustrates the difference between one-stage and two-stage ion source.

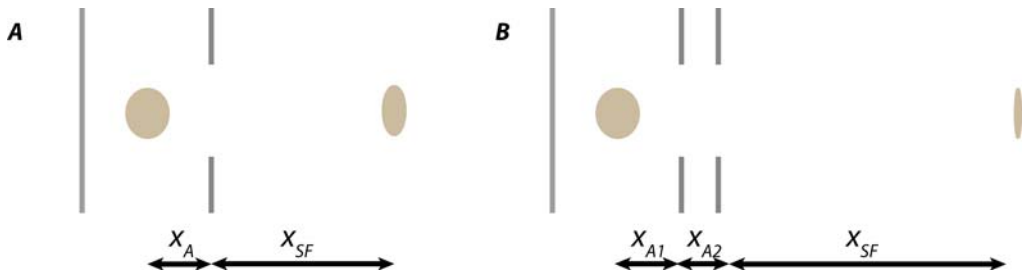


**Figure 2.1:** *First-order space focus of single stage (A) and two stage (B) ion source.*

To define the position of the first-order space focus in a two-stage ion source, the spatial distribution, which leads to an uncertainty in time of flight, has to be taken into consideration. Depending on the voltages applied to the electrodes, the time durations

which the ions spend in the first and second acceleration region ($t_{A1}$,$t_{A2}$) and up until the space focus ($t_{SF}$), are defined as:

$$t_{A1} = 2x_{A1}C\sqrt{\frac{M}{U_{A1}}} = 2C\sqrt{x_{A1}\frac{M}{E_{A1}}} \;;\; U_{A1} = U - U_{A2} \tag{18}$$

$$t_{A2} = 2x_{A2}C\frac{\sqrt{U_{A1}+U_{A2}}-\sqrt{U_{A1}}}{U_{A2}}\sqrt{M} \tag{19}$$

$$= 2C\frac{\sqrt{x_{A1}E_{A1}+U_{A2}}-\sqrt{x_{A1}U_{A1}}}{E_{A2}}\sqrt{M} \tag{20}$$

$$t_{SF} = x_{SF}C\sqrt{\frac{M}{U}} = x_{SF}C\sqrt{\frac{M}{x_{A1}E_{A1}+U_{A2}}} \tag{21}$$

By using these equations to express the contributions for the uncertainty in time of flight, the following terms result:

$$\frac{dt_{A1}}{dx_{A1}} = \frac{d}{dx_{A1}}2C\sqrt{x_{A1}\frac{M}{E_{A1}}} = \frac{1}{2}\frac{t_{A1}}{x_{A1}} \tag{22}$$

$$\frac{dt_{A2}}{dx_{A2}} = \frac{d}{dx_{A1}}2C\frac{\sqrt{x_{A1}E_{A1}+U_{A2}}-\sqrt{x_{A1}U_{A1}}}{E_{A2}}\sqrt{M} \tag{23}$$

$$= \frac{1}{2}t_{A2}\frac{E_{A1}}{\sqrt{(x_{A1}E_{A1}+U_{A2})(x_{A1}U_{A1})}} \tag{24}$$

$$\frac{dt_{SF}}{dx_{A1}} = \frac{d}{dx_{A1}}x_{SF}C\sqrt{\frac{M}{x_{A1}E_{A1}+U_{A2}}} = -\frac{1}{2}t_{SF}\frac{E_{A1}}{x_{A1}E_{A1}+U_{A2}} \tag{25}$$

Analogous to Equation 16, all ions of equal mass arrive simultaneously at the first-order space focus and therefore, the spatial distribution disappears:

$$\frac{dt}{dx_A} = \frac{dt_{A1}}{dx_{A1}} + \frac{dt_{A2}}{dx_{A2}} + \frac{dt_{SF}}{dx_{SF}} = 0 \qquad (26)$$

An expression for the distance to the first-order space focus is given by:

$$x_{SF} = \frac{U^{3/2}}{(U - U_{A2})^{3/2}} x_{A1} - \frac{U^{3/2}}{(U - U_{A2})^{1/2} U_{A2}} x_{A2} + \frac{U}{U_{A2}} x_{A2} \qquad (27)$$

Equation 27 shows directly that the first order space focus distance depends strongly on the applied voltages. To achieve a high resolution, ideally a very long space focus would be used, which requires a small potential difference in the first acceleration stage. A low potential difference in the ion source enhances the effects of space charge and the time of flight spread increases. The pseudo-temporal distribution, which contributes to the uncertainty in the time of flight, can be reduced by applying a high extraction field. Otherwise, using a weak extraction field reduces the effect of the spatial distribution by increasing the time of flight to the space focus. By using a reflectron both issues can be overcome. In a reflectron high extraction fields can be employed while simultaneously increasing the time of flight.

With a second-order space focus a further time compression of the ion cloud can be achieved (see Figure 2.2). By using a specific set of potentials not only the linear but also the quadratic term of the energy spread *ΔU* vanishes.

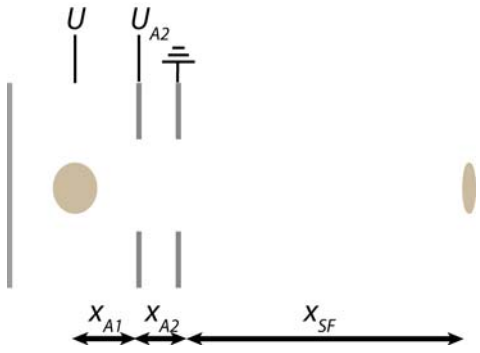


**Figure 2.2:** *Second-order space focus in a two stage ion source causes a stronger compression of the ion cloud.*

## 2.2 Laser induced photoionisation

Photoionisation is based on the ejection of an electron from a neutral species caused by irradiation of atoms or molecules. This process was firstly observed on surfaces of alkali metals by Hertz and was called the photoelectric effect.[28] It was shown that the energy of a photon $hv$, which initiates the irradiation, is equal to the kinetic energy of the ejected photoelectron plus the work function $\phi$ of the metal surface (Equation 28) or plus the ionisation potential IP of an atom/molecule (Equation 29):

$$hv = \frac{1}{2} m_e v^2 + \phi \quad (28)$$

$$hv = \frac{1}{2} m_e v^2 + IP \quad (29)$$

with $m_e$ the mass of an electron and $v$ the electron velocity. Ionisation of alkali metal surfaces can be achieved by using ultraviolet laser irradiation, as the work functions are only in the order of a few electron volts.

Photoionisation processes, which lead to a singly charged $M^+$ species are predicted by a simple selection rule which allows all ionisation pathways. A more detailed description of the selection rules is presented in the following chapter as the same rules apply for photodetachment processes.

For the ionisation of an atom ($A$, Equation 30) or molecule ($M$, Equation 31):

$$A + hv \rightarrow A^+ + e^- \quad (30)$$

$$M + hv \rightarrow M^+ + e^- \quad (31)$$

the energy which is required to eject one electron can be seen as a direct measurement of the orbital energy from which the electron originated. This assumption is known as Koopmans theorem. As orbitals are only based on theoretical concepts, their energy values can only be obtained by theoretical calculations. Calculations for high-electron systems start

to become very complex. In this case experimental values of ionisation potentials show the closest measurable quantities to the orbital energies.[28]

## 2.3 Laser induced photodetachment

The fundamental concept of ejecting electrons in electron photodetachment and photoionisation is the same and was taken from J. M. Hollas *Modern Spectroscopy*.[28] However, in this case an electron is ejected from an anionic species which leads to the formation of a neutral species and a free electron:

$$M^- + h\nu \rightarrow M + e^- \qquad (33)$$

Electron affinity (vertical electron affinity, see Figure 2.3) is defined as the energy gain caused by electron attachment, which equals the minimum energy that is needed to eject one electron from an anion. Depending on the process and the involved molecular state in which the molecule is excited into, three different EAs can be differentiated: the adiabatic electron affinity (AEA), vertical electron affinity (VEA) and vertical detachment energy (VDE). All three are illustrated in Figure 2.3.

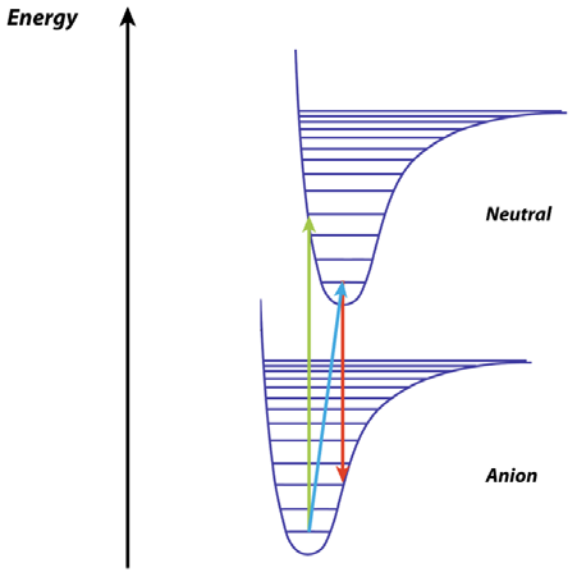


**Figure 2.3:** *Adiabatic electron affinity (blue line), vertical electron affinity (red line) and vertical detachment energy (green line).*

The adiabatic electron affinity corresponds to the 0→0 transition between anion and neutral molecule. The most probable transition starting from the anionic ground state is the vertical transition or VDE, based upon the Franck-Condon principle. The value for the VDE is always higher or the same as the value for AEA. In contrast to the adiabatic electron affinity, the vertical electron affinity involves the attachment of one electron to a neutral molecule. The value of VEA is always lower than or equal to the AEA. If the geometries of both states (anion and neutral) do not differ considerably, the vertical transitions equal the adiabatic electron affinity. Thus, in this case the adiabatic transition is the most intense one.

The selection rules for an allowed photodetachment transition are the same as for photoionisation.[29] A brief description with several key simplifications is given in the following paragraphs. The simplifications are useful to reduce the complexity of the photodetachment process, but still allow a good understanding of the bands appearing in photodetachment spectra. The simplifications involve: **a)** the validation of the Born-Oppenheimer approximation, which enables the separate treatment of the electron and nucleus wave functions and **b)** neglect of the spin-orbital coupling. For this reason, only the overlap of the wave functions has to be considered. Due to these simplifications the transition dipole moment is given by:

$$\vec{M} = \left\langle \psi'_e(r;R) \middle| \sum_{\mathrm{i}} \hat{\mu}_{\mathrm{e}} \middle| \psi''_e(r;R) \right\rangle \langle \psi'_v(R) | \psi''_v(R) \rangle \langle \psi'_s | \psi''_s \rangle \qquad (34)$$

with $\psi'$ as the wave function for the ground state (anion), $\psi''$ as the wave function for the excited state (neutral), *r* and *R* are the coordinates of the nucleus and electron movement, and $\hat{\mu}_{\mathrm{e}}$ represents the transition dipole moment operator for the electron transition. This operator also counts as a single-electron operator and therefore has to be summed over all electrons in the considered system. The indices *e*, *v* and *s* stand for the electronic, vibronic and spin-contributions of the wave function.

From these simplifications the selection rules can be derived. A one electron transition induced by adsorption of one photon from the anion ground state into any neutral state is allowed by symmetry. For an atom the orbital angular momentum of the ejected electron must change by $\Delta l = \pm 1$. As the electron is able to take any orbital angular momentum

from the system upon ejection, transitions to any neutral state are possible. Due to this prediction, the orbital angular momentum of the electron depends upon the angular momenta of the anion and neutral species. For the case of molecules, the symmetries of the molecular orbitals and the photon, influence the symmetry of the electron orbital angular momentum. A two electron excitation would cause an electron-electron coupling, which in turn would create more complex selection rules and is not considered in this work in further detail.

As spin functions with different spins are orthogonal to each other, the anion spin equals the sum of neutral spin plus detached electron spin ($\Delta S$=0). The selection rules for vibrational transitions are only governed by the overlap of the vibrational wave functions. The overlap, or more precisely the overlap integral, is non-zero if the coupling of both states shows a total symmetry. The vibrational ground state of the anion has such a total symmetry. Therefore, any resulting vibration in the neutral species is also predicted to be totally symmetric. Second harmonics of modes of different symmetry are included as well. In conclusion two main selection rules can be proposed:

$$\Delta v = \{0, 1, 2, \dots \quad (35)$$

for total symmetric vibrations and:

$$\Delta v = \{0, 2, 4, \dots \quad (36)$$

for all vibrations.

## 2.4 Metal cluster geometries and electronic properties

The theoretical description of the electronic and geometric structure of transition metal clusters is demanding. Therefore, the combination of experimental and theoretical studies is indispensable in order to interpret experimental data. This is especially true in the case of larger clusters. A variety of data is essential as multiple structural isomers can exist and spin multiplicities lead to minor energetic differences.[30,31] Theoretical predictions can be in good agreement with experimental energy measurements, but often fail to explain other experimental results such as magnetic moments or vibrational spectra.[32]

The electronic properties of metal clusters can be described by the ionisation potential (IP) and electron affinity (EA), both of which are functions of the cluster size. From the atom to the bulk, the IP decreases, whereas the EA increases. Both values are represented by the work function in bulk metals.[33] It was found that over the entire mass range IP and EA scale with $n^{-1/3}$.[33] However, for certain mass ranges this behaviour is not seen and a strong divergence of both values with cluster size was observed. This phenomenon is described as the non-scalable size regime.

## Niobium

Far-infrared absorption spectra of small neutral and cationic niobium clusters ($Nb_n$, n = 5-9) were obtained from multiple photon dissociation spectroscopy of their argon complexes by *Fielicke et al.*[34] The cluster structures were identified by comparison of the experimental and calculated far-IR spectra. The experimental spectra for n= 5,6,8, and 9 showed a significant difference between neutral and cationic clusters. However, theory predicted that the overall geometries for all species except $Nb_6$ were very similar. All considered cluster sizes were determined to have compact three-dimensional structures. Following the removal of one electron due to photon dissociation, no significant changes in the cluster geometries were visible. Overall most niobium cluster geometries are very similar to those of the corresponding vanadium clusters.[34] A common build-up principle for these cluster geometries has still not been identified.

**Table 2.1:** *Calculated lowest energetic structures for neutral and cationic niobium clusters (n =5-9).*

| Number of atoms per cluster | Lowest energetic structures for neutral[a]/cationic[b] clusters |
|---|---|
| 5 | Trigonal bipyramid |
| 6 | Tetragonal square bipyramid[a]/Tetragonal nonsquare bipyramid[b] |
| 7 | Pentagonal bipyramid |
| 8 | Hexagonal bipyramid |
| 9 | Capped hexagon |

*Kietzmann et al.*[35] combined photoelectron spectroscopy measurements with density functional theory (DFT) calculations to determine the structures of anionic niobium clusters (n = 3-8). The clusters showed strongly size dependent spectra and compact low-symmetry 3D structures. For $Nb_8^-$ the coexistence of two isomers under specific experimental conditions was found. The structures inferred from the experimental data were found to match the calculated structures well. Only $Nb_3^-$ and $Nb_5^-$ showed slight variation from theory. Vertical detachment energies (VDE) for $Nb_8^-$ and $Nb_{10}^-$ of slightly less than 1.5 eV were measured, which is 0.2 eV lower than the values obtained for $Nb_7^-$ and $Nb_9^-$.[36] This even-odd alternation in the VDE was found to hold for clusters up to $Nb_{17}$[36] and is analogous to the trend seen for alkali metal clusters.[37] For smaller clusters n < 6, no systematic pattern of the VDEs was observed. The opposite oscillation (even > odd) was found for the ionisation potentials of niobium clusters. Ionisation potentials decreased rapidly from 6.2 eV for Nb to a local minimum of 4.53 eV for $Nb_{15}$ and increased slightly reaching a local maxima at n = 26.[38] Niobium clusters with n = 8, 10, and 16 were found to be considerably inert towards reactions with simple molecules. This high stability corresponded to stable structures due to an electronic or geometric shell closing.[36] The first geometric shell closing seemed to occur for n = 15 with a body centred cubic structure (bcc). There were indications that a general change in electronic and geometric structure occurred at this cluster size.[36] The mentioned values for the corresponding niobium cluster size are shown in Figure 2.4.

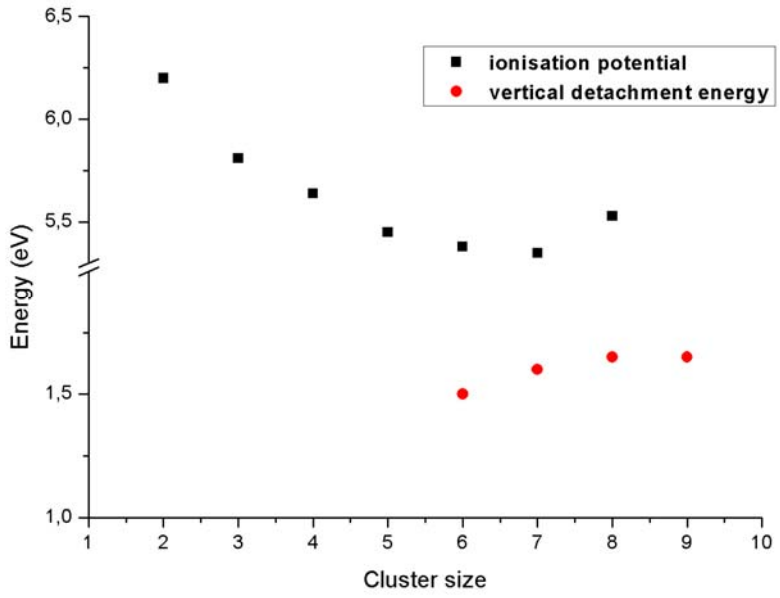


**Figure 2.4:** *Ionisation potentials*[38] *and vertical detachment energies*[36] *plotted against the size of niobium clusters.*

## Tantalum

The geometries and electronic properties of tantalum clusters ($Ta_n$, n =1-3) were studied by *Wu et al.*[39] using DFT calculations. For the neutral tantalum dimer a dissociation energy of 2.87 eV was found, while the dissociation energies for the cation with 4.51 eV and the anion with 4.17 eV were much higher.[39] This indicated that the Ta-Ta bond was strengthened by the addition or removal of an electron, which was also reflected by the formation of a double bond in the cation and a triple bond in the anion. The IP of the neutral dimer was calculated to be 6.15 eV, which was smaller than the value for the tantalum atom of 7.78 eV. The calculated EA (1.05 eV) and IP (5.64 eV) for $Ta_3$ were found to be slightly smaller than those for $Ta_2$. The dissociation energies for the charged species (cation 4.71 eV, anion 4.56 eV) compared to the neutral (4.32 eV) followed the same trend as for the dimer. The lowest energetic structure of the neutral trimer was found to be an equilateral triangle with $D_{3h}$ symmetry.

*Fielicke et al.*[40] investigated vibrational spectra of gas phase cationic tantalum clusters by using infrared multiple photon dissociation (IR-MPD) of their complexes with argon atoms. For many cluster sizes the spectra of cationic clusters showed similar features to the ones of its lighter homologues niobium and vanadium, especially for n = 6, 7, 13, 15 and 17. Cluster growth seemed to follow a similar mechanism. $Ta_6^+$ was predicted as a distorted tetragonal bi-pyramid and $Ta_7^+$ as a distorted pentagonal bi-pyramid. Calculations performed by *Fa et al.*[41] predicted the same geometries for neutral tantalum clusters. $Ta_{13}^+$ was found to be an interesting species as it can form highly symmetric icosahedral or cuboctahedral structures. In a 13- atom cluster twelve atoms can fully surround the central atom, which vibrates against the surrounding cage. $Ta_{15}^+$ was found as the smallest cluster to show a bcc structure. Theory[41] predicted bcc as the most stable structure for the neutral species. The spectrum for $Ta_{17}^+$ gave rise to a Frank-Kasper polyhedra. Spectra for $Ta_n^+$ with n = 8-12, 14, 16 and higher than 17 showed more complicated features. For $Ta_{12}$ two isomers with IPs of 4.35 eV and 4.86 eV [42] were found, but for the cation such an assumption could not be proved, as the spectrum showed only weak peaks. For clusters with more than 17 atoms the spectra became even more complicated. Structural isomers were very likely, however due to the decreasing signal to noise ratio further investigation was impeded.

Ionisation potentials for $Ta_n$ with n = 3-60 were obtained from photoionisation efficiency spectra measured by *Collings et al.*[42] Considerable variations of IPs in the lower size regime from those of theoretical models were found, which indicated that the IPs of a cluster size regime with n < 20 atoms cannot be approximated by a metallic sphere. For clusters > 20 atoms the variation occurred more smoothly with cluster size. The variation between each cluster indicated that the IP was strongly affected by the distinct geometric and electronic structures of the clusters.[42] A list of the measured IPs of $Ta_n$ with n = 1-9 is shown in Chapter 6.1.

Studies on anionic tantalum cluster geometries were limited in literature. *Wang et al.*[43] investigated the electronic structure of $Ta_3^-$ by using photoelectron spectroscopy in combination with DFT calculations. At 355 nm several congested features were observed in the experimental photoelectron spectra, which led to VDEs between 2.03 eV and 2.9 eV. These congested spectral features indicated a high density of electronic states, which was expected for an open-shelled cluster. DFT calculations predicted an equilateral triangle with a $D_{3h}$ symmetry as the ground state symmetry for $Ta_3^-$.

The IP values for the corresponding tantalum cluster size are shown in Figure 2.5.

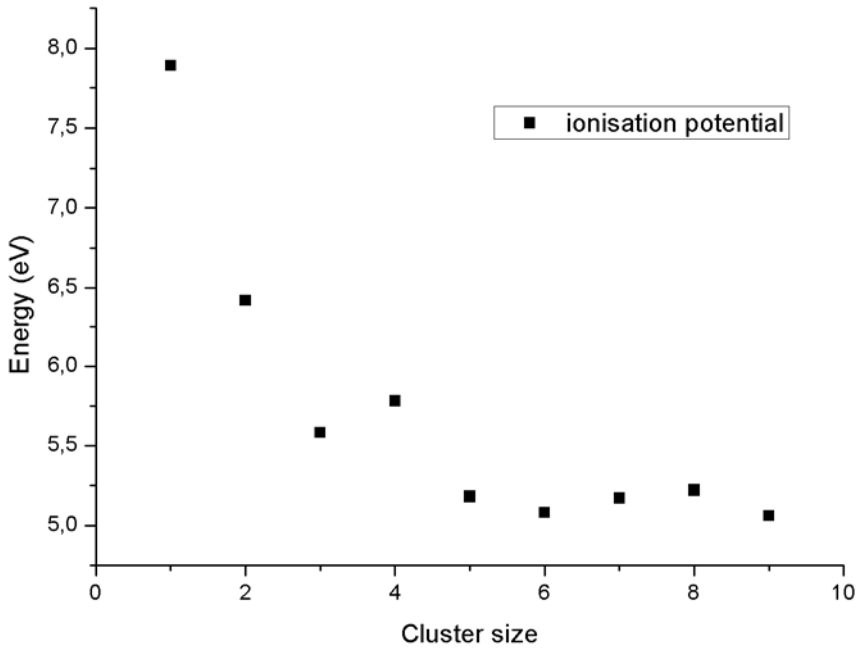


**Figure 2.5:** *Ionisation potentials of tantalum clusters with $Ta_n$, n = 1-9.*[42]

## Rhodium

The geometric structures of cationic rhodium clusters ($Rh_n^+$, n = 6-12) were investigated in the gas phase by far-infrared multiple photon dissociation (FIR-MPD) spectroscopy and density functional theory (DFT) by *Harding et al.*[31] In order to measure the vibrational spectra of bare transition metal clusters argon was used as a messenger. An overview of the calculated lowest energetic structures is presented in Table 2.2.

**Table 2.2***: List of cationic $Rh_n^+$ with n = 6-12 and the corresponding lowest energetic structures calculated by DFT.*

| Cationic rhodium clusters | Lowest energetic structures[31] |
|---|---|
| $Rh_6^+$ | Distorted octahedral |
| $Rh_7^+$ | Distorted pentagonal bi-pyramid |
| $Rh_8^+$ | Bi-capped octahedron |
| $Rh_9^+$ | Trigonal prism |
| $Rh_{10}^+$ | Polytetrahedral |
| $Rh_{11}^+$ | Icosahedral fragment |
| $Rh_{12}^+$ | Capped octahedral |

In general, the clusters were found to favour structures based on octahedral and tetrahedral motifs for most of the considered cluster sizes. In contrast to Harding, Aguilera-Granja *et al.* predicted capped structures with cubic motifs.[44]

Neutral and anionic rhodium clusters (n = 1-9) were investigated by Beltran *et al.*[30] using ab initio calculations and anion photoelectron spectroscopy (PES). The resultant structures for neutral and anionic clusters are shown in Table 2.3. The experimental and calculated values for the adiabatic detachment energy (ADE) and the vertical detachment energy (VDE) differed by less than 0.3 eV for all considered clusters, except the neutral $Rh_7$ cluster. The calculated VDE was 0.54 eV higher than the experimental value. In general, the detachment energies increased non-linearly with cluster size from Rh with a VDE of 1.10 eV up to $Rh_9$ with ADE and VDE of 2.2/2.4 eV. $Rh_2$ showed considerably higher values (1.5 eV ADE/1.65 eV VDE) than $Rh_3$ with 1.0 eV ADE/1.2 VDE and the values of $Rh_4$ were measured to be lower (0.7 eV ADE/0.9 eV VDE) than $Rh_5$.[30]

**Table 2.3:** *Calculated structures for neutral and anionic rhodium clusters (n =1-9).*

| Rhodium clusters | Lowest energetic structures for neutrals and anions[30] |
|---|---|
| $Rh_2$ | Linear |
| $Rh_3$ | Triangular |
| $Rh_4$ | Bent rhombus |
| $Rh_5$ | Triangular bi-pyramid |
| $Rh_6$ | Octahedron |
| $Rh_7$ | Pentagonal bi-pyramid |
| $Rh_8$ | Bi-capped octahedron |
| $Rh_9$ | Capped anti-prism |

Calaminici *et al.*[45] performed DFT calculations on $Rh_{13}$ in order to study the ground state structure. A biplanar-like structure with $C_1$ symmetry was found. The result was in good agreement with the experimental value of the magnetic moment and was supported by X-ray magnetic circular dichroism measurements.[45] The values of ADE and VDE for the corresponding rhodium cluster size are shown in Figure 2.6.

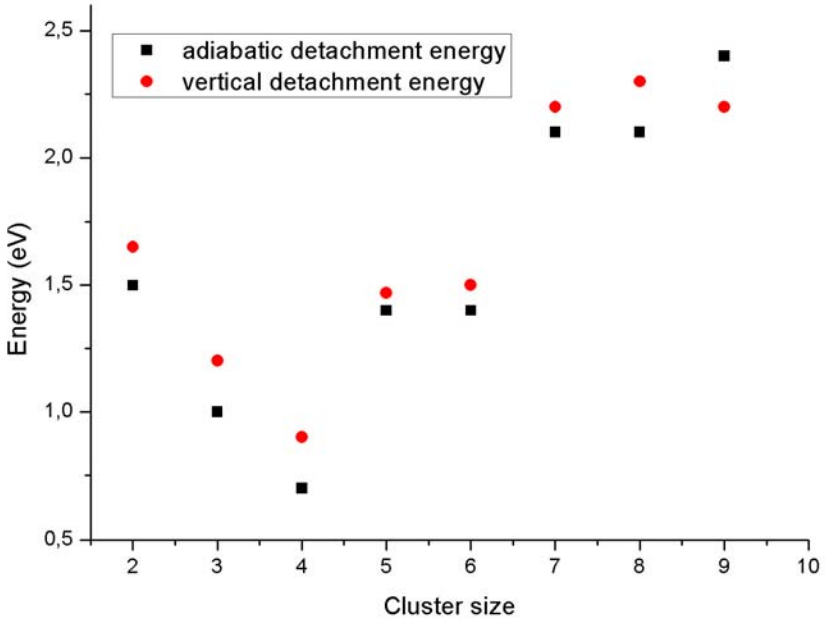


**Figure 2.6:** *Rhodium clusters($Rh_n$, n = 2-9) and their corresponding adiabatic detachment energies and vertical detachment energies.*[30]

## 2.5 Metal–adsorbate interaction

Adsorption processes of small molecules on transition metal (TM) clusters have been investigated over the last decades. Not only in industrial catalysis, but also in the investigation of environmental issues, TM clusters are attractive systems to study, as a large potential lies in their reactions with highly relevant molecules such as CO, $CO_2$, $N_2O$ or methane. In the following sections adsorbate interaction and reactions are presented, which focus on the investigated metal clusters used in this work.

### Niobium

Photoelectron spectra of $Nb_n^-$ with n = 3-20 were investigated by *Kietzmann et al.,*[36] which predicted a reduced reactivity of $Nb_8^-$, $Nb_{10}^-$ and $Nb_{16}^-$ towards **$H_2$**. These three cluster species exhibit a relatively large HOMO-LUMO gap in the corresponding neutral form, which correlates with the reduced reactivity. Both the electronic structure and the geometric properties were found to determine the reactivity of these species.[36]

Studies on primary alcohols (**methanol and ethanol**) activated by niobium oxide anions were performed by *Jackson et al.*[46] Cluster oxides were generated in a laser ablation source and analysed using a Fourier transform ion cyclotron resonance (FT-ICR) mass spectrometer. The dominant reaction mechanism involved initial alcohol condensation at a metal-oxygen double bond to yield $Nb(OH)(OCH_3)$. The resultant niobium-hydroxyl bond subsequently built a new reactive site in the cluster. Due to this reactivity, ligand switching occurred and a niobium-bis-methoxy cluster and $H_2O$ were generated. Dehydrogenation only occurred when two oxygens were doubly bonded to one niobium atom. The Nb-O bond was the dominant structural feature in the investigated cluster systems, due to its high strength (dissociation energy 7.13 eV[47]). Monomeric and dimeric niobium clusters were the most reactive species towards methanol and ethanol, which could be seen as a small size selective effect. Species like $Nb_4O_{10}^-$ were found to be totally inert towards both alcohols. This high stability could have been caused by a closed-shell structure with no Nb-O double bond and a large HOMO-LUMO gap.

*Berg et al.*[48] investigated the adsorption of **benzene** ($C_6H_6$) on charged niobium clusters ($Nb_n^{+/-}$, n = 3-28). Complete dehydrogenation was found to be the dominant reaction

pathway, which led to the formation of $Nb_nC_6$. For anions and cations in the size range of about 12≤n≤22, intact benzene was found to adsorb to the metal cluster via π-bonding. C-H bond cleavage could have been caused by liberation of energy due to the Nb-C bond forming process. This energy resulted in heating of the cluster, which led to the release of hydrogen. Adsorption experiments with **unsaturated hydrocarbons** such as ethylene, propylene and 1-butene resulted in partially and fully dehydrogenated products with neutral niobium clusters.[49] The rate of dehydrogenation increased with increasing cluster size. Full dehydrogenation started to occur for $Nb_n$ with 2≤n≤5. This result was in agreement with thermodynamic considerations that a larger cluster can form more metal carbon bonds. Therefore, the release of more energy caused an increase of evaporated hydrogen. Dehydrogenation was suggested to occur via interaction of an unsaturated C-C bond with the metal cluster. Electron transfer from the π-HOMO of the unsaturated hydrocarbon to the LUMO of the cluster caused the formation of a π-bonded complex which led to dehydrogenation reactions. As neutral and ionic niobium clusters showed strong similarities in the extent of dehydrogenation, this suggested that the charge of the cluster did not change the overall thermodynamics.

## Tantalum

Tantalum clusters were seen to be reactive towards unsaturated hydrocarbons similar to the niobium clusters described previously. The most important reaction of cationic tantalum atoms with alkanes and alkenes is C-H bond activation, which was observed in the late 1980s by *Freiser et al.*[50] Cationic tantalum was found to be one of the few gas-phase cations that is able to activate the C-H bond of methane.[51]

Not only bare cationic tantalum clusters showed interesting reaction pathways however, the corresponding oxide clusters were found to be very reactive to unsaturated hydrocarbons. *Zemski et al.*[51] used a laser vaporisation source and a triple quadrupole mass spectrometer to study the reactivities of cationic tantalum oxide species with 1-butene, 1,3-butadiene and benzene. The major reaction product that was found, was the breaking of the C2-C3 bond of 1-butene and 1,3-butadiene to yield $Ta_nO_mC_2H_4^+$. However, no selectivity for any C-C bond was found. All C-C bonds could have potentially been activated by tantalum oxide cluster

cations. The highest reactivity towards breaking of C-C bonds in both unsaturated hydrocarbons was shown by $Ta_2O_4^+$. During reactions with benzene most oxide clusters exhibited C-C bond breakage to produce $Ta_nO_mC_4H_4^+$ and dehydrogenation to form $Ta_nO_mC_6H_4^+$. The most reactive oxide cluster towards C-C bond breaking of benzene was $Ta_3O_8^+$ and towards dehydrogenation $TaO_2^+$.

## Rhodium

Many experiments of CO oxidation on transition metals (TM) supported on surfaces or in the gas phase were performed.[52,53] *Fu-Yang et al.* studied the adsorption properties of **CO** adsorbed on $Rh_n$ with n = 2-19 using DFT calculations.[53] Depending on the cluster size, adsorption to the top site, bridge site (carbon atom over a Rh-Rh bond) or face site (carbon atom on a triangular plane defined by three rhodium atoms) was favoured. For larger clusters ($Rh_n$ with n = 13-19) adsorption on the bridge and face sites dominated. In addition, it was found that the adsorption energy of CO lay 0.2 eV-0.3 eV above the theoretical value for CO-adsorption on a clean Rh(111) surface at 2.0 eV.[53] Studies on reactions with $N_2O$[54,55] were performed as rhodium is an interesting catalyst for the decomposition of exhaust gases. *Mackenzie et al.*[55] observed that the principle reaction is the sequential addition of oxygen atoms to the bare clusters. A key step in the dissociation pathway could involve the bending of $N_2O$ to bind with N and O to the cluster. Large variations in the rates of reactivity (up to three orders of magnitude) with cluster size for the cationic clusters were observed. The anionic clusters exhibited smaller fluctuations. This trend in reactivity is more similar to those of reactions with small hydrocarbons[56] than with diatomic molecules. Another important reaction of rhodium clusters towards adsorbed molecules is C-H bond activation, which leads to dehydrogenation. Dehydrogenation is one of the major reactions between the investigated metal clusters and adsorbed species observed in this work. *Uggerud et al.*[57] studied the rate coefficients for the **dehydrogenation** of ethane, propane and isobutane with cationic rhodium clusters ($Rh_n^+$, n = 1-30) with Fourier transform ion cyclotron resonance (FT-ICR) mass spectrometry. Two reaction pathways were proposed after one rhodium atom was inserted into a C-H bond. The first mechanism included a 1,1-elimination and the second predicted a 1,2-elimination of $H_2$. In the 1,2-elimination one rhodium atom

π-bonded to ethene was observed. This was primarily observed to occur for smaller clusters. For the 1,1-elimination two rhodium atoms were found di-π-bonded to one carbon. This process was dominant for larger cluster sizes. 1,2-elimination was the dominant mechanism during dehydrogenation of ethane and propane. Due to fast scrambling of the hydrogen, dehydrogenation was reversible in this case. Multiple coordination of ethane was observed for $Rh_7C_6H_{10}^+$. The change of reactivity of larger rhodium clusters was predicted to originate from geometric effects.[57]

Not only dehydrogenation of alkanes was observed, also aromatic compounds such as **benzene** were found to undergo dehydrogenation reactions. Reactions of cationic and anionic niobium/rhodium clusters (n = 3-28) with benzene were investigated by FT-ICR experiments by *Berg et al.*[48] For rhodium clusters up to n = 5, $H_2$-loss was the dominant reaction. By further increasing the cluster size a loss of two $H_2$ was additionally observed. For cationic rhodium clusters with n = 9 total dehydrogenation was observed, similar to what was seen for anionic clusters with n = 12. Molecular adsorption of benzene started to become the most dominant process from $Rh_{14}^-$ on and was assigned to a π-bonded complex. The total adsorption of benzene on larger clusters was driven by the cluster temperature. Larger clusters own more internal degrees of freedom, which allow an easier redistribution of energy caused by complex formation. Therefore, larger clusters are colder and offer a better stabilisation of the adsorbed compound. In addition to temperature properties, geometric configurations could also exhibit a strong influence on the size effect.[48]

Previous studies and DFT calculations on more complex molecules such as (R)-+-limonene (see Chapter 5.1) with a chiral structure adsorbed on TM clusters were not found. Therefore, the analysis and interpretation of the results presented in Chapter 5 could only occur based on the data which was obtained from less complex systems.

# 3. Experimental setup

The experimental setup shown in Figure 3.1 that was constructed during this work enables the investigation of metal cluster-complexes in the gas phase using time-of-flight mass spectrometry and a number of laser spectroscopic techniques. To address the aims of the project, it was necessary to establish three main elements: ***a) cluster source that produced sufficient quantities of the desired clusters, b) an adsorbate delivery method*** for organic compounds to create cluster-adsorbate complexes and ***c) the implementation of laser spectroscopic techniques*** to probe the cluster-adsorbate complexes.

The experimental setup was mounted on an 80x80 mm thick aluminium profile (*RK Rose+Krieger GmbH*) and consisted of three stainless steel chambers and a metal tube whose volume could be evacuated to allow experiments under UHV (Ultra High Vacuum) conditions.

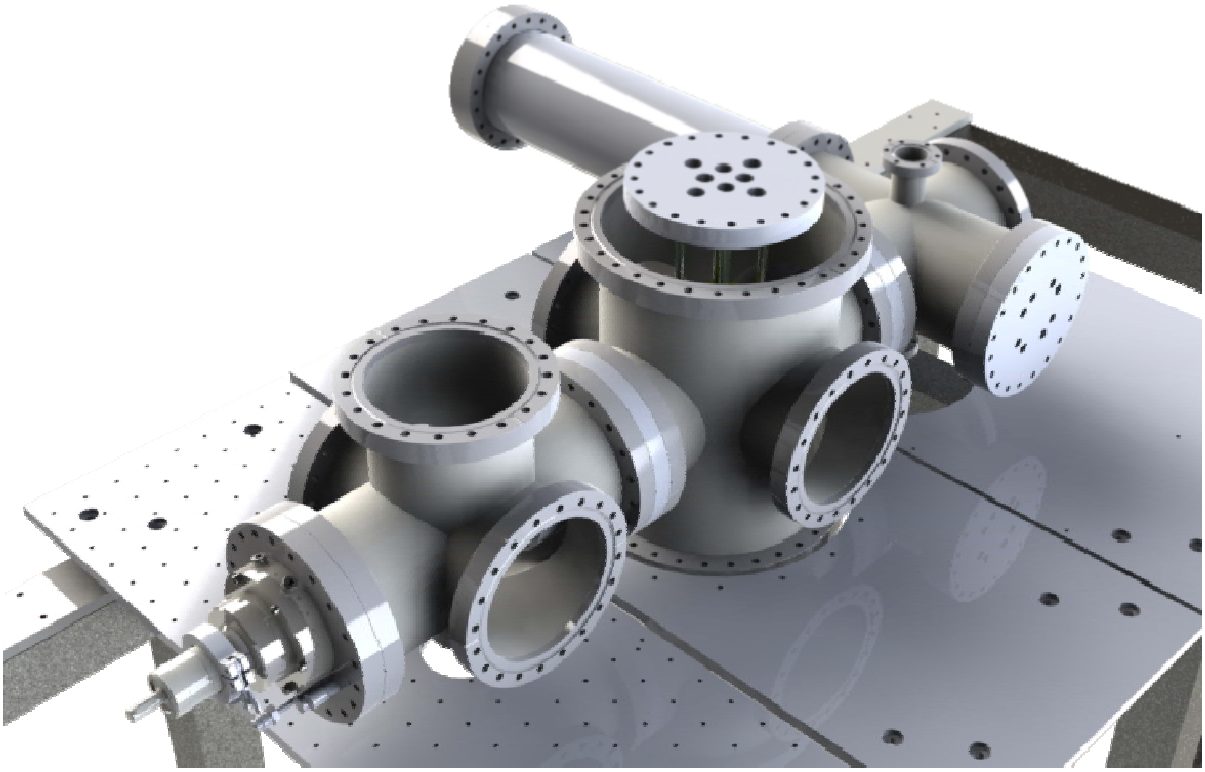

**Figure 3.1**: *3D-CAD model of the UHV setup supported by moveable aluminium plates.*

For a flexible arrangement of the chambers the setup was mounted on 15 mm thick individually moveable aluminium plates which were connected to subjacent solid rails (*Bosch-Rexroth AG*) by so called runners *(Bosch-Rexroth AG*, Figure 3.2). Stoppers were locked onto the solid rails to prevent movement of the individual components during the assembly and disassembly of the chambers.

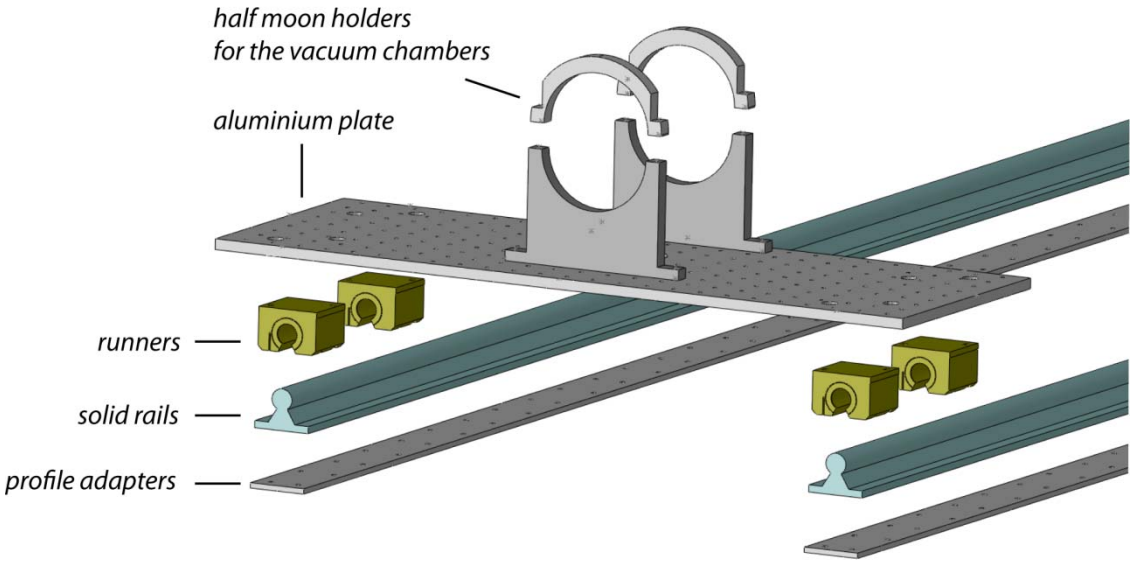


**Figure 3.2:** *3D-CAD model of the individual parts used to support the UHV chambers.*

## 3.1 Laser vaporisation cluster source

The cluster source is the core element of the presented experimental setup. The main principle of cluster formation can be described as a supersaturation of a rapidly cooled vapour flow which causes a homogenous nucleation in the beam[58].

The research of small metal clusters produced using cluster sources has a long history. In the 1960s, scientists were highly interested in studying the properties and reactivities of metal nanoparticles formed using the newly built cluster sources[58]. The stated aim of these studies was to understand the structure and behaviour of the small clusters which lead to metallic properties. *Henkes et al.*[59] and *Leckenby et al.*[60] published the first results on a new technique which employed the non-equilibrium conditions of an adiabatically expanded metal vapour. This breakthrough for laboratory cluster research allowed a more exacting

control of the cluster production process. This meant that scientists could obtain a larger cluster size distribution or a very precise synthesis of structures. Other methods, such as the chemical preparation of nanoparticles did not provide these advantages[61].

Following on from this pioneering work, various types of cluster sources were engineered for different purposes. The source built and used in the present experiment is known as a **laser vaporisation cluster source** and was first published by *Smalley et al.*[62] in the early 1980s. Two main features characterise this type of source: ***a) a laser is used to vaporise*** even the most refractory metals such as Mo or W without a strong heating of the cluster source itself and ***b) a supersonic expansion*** of the gas/cluster mixture. Due to collisions of the vaporised metal nanoparticles with a pulsed inert buffer gas a cooling of the particles occurs.

Through the combination of these two techniques a size regime from single atoms up to several hundreds of atoms can be produced for any desired metal[63]. The cluster source utilised in this work is based upon the design used by *Heiz et al.*[63] To fulfil the aims of the experiment several changes to the original design were made and these will be described in the following paragraphs.

The entire source assembly (Figure 3.3) was fixed onto a CF 160 flange which was bolted onto the source vacuum chamber. A circular **metal target** of 45 mm diameter was fixed onto an inner gear of 50 mm diameter and is the primary element of the cluster source.

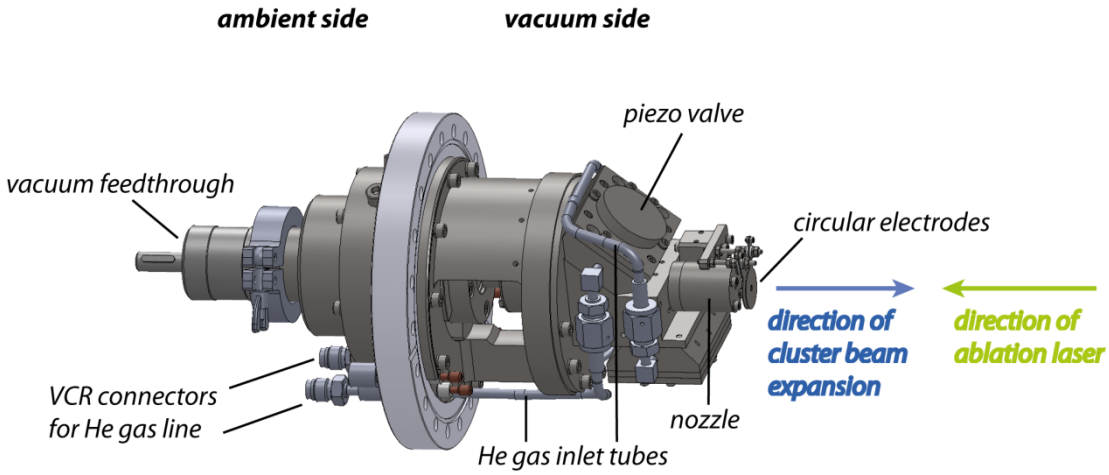


**Figure 3.3:** *3D-CAD model of the laser vaporisation cluster source mounted onto a CF160 flange.*

A motor (*Color-Technik GmbH E 192H*) connected to a vacuum feedthrough *(Pfeiffer Vakuum GmbH DD 040* A, see Figure 3.4) was located on the ambient side of the CF 160 flange and caused a rotation (rotation frequency 0.1-0.2 Hz) of the target assembly inside an outer gear.

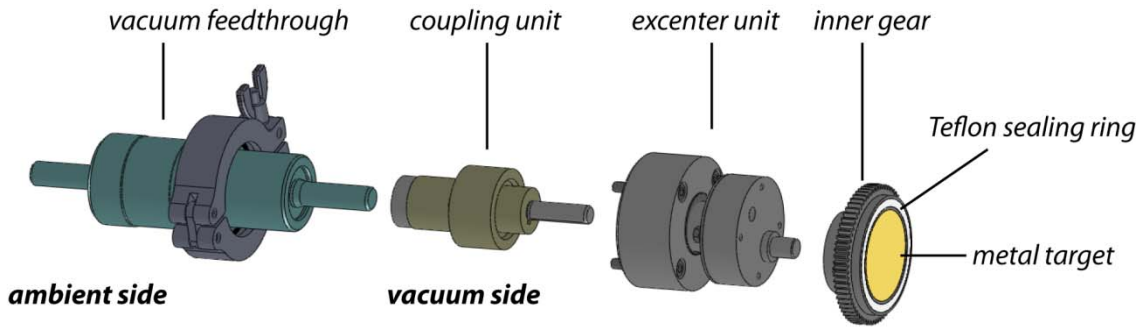


**Figure 3.4:** *Motor-driven assembly with the metal target mounted onto the inner gear. The motor unit on the ambient side is excluded from the diagram.*

The outer gear was screwed onto a polished stainless steel plate against which the target was pushed by a spring mechanism. A flat Teflon ring was used to achieve an air tight seal between the target and the polished plate.

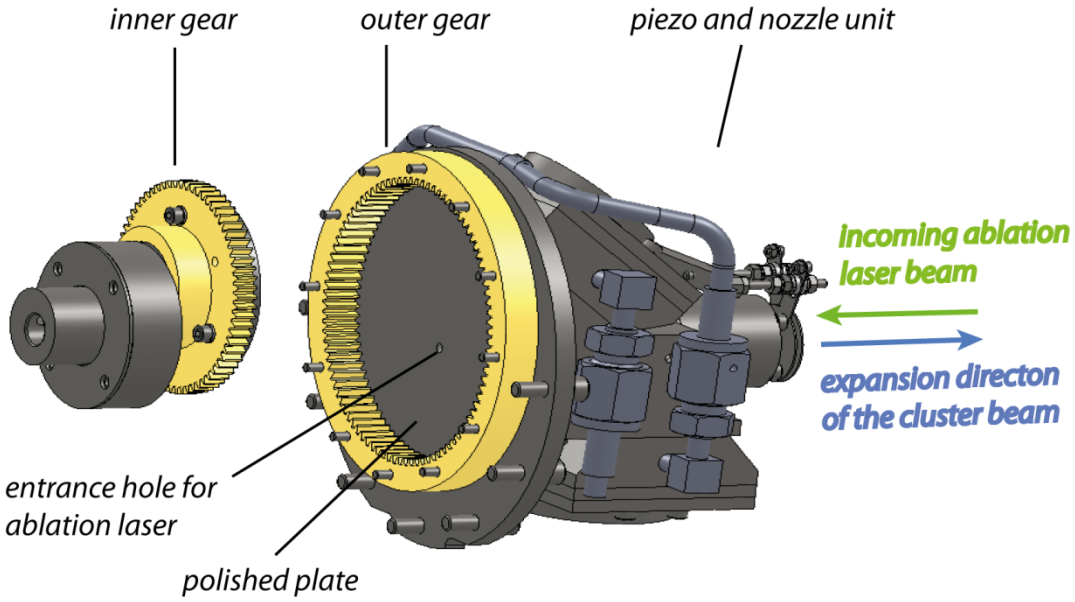


**Figure 3.5:** *Gear assembly with the inner gear rotating inside the outer gear on a polished plate. The off-axis entrance hole for the ablation laser enhances the usage of the target area.*

The ablation laser entry hole was centred on the polished plate, but was off axis in comparison to the centre of target and therefore ablates a hypocycloidal pattern on the target's surface. This principle enabled the usage of 90% of the entire target area[63]. As the creation of a highly stable cluster beam was crucial for the conducted experiments, the gas tight seal around the target and a constant ablation of the target were of high importance.

**Ablation of material** from the metal target surface was achieved by using the second harmonic (532 nm) of a 100 Hz triggered Nd:YAG laser (*Innolas Spit Light* DPSS, ~70 mJ/pulse at 532 nm). The entrance point of the beam into the UHV setup was a CF 40 view port connected to the TOF-MS chamber. To guide the laser beam into the setup an assembly of two highly reflecting mirrors (CVI *Melles Griot, 532 nm*) were used. The two mirrors guided the beam through the entrance hole in the polished metal plate and onto the target. As the laser energy for ablation needed to be over a certain threshold the beam was focused onto the metal target by using a focusing lens (*CVI Melles Griot, focal length 1.3 m*), which was fixed onto an aluminium plate in front of the view port. A schematic overview of the beam path is shown in Figure 3.6.

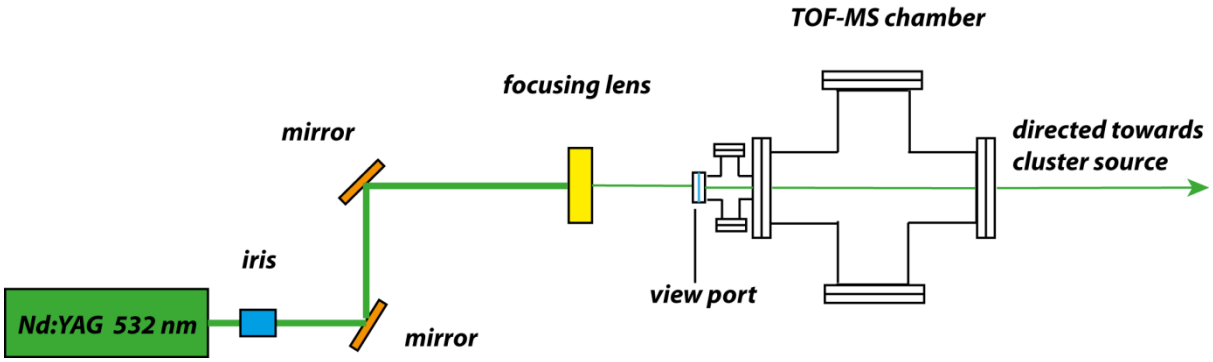


**Figure 3.6:** *The second harmonic (532 nm) of a diode pumped Nd:YAG laser is guided by two mirrors into the setup.*

Two other important elements for cluster formation were the **He carrier gas inlet system** and the **gas expansion** into the vacuum. To introduce helium gas (*Helium 6.0, Westfalen AG*) into the source a gas line was established. This gas line was connected to a piezoelectric valve,[64] which controls the pulsing of the gas (1-10 bar) into a channel pointing in direction of the entrance hole for the ablation laser (Figure 3.7). The piezo valve was controlled by an in-house pulsing device (*TUMelo Piezo Pulser*) which offers variable repetition frequency and pulses of a potential difference of up to 450 V lasting several hundred microseconds.

*Nakajima et al.*[65] were the first to use a **piezo – driven pulsed valve** for the purpose of helium gas injection in laser vaporisation sources. The basic design of a piezo valve is based on the design invented in the late 1980s by *Proch* and *Trickl et al.*[64]. The main advantages compared to common pulsed valves used for molecular beams are short pulses, high repetition rates (up to several kHz), lower power consumption and the ability to cool and heat the nozzle. With these enhancements a longer lifetime of the valve is obtained, as well as the capability for a wide range of applications. Therefore, the valve is a powerful tool for pulsed molecular beams such as those produced in the generation of metal clusters.

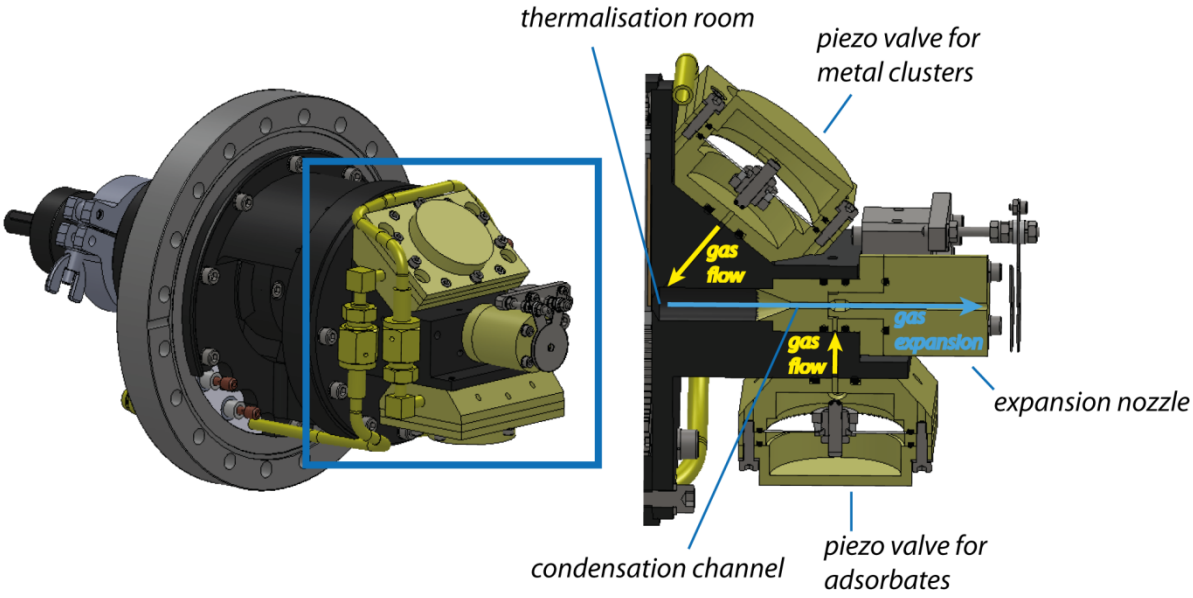


**Figure 3.7:** *3D-CAD cut through of the piezoelectric valves and the expansion nozzle. The directions of gas flow and expansion are highlighted.*

When the target was ablated by the laser, a carrier gas pulse was triggered and the resultant metal vapour plasma was expanded away from the target surface coaxial to the incoming laser beam into the vacuum. Before the gas mixture was ejected into the vacuum the metal vapour passed a thermalisation room and was cooled through collisions with inert gas atoms. The cluster beam was formed as the gas/cluster mixture expanded out of the nozzle into the vacuum.

As mentioned previously, the establishment of an adequate adsorbate delivery method to create metal-organic complexes was one of the most important aims of the presented work.

In the past decades several groups worked with organic and inorganic compounds adsorbed onto transition metal clusters. In the mid 1980s *Castleman et al.*[66,67] performed adsorption experiments with different metal clusters such as Titanium,[68] Aluminium,[69] Niobium[70] and Tantalum[71] towards organic and inorganic species. For this purpose a laser vaporisation source with a rotating and translating metal rod was used to produce the metal clusters. The ablation of metal particles was performed by using the second harmonic (532 nm) of a Nd:YAG laser. Castleman used an adsorbate delivery system which was implemented inside the source. A small percentage of the adsorbate molecules were entrained in a carrier gas pulse valve at a back pressure of 5 bar. That means that the pulse properties of the reactant species depended on the carrier gas settings.

*Cox et al.* and *Kaldor et al.* also contributed to the field of interactions between metal clusters and simple organic and inorganic species (e.g. palladium clusters and CO[72], aluminium clusters and methanol[73] or niobium clusters and benzene[74]). Metal clusters were generated in a laser vaporisation source in the same process that was used in the work of Castleman. The helium gas inlet used for the carrier gas was a double solenoid actuated pulse valve, designed by *Smalley et al.*[75], which operated with a pulse width of 200-300 µs. The source contained a 7.6 cm long reactor tube into which a reactant gas, seeded in helium, was injected by a second gas pulse. Therefore, the gas inlet system consisted of two pulsed valves, one for the cluster cooling and one for the reactant gas which enabled separate control of each gas pulse. This procedure was a more efficient way of forming cluster–adsorbate species because the actual metal cluster formation is less affected by perturbances.

To realise the introduction of organic species into the present cluster source a unique modification was made to the design of the source. A **second piezoelectric valve** was added to the source setup to introduce organic compounds to the cluster beam inside the expansion channel (see Figure 3.7). The mode of operation was analogous to that of the piezo valve for the helium buffer gas. Otherwise, the gas line of the second piezo was additionally connected to a bubbler (Figure 3. 8), filled with the target adsorbate in liquid form, through which a helium gas stream (1-5 bar) was channelled. Subsequently, the resulting mixture was fed to the second piezo valve and dosed into the condensation channel of the cluster source after the metal clusters were formed. This setup enabled the

precise control of cluster–adsorbate species due to the independently operating valves. The output of each valve could have been adjusted by changing the helium back pressure, pulse width and the potential applied to the piezo disc. Optimisation of the cluster distribution was achieved by changing the settings of both valves.

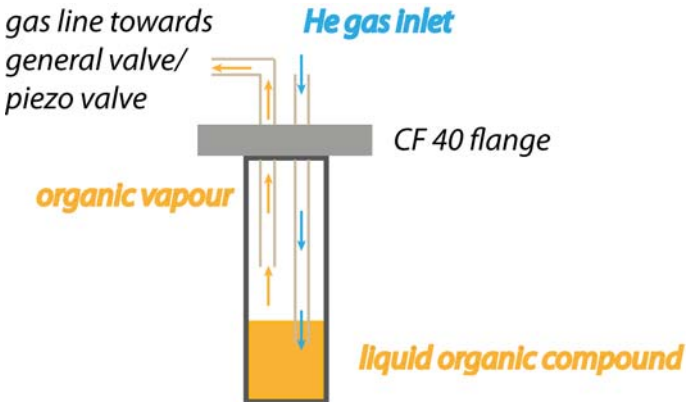


**Figure 3. 8:** *Overview of the adsorbate inlet system consisting of a helium gas line connected to the input of the bubbler housing containing the organic compound. The gas/adsorbate mixture is channelled by a second gas line into the second piezo valve or the general valve.*

Several experiments were performed with the operation of the second piezo valve (see Chapter 5). The results showed the first successes in the formation of cluster-complexes. However, due to experimental difficulties in creating sufficient amounts of the cluster-adsorbate species a second type of valve was utilised. It will be described in the following sub-chapter.

## 3.2 General valve

A general valve is a pulsed magnetic valve with a high repetition rate (*Parker Hannifin Corp., General Valve*, Series 9). A general valve was installed in the source chamber perpendicular to the expansion direction of the cluster beam (Figure 3.9). The faceplates of the valve can be changed in order to vary the diameter of the nozzle orifice. The nozzle orifice diameter used for this work measured 200 µm. A turbomolecular pump (*Pfeiffer Balzers TPU 2200*) which was backed by a rotary vane pump (*Pfeiffer Duo 060 A*) was connected to the central chamber and evacuated the three main chambers as well as the drift tube. To prevent

contamination of the turbo pump with oil from the rotary vane pump a zeolite trap was installed onto the rotary vane pump. The pumps were connected to each other by a flexible metal bellows. In the case of a loss of power both pumps were switched off simultaneously due to an interlock implemented in the pumping control unit (*Pfeiffer TCP 5000*).

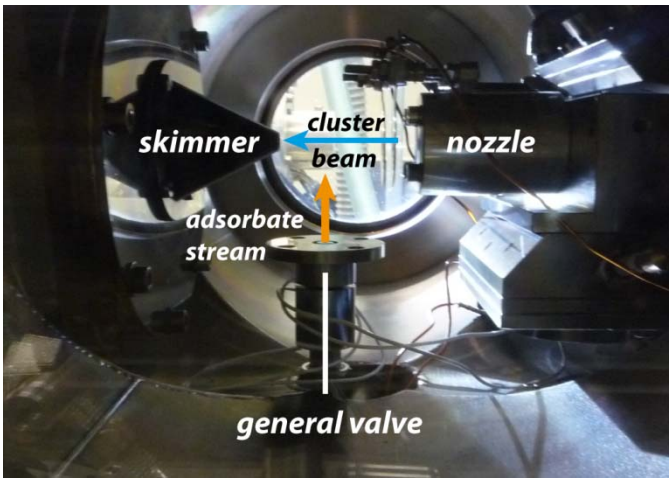


**Figure 3.9:** *Inside view of the source chamber with expansion nozzle, skimmer and general valve. The valve was inserted outside of the cluster source, perpendicular to the cluster beam expansion*.

One main difference compared to the second piezo valve was the point of installation. The general valve was located outside of the source and therefore, the adsorbates were dosed onto the cluster beam after the clusters expand into the vacuum. Another important difference was how potentials were applied to each valve. The potential for the piezo valve was directly applied across the piezo ceramic disc using a small wire. When reactant species were introduced into the piezo housing and the pressure within the valve housing was within a certain range, then arcing could have occurred, which would have damaged the piezo valve and potentially fragment the reactant molecules. Contact between the applied voltage and the reactant species inside the general valve was eliminated as the driving solenoid is separated from the internal gas reservoir. The results obtained from the use of each of the valves are presented and discussed in Chapter 5.

## 3.3 Ion Optics

Ion optics are powerful tools used to guide charged species through the setup. The trajectory of the particle beam can for example be converged and magnified in a way that is analogous to that of light through an optical lens. Deflection or bending of the ion beam is also feasible[76]. Several different kinds of ion optics were implemented in the presented experiment. The following sketch shows an overview of the individual ion optics installed in the experimental setup.

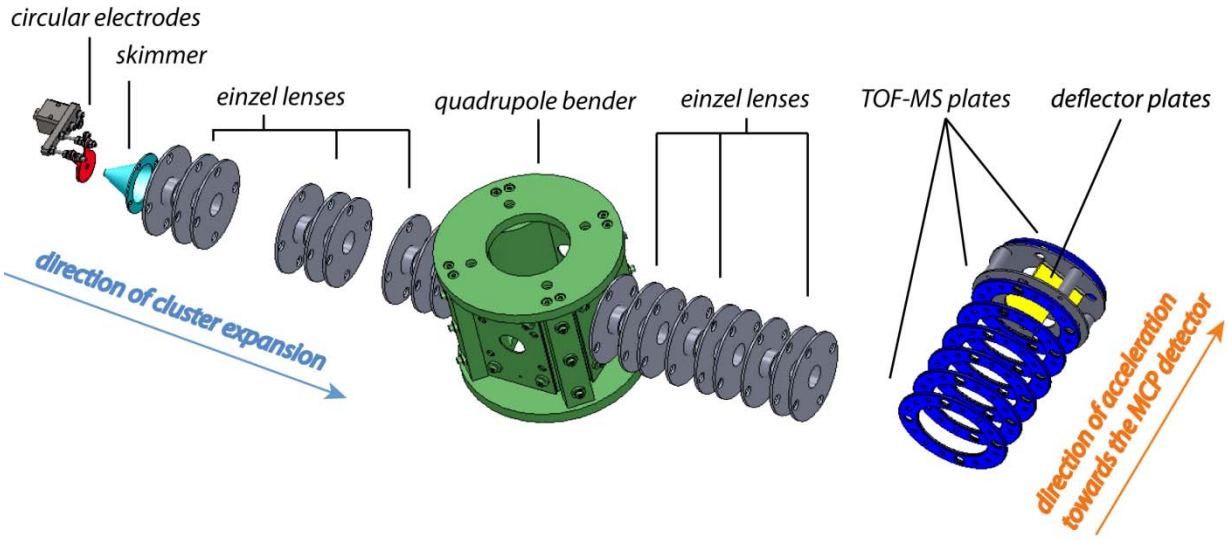


**Figure 3.10:** *Overview of the ion optics used to guide the cluster beam from the cluster source chamber into the TOF-MS and further to the MCP-detector.*

**Two circular electrodes** (Figure 3.11) formed the first ion optic lens which the charged species pass and were attached to the cluster source housing in front of the nozzle. If neutral species were investigated, a voltage (*TUM Bipolar HV Power Supply*) was applied to the first electrode to cause a deflection and therefore a filtering of all charged species. The second electrode was kept at ground potential to avoid unwanted electric fields in the source chamber.

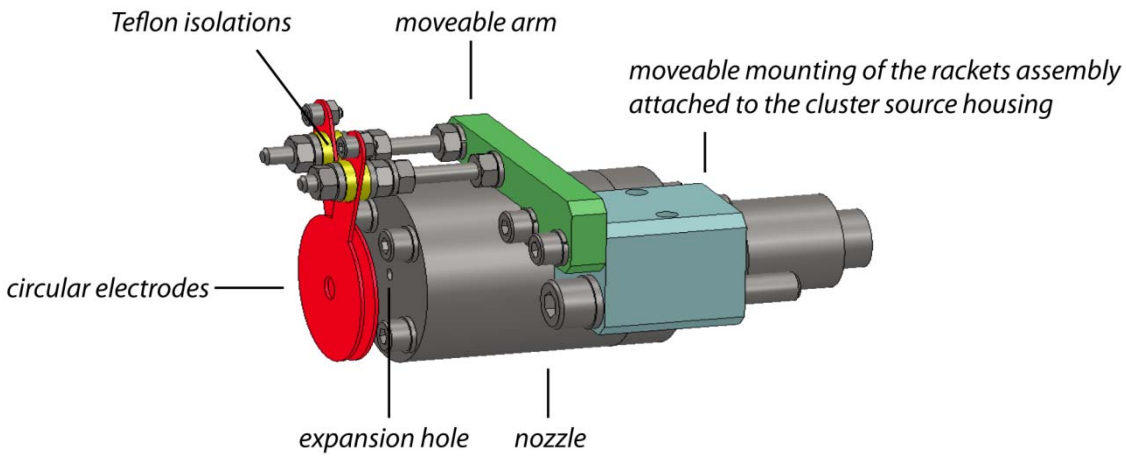


**Figure 3.11:** *Sketch of the expansion nozzle with two attached circular electrodes used as ion filter.*

Subsequently a ***skimmer*** with a 5 mm opening was used to collimate the expanded gas/cluster mixture into a beam and to achieve a differentially pumped setup. The distance between nozzle and skimmer influenced the pressures in the following chambers due to the geometry of the helium gas expansion. The skimmer was mounted onto a housing consisting of a metal plate and two adapter tubes, enabling the adjustment of the distance between nozzle and skimmer. The housing itself was supported on a sandwich flange by a mounting plate (Figure 3.12). This sandwich flange formed the link between source chamber and the adjacent chamber and additionally functioned as a support for the subsequent ion optics (**electrostatic lenses**), which guided the charged species into the time-of-flight mass spectrometer (TOF-MS).

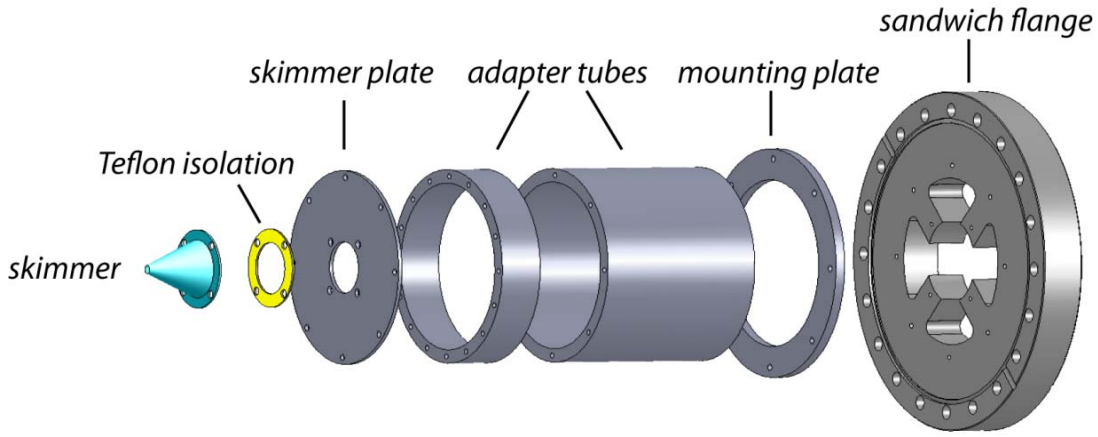


**Figure 3.12:** *Exploded view of the skimmer and support assembly*

The skimmer and the electrostatic lenses were electrically isolated from the chambers by using Teflon and ceramic isolations and were set to specific potentials by using coaxial BNC electrical feedthroughs (*VACOM Vakuum Komponenten & Messtechnik GmbH*, max. transmission 500 V) which were welded into the sandwich flange. Optimisation of the potentials led to an enhancement of the total amount of charged particles arriving in the TOF-MS. The electrostatic lenses used in this experiment consisted of stainless steel metal plates with a cylindrical tubular extension on one side and were assembled in a group of three (stack of lenses, Figure 3.13). Theses lens stacks functioned as **Einzel lenses** when the two outer lenses were set at ground potential and a non-zero potential is applied to the middle element.

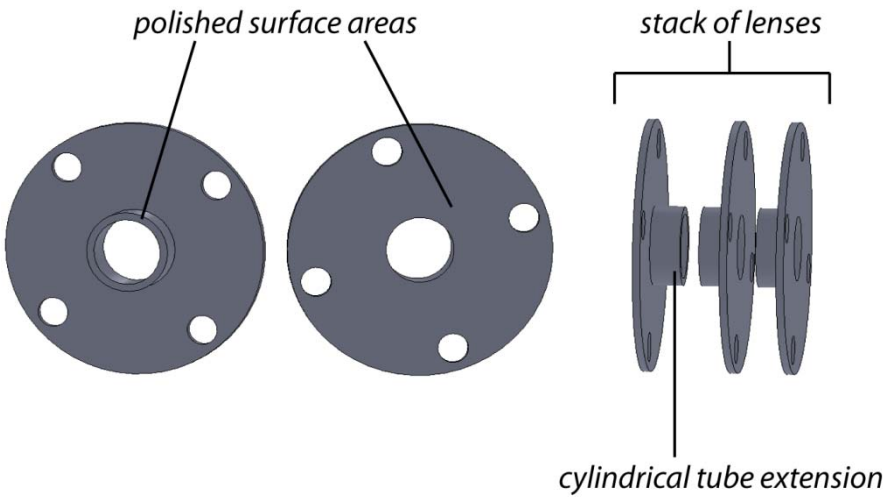


**Figure 3.13:** *Electrostatic lenses in a stack of three with polished surface close to the cylindrical opening to ensure homogeneous field lines.*

During the experimentation it was recognised that applying an adjustable potential (*TUM Bipolar HV Power Supply*) on every lense element individually led to a better control of the cluster beam trajectory.

The electrostatic lenses were mounted on four threaded bars which were fixed into the sandwich flange. Three stacks of lenses were installed behind the skimmer, with one in front of the sandwich flange, one inside the flange and a third one behind the flange.

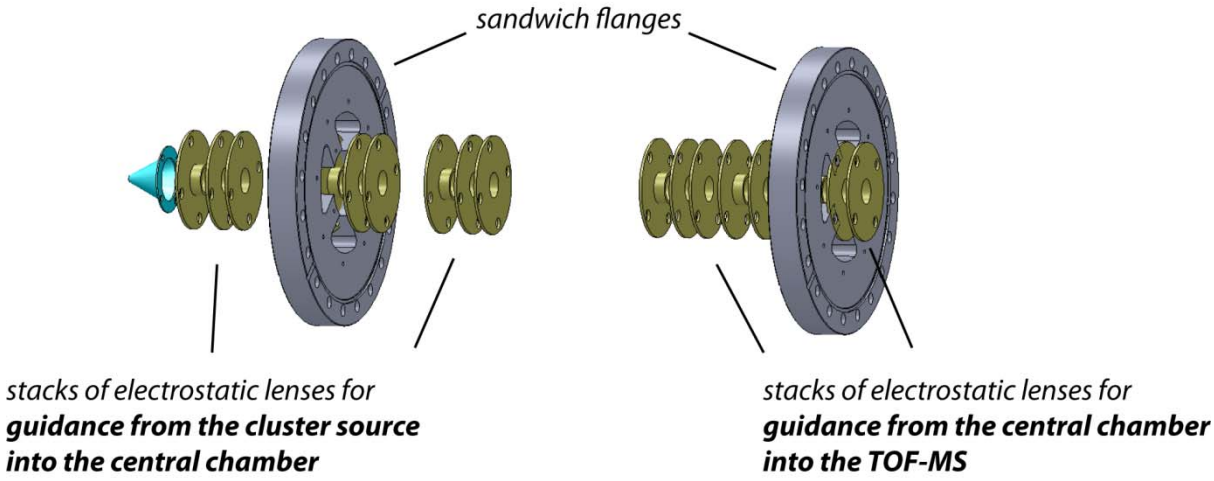


**Figure 3.14:** *Overview of all stacks of lenses implemented in the experiment. The threaded bars and the quadrupole bender are excluded from this sketch.*

For future experiments a quadrupole mass spectrometer (QMS) and a ring electrode ion trap will be installed along a perpendicular axis of the central chamber. A **quadrupole bender** (Figure 3.15) was mounted into the middle of the chamber and will be used to bend the cluster beam into the QMS. The plates of the bender which were fixed in direction of the cluster expansion towards the TOF-MS were additionally used to optimise the beam trajectory.

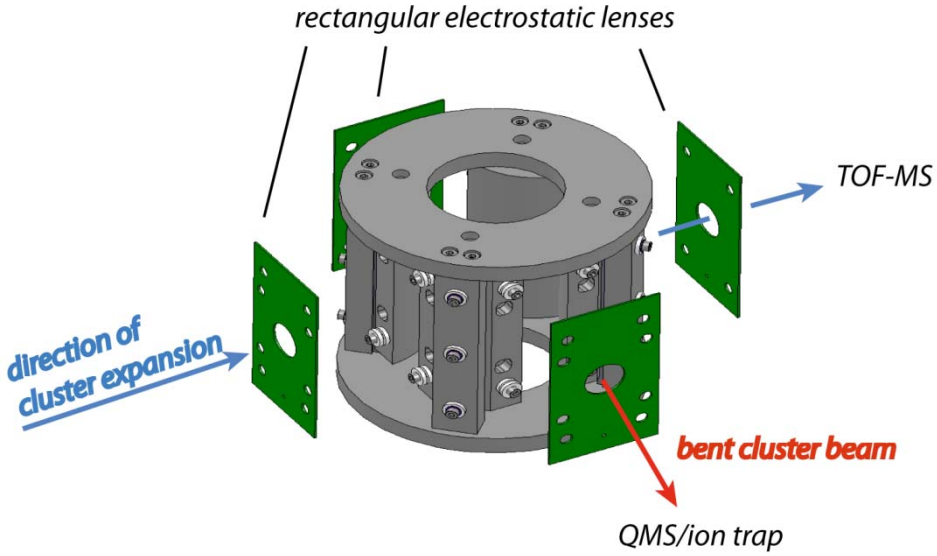


**Figure 3.15:** *3D CAD model of the quadrupole bender with rectangular entrance and exit plates used for ion guidance. The ion beam can be bent perpendicular to the expansion axis into a QMS with an ion trap for reactivity studies.*

Following the bender three more stacks of lenses were mounted onto the sandwich flange between the central and TOF-MS chambers in the same arrangement as the lenses described previously (see Figure 3.14), and were used to ensure an optimum amount of charged species entering the TOF-MS. Ion optics which belong to the TOF-MS assembly are described and shown in further detail in the following sub-chapter.

## 3.4 TOF-MS

Mass spectrometry of the produced cluster species was performed using a home-built linear Wiley McLaren type time-of-light mass spectrometer, mounted onto a CF 160 blind flange with integrated BNC and SHV feedthroughs. The assembly (see Figure 3.16 below) was situated in the third main chamber of the setup.

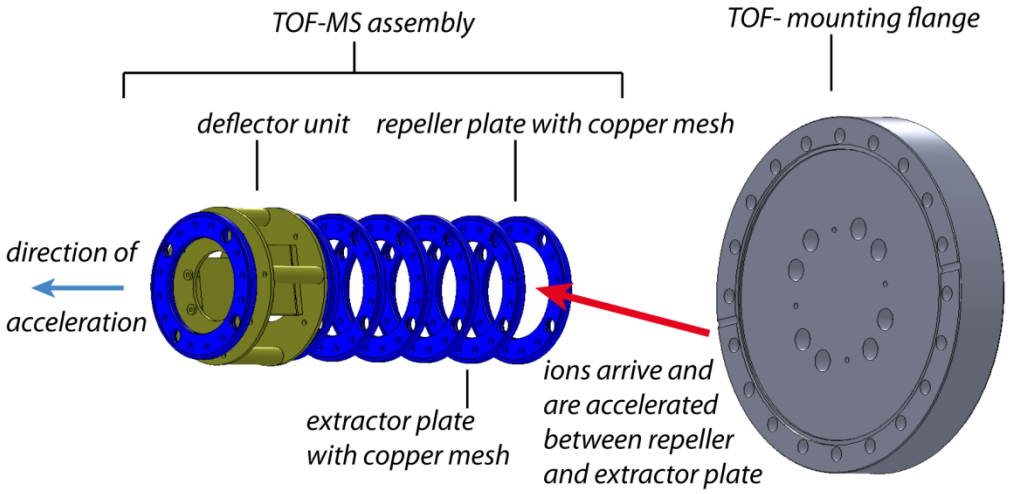


**Figure 3.16:** *Overview of the TOF-MS assembly with implemented deflector unit and TOF-mounting flange. The ions arrive between the repeller and extractor meshes and are extracted in the direction of the detector.*

As the ions arrived in between repeller and extractor plate of the TOF-MS they were accelerated perpendicular to the cluster expansion direction. Mass separation of the charged species occurred as heavier ions experienced longer flight times in the field free drift region (see Chapter 2.2 for the theory of TOF-MS).

The TOF-MS was constructed of several circular plates with circular centred holes (58 mm) to allow ion extraction. Copper meshes (70 LPI Cu mesh bonded to 58mm OD SS rings, *Precision Eforming*) covered the holes of the repeller, extractor and ground plates to ensure a homogeneous electric field throughout the ion path. The cluster beam entered the TOF-MS between the repeller ($U_1$) and the extractor ($U_2$) plate. Both plates were electrically isolated from each other and were set to a high positive or negative voltage by using HV power supplies (*FuG Elektronik GmbH DC Power Supply HCP 14-6500, Fug Elektronik GmbH Hochspannungs-Netzgerät HCN 35-3500*). The potentials for repeller and extractor plates were applied in a pulsed manner through the use of two high power pulsing units (*Behlke Power Electronics GmbH*, *6.5 kV*) connected in between the plates and the HV power supply units. The TOF-MS frequency was adjusted to the 100 Hz operating frequency of the cluster ablation laser. The region between the repeller and extractor plates can be termed as the first acceleration stage with the electric field strength $E_1$. To obtain a second stage of constant acceleration with electric field strength $E_2$, the extractor plate was connected to the four following plates by a series of resistors of the same value. With this arrangement (Figure 3.17) a potential gradient was achieved.

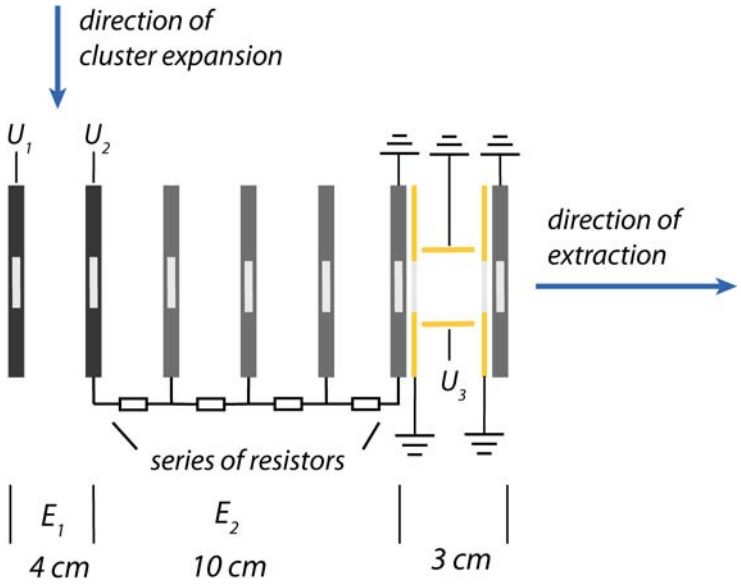


**Figure 3.17:** *Schematic overview of the TOF-MS with a potential $U_1$ applied to the repeller plate, $U_2$ applied to the extractor plate and $U_3$ applied to one of the deflector plates.*

Two rectangular shaped deflector plates were located after the grounded plate of the TOF-MS (Figure 3.18) and were use to maximise the signal intensity of a certain mass range by compensating for the velocity of the clusters in the expansion direction, which is oriented vertically to the TOF-axis, and steering them onto the detector. They were fixed perpendicularly to the acceleration direction using two additional circular plates. One of the deflector plates can be set to a specific potential ($U_3$) of up to 5000 volts (*FuG Elektronik GmbH MCN 14-2000*). The final plate was set to ground to avoid electric fields in the field free drift region.

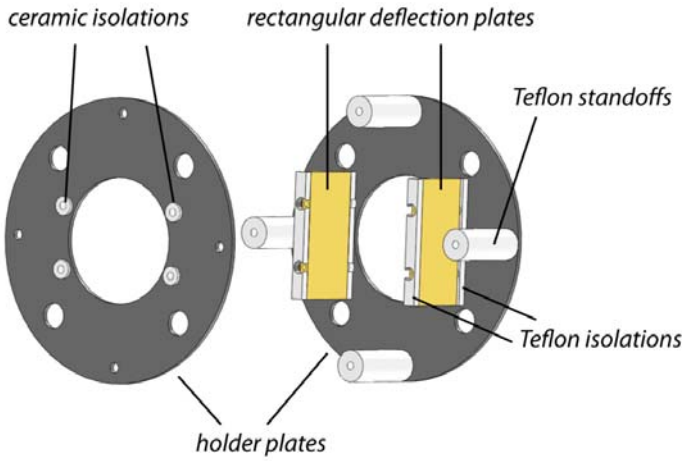


**Figure 3.18:** *3D-CAD model of the deflection assembly implemented at the end part of the TOF-MS.*

After the clusters left the TOF-MS ion source they entered a field free drift region of 30 cm length. For detection of the ions a micro channel plate detector (*SI Scientific Instr. GmbH*, active area of 40 mm) was installed at the end of the drift tube on a CF 160 flange (Figure 3.20). The detector worked as an electron multiplier where incoming ions caused an electron cascade and thus amplified the signal. The detector consisted of two microchannel plates (chevron configuration) and a metal anode and provided a gain of ~ $1 \cdot 10^7$. The front surface of the first MCP was held at ground potential to enable the detection of both positively and negatively charged species. The back surface of the second plate was connected via a resistor with 7 % of the total detector circuit resistance to the anode while the anode was directly connected to a HV power supply (*FuG ElektroniK GmbH DC Power*

*Supply HCP 14-6500*) with a working voltage of 2.4 kV. A schematic overview of the detector assembly is shown in Figure 3.19.

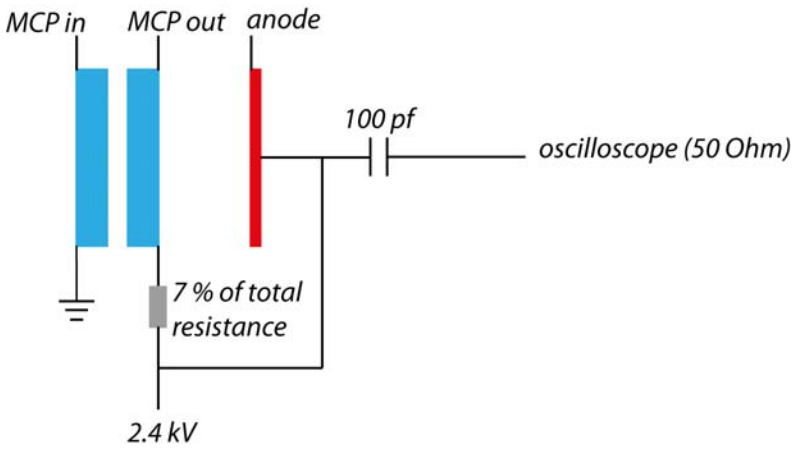


**Figure 3.19:** *Schematic overview of the detector assembly with the applied voltage of 2.4 kV*

Due to the potential difference of 2.4 kV applied over the detector, electrons were accelerated towards the anode. A capacitor (100 picofarad) was used to decouple the AC signal from the applied DC voltage. This allowed the recording of the electron current at the 50 Ω input of the oscilloscope (*LeCroy waveRunner 44Xi-A*), where a voltage change in the mV range was observed for the detection of a single ion.

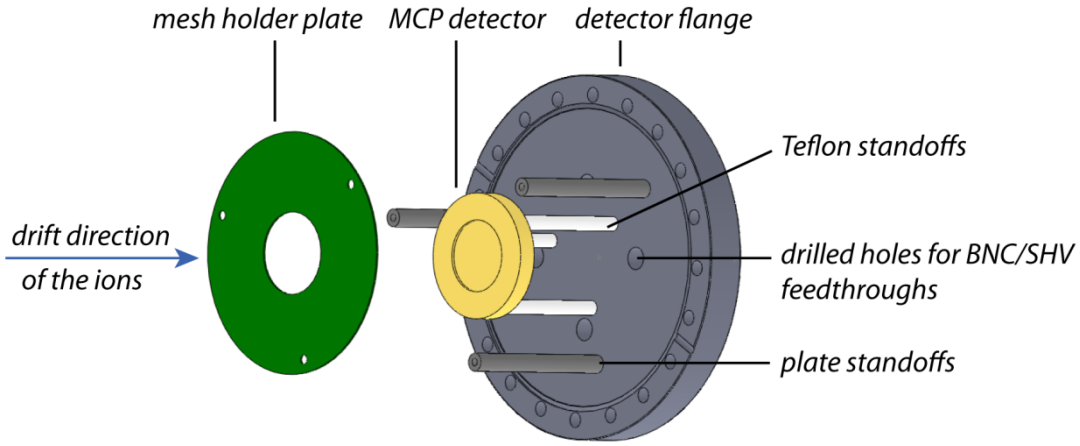


**Figure 3.20:** *Simple 3D-CAD model of the MCP detector mounted onto a CF160 flange. To preserve a homogenous field for the arriving ions a mesh covered plate is installed in front of the detector.*

The flight paths of ions drifting towards the MCPs can potentially be perturbed by the electric field caused by the potentials applied to the detector before they penetrate the first

MCP plate. Therefore, a mesh covered circular metal plate (see Figure 3.20) was installed in front of the detector to ensure that the TOF-MS drift region remains field free.

A four-way cross was connected to the TOF-MS chamber, which contained a manipulator holding a glass slide (*VACOM Vakuum Komponenten & Messtechnik GmbH series EPP*, Figure 3.21). As neutral species were not extracted by the electric field of the TOF-MS they continued to travel in the direction of expansion. At the end of the chamber they would be deposited on the surface of a quartz view port (*Torr Scientific Ltd*) through which the ablation laser beam had to pass. Having the clusters deposited here would eventually have damaged the quartz view port after a certain time. Instead of deposition on the view port the neutral species were impeded by the glass slide.

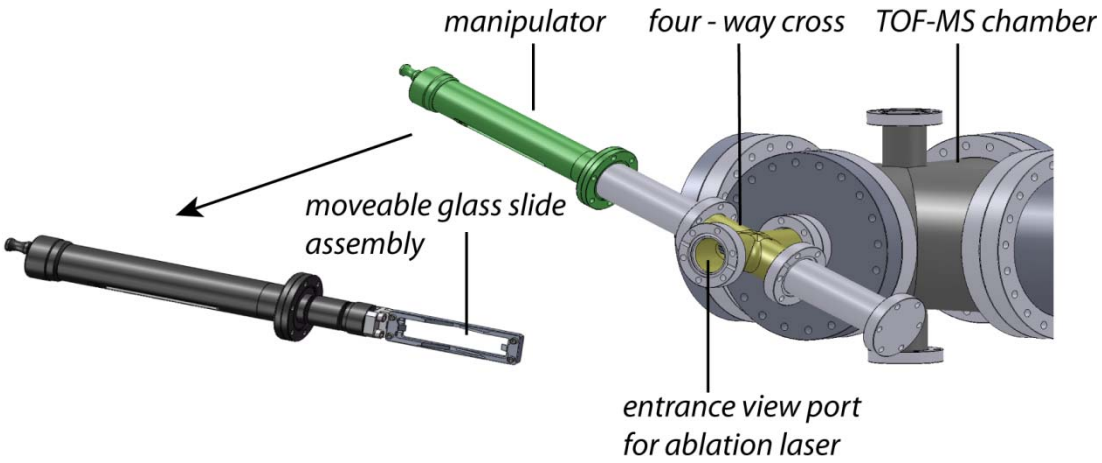


**Figure 3.21:** *Assembly of the moveable glass slide attached to the TOF-MS chamber by a four-way cross. The glass slide prevents deposition of the neutral clusters onto the view port.*

## 3.5 Pumping units

Time-of- flight mass spectrometry of metal cluster species requires a clean and contamination free vacuum. For this purpose a vacuum assembly of 4 different pumps was utilised (Figure 3.22). A turbomolecular pump (*Pfeiffer Balzers TPU 2200*) which was backed by a rotary vane pump (*Pfeiffer Duo 060 A*) was connected to the central chamber and evacuated the three main chambers as well as the drift tube. To prevent contamination of the turbo pump with oil from the rotary vane pump a zeolite trap was installed onto the rotary vane pump. The pumps were connected to each other by a flexible metal bellow. In

the case of a loss of power both pumps were switched off simultaneously due to an interlock implemented in the pumping control unit (*Pfeiffer TCP 5000*).

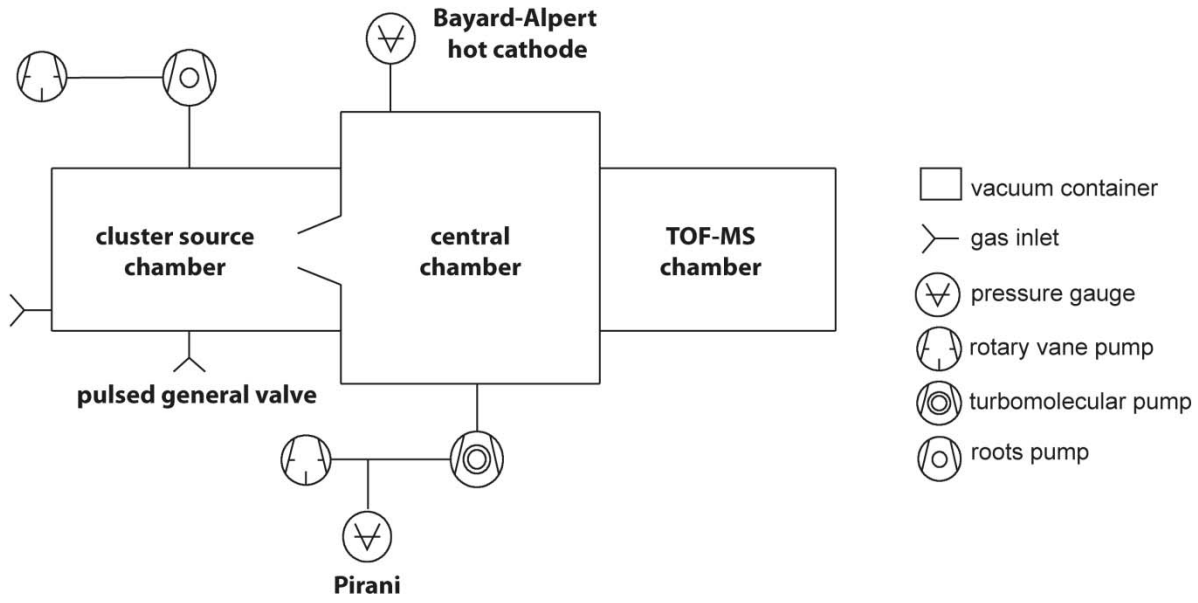


**Figure 3.22:** *Schematic diagram of the pumping units and pressure gauges attached to the UHV setup.*

When the helium gas pulse was operating a large amount of gas was introduced into the cluster source chamber. A roots pump with a high throughput (*Oerlikon Leybold Vacuum Ruvac WS 1001, 1200 $m^3/h$*) was attached to the source chamber to pump away as much excess gas as possible. This pump was also backed by a rotary vane pump (*Busch R5 RA 0205*) to maintain a high pumping speed at low pressure. To monitor the current pressures within the chambers and after the pre pump of the turbo pump, pressure gauges (*Pfeiffer Vacuum Compact FullRange$^{TM}$BA Gauge, Pfeiffer Vacuum Compact Pirani TPR*) were installed. The pressures were displayed on a gauge control unit (*Pfeiffer Vacuum MaxiGauge$^{TM}$*).An overview of the pressure ranges within the setup with and without the operating helium gas pulse in operation is given in table 3.1.

**Table 3. 1***: A list of the reached pressures in the setup with and without using the helium gas pulse.*

| **chambers** | **pressure /mbar without He gas pulse and roots pump off** | **pressure/mbar with He gas pulse (8 bar back pressure)** |
|---|---|---|
| cluster source chamber | $10^{-5}$ - $10^{-6}$ | $10^{-1}$ - $10^{-2}$ |

| | | |
|---|---|---|
| central chamber | $10^{-7}$ - $10^{-8}$ | $10^{-5}$ |
| TOF-MS tube | $10^{-7}$ - $10^{-8}$ | $10^{-5}$ |

## 3.6 Laser setup for spectroscopy

The differentiation of chiral metal cluster species through the use of laser spectroscopy is the ultimate goal of the presented experiment. Various spectroscopic techniques such as REMPI (Resonance Enhanced Multiphoton Ionisation), and photodepletion (by dissociation) spectroscopy are important tools to probe the cluster–adsorbate complexes. A special version of REMPI is circular dichroism laser spectroscopy which allows enantio-sensitive detection of chiral molecular systems. Non resonant photoionisation and –depletion of metal clusters at a wavelength of 355 nm were performed and shown in this work as a first proof for the capability of the experimental setup for future experiments. The third harmonic (355 nm) of a Nd:YAG laser (*Innolas Spit Light* ,120 mJ/pulse) was used for the ionisation and depletion experiments. This laser can be used to pump a dye laser in future experiments in order to perform wavelength depend spectroscopy. The laser beam was guided by several high reflecting mirrors (*Melles Griot BV, 355 nm*) and periscope assemblies (*ThorLabs RS99*).

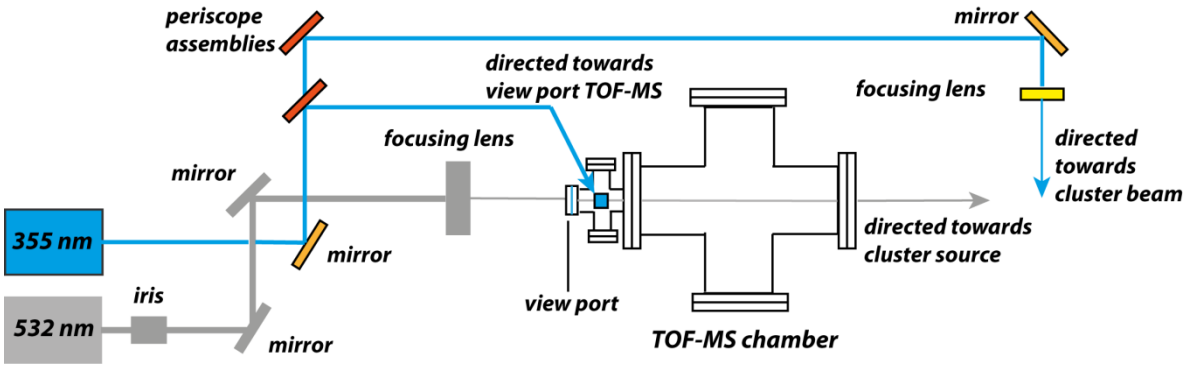


**Figure 3. 23:** *Overview of the guided 355 nm laser beam paths towards the experimental setup.*

There were two potential positions of interaction between laser and cluster beam available. The first position was located in the source chamber. The laser beam passed through a CF 100 quartz view port mounted onto the source chamber and irradiated the cluster beam at

right angles in the region between nozzle and skimmer. The second position of interaction was set between the repeller and extractor plates in the TOF-MS (see Figure 3.24). In order to overlap the beams perpendicularly, the laser beam passed a CF 40 quartz view port mounted on the top side of the TOF-MS chamber.

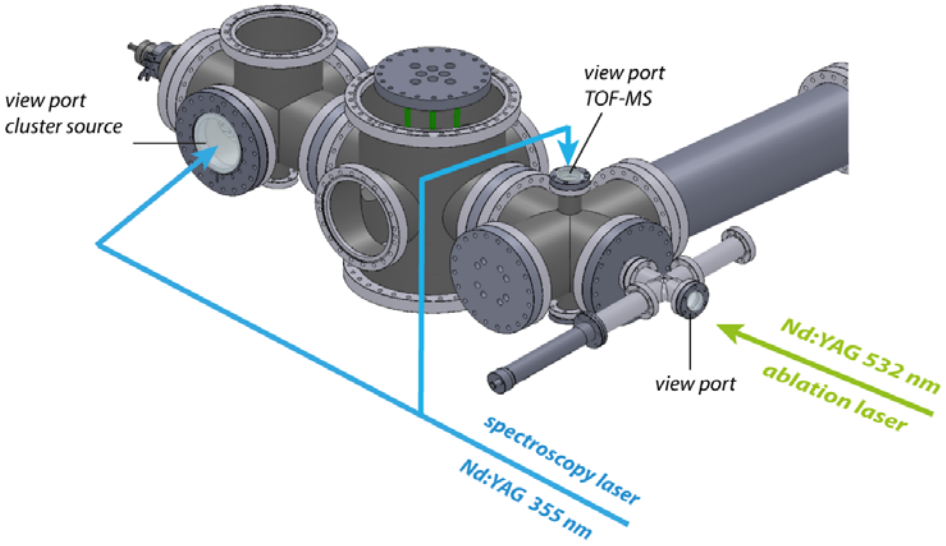


**Figure 3.24:** *Potential beam paths for the 355 nm pump laser. The cluster species can be either probed in the source chamber between nozzle and skimmer or in between the repeller and extractor plate of the TOF-MS.*

The time delay of the laser was synchronized to the delay of the ablation laser using a delay generator described previously. However, in comparison to the 100 Hz of the clustering process the repetition rate of the spectroscopy laser was set to 33 Hz. This caused a measurable event every third ablation laser pulse (see
Figure **3.25**).

## 3.7 Data acquisition procedure and treatment

The most crucial element of the cluster formation was the ablation laser, which operated with a frequency of 100 Hz. All other experimental elements were synchronised with it. Every element ran at a frequency of 100 Hz except for the general valve and the Nd:YAG laser for the spectroscopy experiments (see Chapter 6), which operated at a repetition rate of 33 Hz and a laser pulse length of 10 ns. Three digital delay generators (*Standford*

*Research Systems DG645*) were used to adjust the timing of the different elements with respect to each other. A schematic overview of the prevalently used delay timings for the cluster source settings is shown in

Figure **3.25**. The settings for each of the elements were optimised for the metal target and the pressure conditions to gain a stable and high in intensity cluster signal.

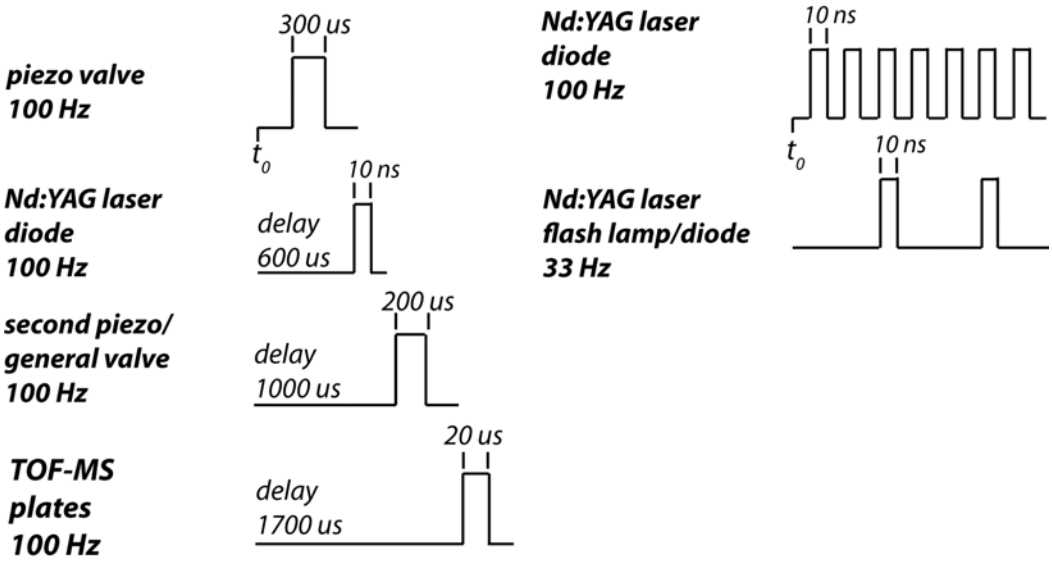


**Figure 3.25:** *Scheme of the pulsed experimental elements and their delay with respects to the ablation laser for a standard experiment.*

As described previously, the ion signal caused by the charged species hitting the MCP detector was recorded using an oscilloscope. Only if the oscilloscope was triggered at the same time as the TOF-MS electrodes (see Chapter 3.3) was the measured t was representative of the ion flight time. The signal was recorded as the intensity (change of the potential at the MCP anode, mV) as a function of time (s) where time 0 was defined by the pulsing of the TOF-MS electrodes. During optimisation of the delay settings of the experimental components an average of approximately 20-50 experimental cycles was used to see an immediate effect on the cluster formation process. For data analysis the number of averages is increased to 1000 to ensure an accurate tracking of the cluster signal evolution. The time-of-flight spectra were recorded in the form of an ASCII file. To transform the flight time t into an ion mass, a mass calibration was required. According to the metal used a comparison between assumed masses (e.g. cluster sizes) and the t of the observed peaks were performed. As described in Chapter 2.3, the square roots of several masses were plotted against the corresponding time-of-flight times and a regression line was

generated. The equation of the resulting function, with slope *a* and ordinate intercept *b* (see Equation 1), was used to convert the time-of-flight scale into a mass scale.

$$m_{TOF} = (a \cdot t_{TOF} - b)^2 \qquad (37)$$

An example of mass calibration for cationic tantalum clusters is shown below.

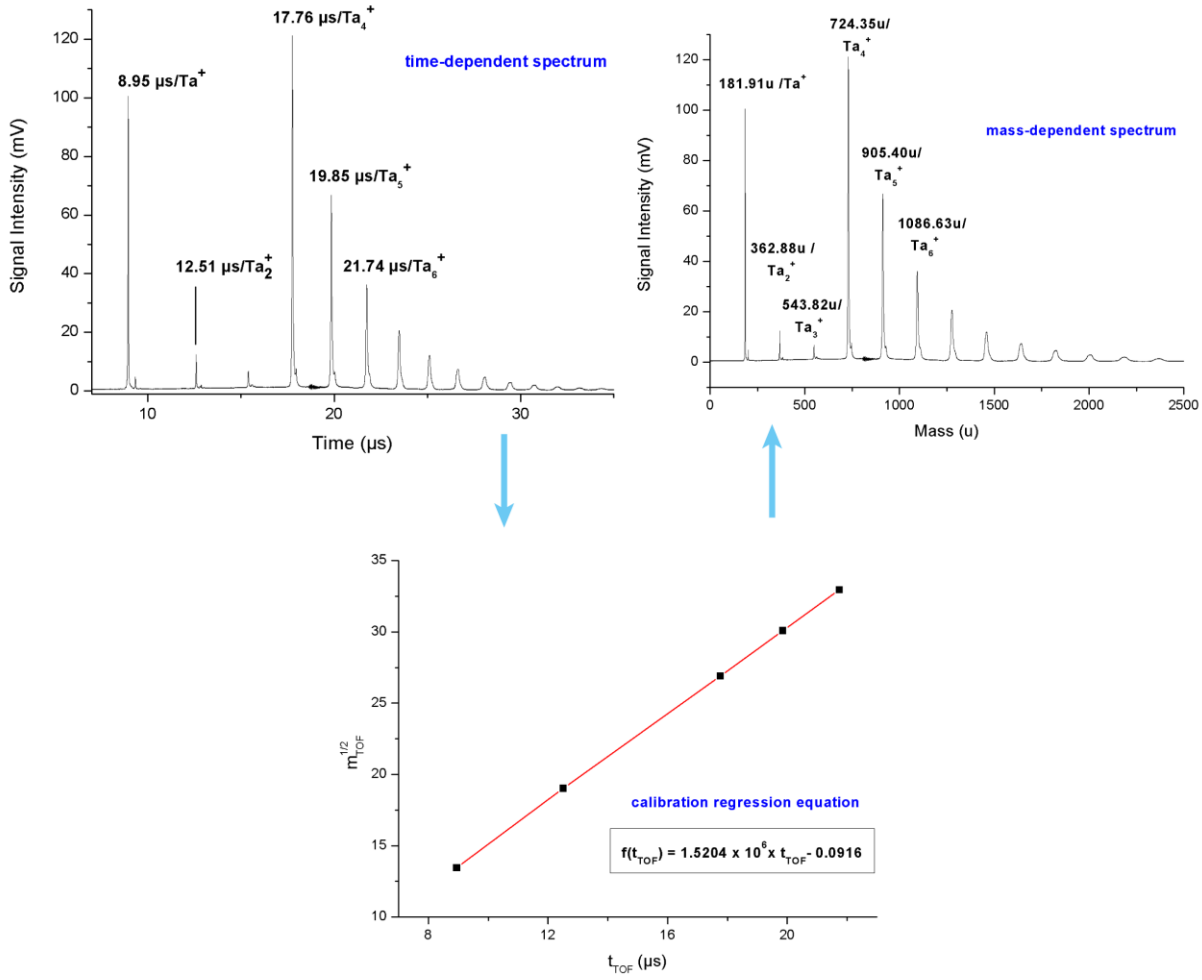


**Figure 3.26:** *Calibration procedure of the data obtained from the oscilloscope to generate a mass fit for the analysed metal clusters.*

Origin (*Origin Pro 8E by Origin Lab*), a software program for scientific graphing and data analysis, was utilised for plotting the resulting mass spectra.

# 4. Metal cluster formation

The laser vaporisation cluster source formed the basic element of the experimental setup. An extensive characterisation of the cluster output was essential for further cluster-adsorbate and spectroscopy experiments performed within the apparatus.

## 4.1 Investigated metal targets

Metal clusters of niobium, tantalum and rhodium were investigated during this work. All three play an important role in the field of catalysis. Tantalum and rhodium clusters are of special interest as both metals show an early transition in geometry from 2D to 3D structures.[30,39] These atoms build the basis for possible chiral structures, which can find application in asymmetric catalysis. Tantalum clusters also show C-H bond activation of alkanes[77] (methane activation). And rhodium clusters show N-O bond activation, which is of interest for exhaust chemistry.

These metal targets have only one major naturally occurring isotope which reduced the complexity of the resulting mass spectra. For every metal the cluster source settings were optimised to obtain the maximum cluster output at different size regimes.

### 4.1.1 Niobium

For the first experiments a niobium metal target was used in order to study the characteristics of the newly built cluster source.

Niobium is one of the five major refractory metals (high resistance to high heat and wear, along with tungsten, molybdenum, tantalum, and rhenium) and has melting point of 2477°C.[78] It is mostly used in stainless steel alloys. Niobium clusters are important to the field of catalysis and are used as a prototype system for studying the reactions of transition metal clusters. The reactions of niobium clusters with various types of molecules, such as $CO_2$[77], unsaturated hydrocarbons[79] or NO[80] have been investigated in order to understand

the reaction patterns and reactivity trends. Numerous industrial processes are catalysed by niobium oxides because of their highly reducible nature[79].

Manipulation of the cluster source settings enabled the tuning of the cluster generation within certain mass ranges. The production of small cationic niobium clusters was relatively simple to achieve. After a longer optimisation of the source settings an upper cluster size limit of $Nb_{22}$ was feasible. Figure 4.1 shows a mass spectrum with an asymmetric Gaussian-like cluster distribution ($Nb_n^+$, n=1-22) with $Nb_7^+$ as the species with the highest intensity (8 mV) due to the optimisation of the cluster distribution for this mass regime. Intensities of more than 20 mV (corresponds to ~ 10.000 ions) were achieved for $Nb_7^+$ with optimised cluster source settings.

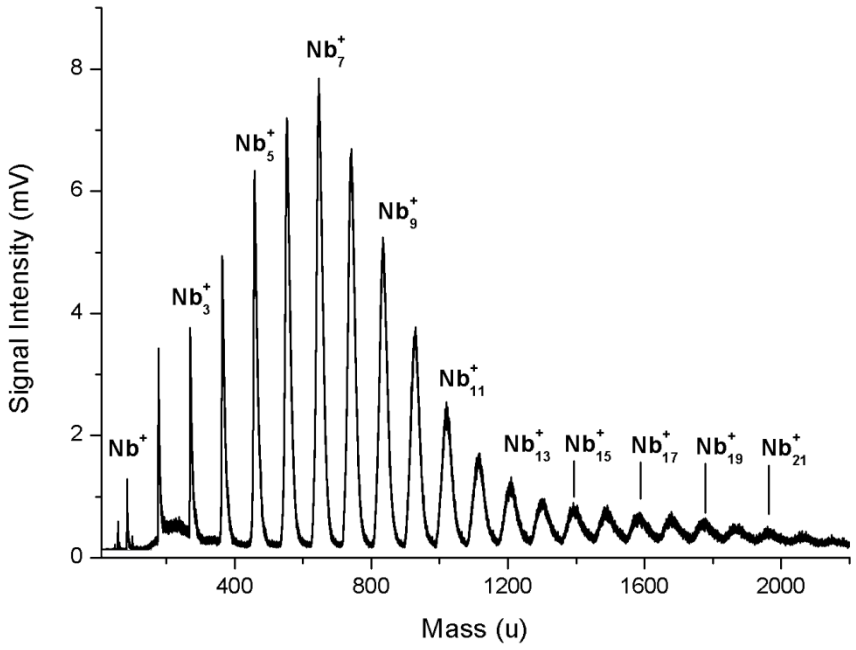


**Figure 4.1:** *Mass spectrum of nascent cationic niobium clusters.*

The increasing broadening of the peaks with cluster size seen in this Figure 4.1 was caused by a very low mass resolution of 31 (**M**($Nb_7^+$) = 650.10 u, **ΔM** = 20.56 u). This experiment was a first proof of principle for the operation of the cluster source and it was shown that niobium clusters of a wide range of cluster sizes could be produced with sufficient intensity for further study.

## 4.1.2 Tantalum

Tantalum is located directly below niobium in the periodic table and shows very similar chemical properties. It is also one of the most refractory metals and has a melting point of 3017°C.[81] Due to its chemical inertness the two main fields of application for tantalum are in medical implants and electronic equipment.[82] It has two natural appearing isotopes with $^{181}$Ta being the major isotope with a natural abundance of 99.998 % and is therefore the only isotope seen in the mass spectra. Tantalum clusters are of equal interest in catalysis as niobium. The oxide species show catalytic properties, e.g in the selective oxidation of 2-thiomethyl-4,6-dimethyl-pyrimidine[83]. Bare tantalum clusters are found to activate nitrogen on the cluster surface, which is an important step in the heterogeneous catalytic synthesis of ammonia[84]. The activation of C-H bonds in alkanes is another relevant application. Methane is one of the most prevalent green house gases. Therefore, the conversion into methanol is of great demand and interest as methanol is seen as a possible alternative energy source. First studies show a catalytic activity of silica-supported tantalum clusters for ethane conversion into methane and propane[85].

A typical **cationic tantalum cluster** distribution is shown in Figure 4.2. For cluster sizes $Ta_{1-5}^+$ a small amount of the mono oxide species was observed and is assumed to arise from contamination of the vacuum. The cluster distribution did not follow a classical Gaussian-like trend. The signal intensities showed a steep decrease from the monomer to the dimer and trimer. The signal corresponding to $Ta_4^+$ showed the highest intensity for the cluster source settings used. The mass resolution was measured to be 182 (**M**($Ta_4^+$) = 729.69 u, **ΔM** = 4.00 u). A better mass resolution could be achieved using different cluster source conditions.

$Ta_2^+$ and $Ta_3^+$ remained as the least abundant cluster species regardless of the cluster source settings used and the peaks intensities did not change significantly. Instead, the formation of $Ta_4^+$ seemed to be favoured during most experiments with tantalum, so long as the cluster source was not optimised for very large clusters ($Ta_n^+$, n > 20). Suzuki *et al.*[86] showed time-of-flight mass spectra recorded for cationic niobium and tantalum clusters generated by a laser vapourisation cluster source. It was found that similar to the results presented in this work, $Ta_4^+$ showed a very high abundance and $Ta_2^+$ and $Ta_3^+$ a very low intensity

compared to the other cluster sizes. A possible reason for the low intensities of the dimer and trimer could arise from neutralisation processes of the cationic species by electrons created during the cluster formation process. However, no other cluster size showed a similar behaviour, which leads to the assumption that the low intensities are due to size effects. Interestingly, physical properties of the dimer and trimer such as the IPs, dissociation energies or VDEs presented in Chapter 2.4, did not show any peculiarities when compared with other similarly sized clusters.

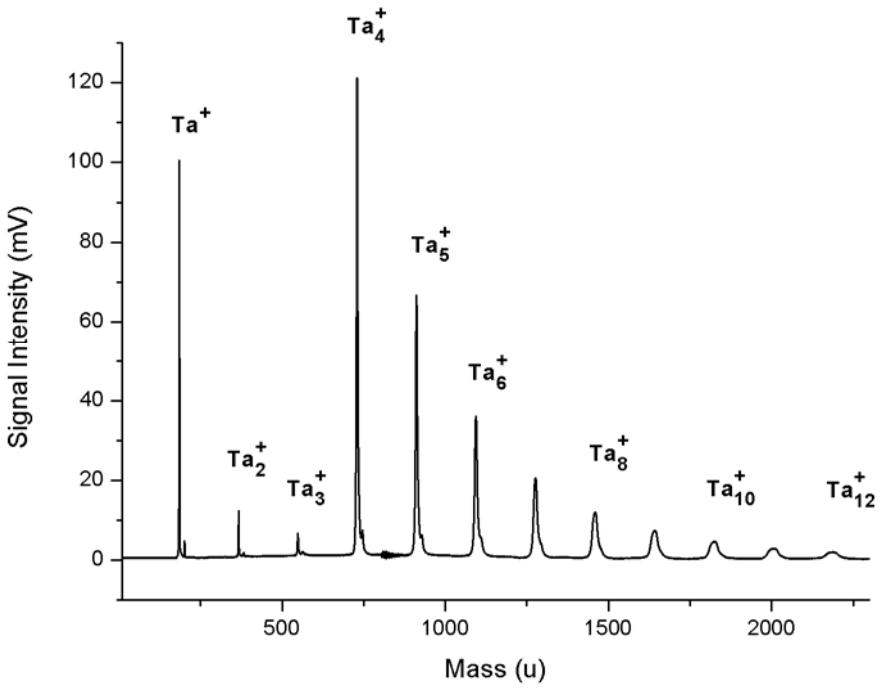


**Figure 4.2:** *Mass distribution observed for nascent cationic tantalum clusters with the cluster source tuned for maximum intensity of $Ta_4^+$.*

The early change from 2D- to 3D- configuration[41] occurs between the trimer and tetramer, with $Ta_3$ assigned to a triangular geometry[39] and $Ta_4$ to a tetrahedral geometry.[87] This early geometry transition could be another argument to explain the relative intensities of these species. No concrete explanation for this effect was found in literature. On the one hand, photoionisation experiments of neutral tantalum clusters presented in Chapter 6.1 could confirm the enhanced neutralisation of $Ta_2^+$ and $Ta_3^+$ in the cluster source. The recorded ionisation spectrum (see Figure 6.1) showed significantly higher signal intensities for $Ta_2^+$ and $Ta_3^+$ than for the cations generated in the cluster source. On the other hand,

fragmentation of larger clusters occurring by using photoionisation could also contribute to the higher abundance of the ionised dimer and trimer.

**Anionic tantalum clusters** were investigated using the anion mode of the experimental settings. A cluster size distribution of n = 3-12 was optimised (see Figure 4.3). Peaks corresponding to the mono oxide species of the clusters were observed similar to the cationic clusters. The noise present between $Ta_5^-$ and $Ta_6^-$ corresponded to the triggering (turning off) of the TOF-MS electrodes. The most abundant species in Figure 4.3 is $Ta_5^-$ due to the optimised mass range. The spectrum showed a steep increase of signal intensity from the trimer towards $Ta_5^-$ and a more gradual decrease from $Ta_6^-$ to higher cluster sizes. The intensity profile of the anionic cluster distribution was found to be similar to that of the cationic species.

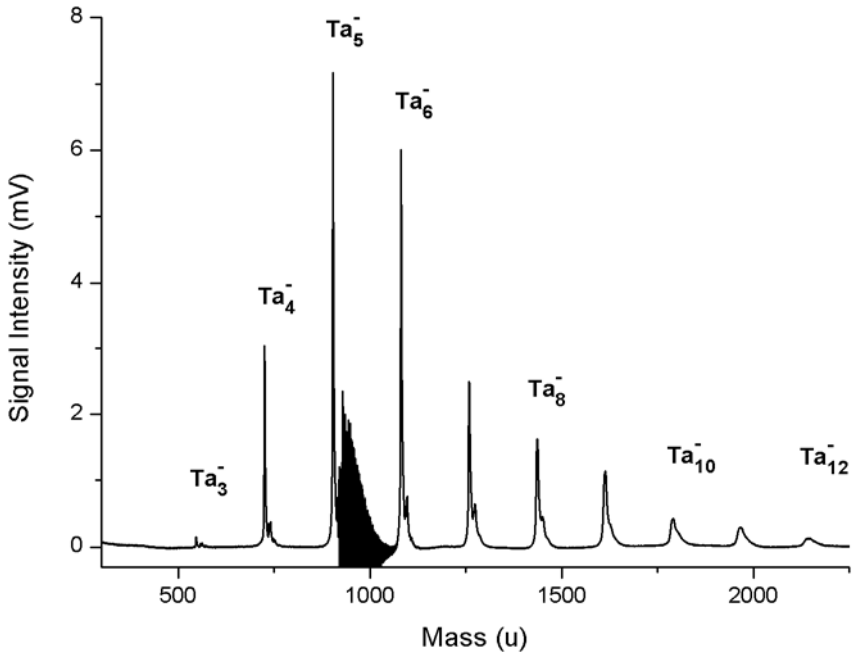


**Figure 4.3:** *Mass distribution of anionic tantalum clusters with maximum intensity observed for $Ta_5^-$.*

The mass resolution of 333 (**M**($Ta_5^-$) = 902.43 u, **ΔM** = 2.71u) is almost double that of the cation spectrum. This phenomenon was observed during numerous experiments. This might be explained by the fact that the anions seemed to undergo a more efficient cooling process with the helium carrier gas. Otherwise, the intensities of the anionic species were considerably reduced in intensity compared to the cationic cluster intensities. This might be due to electron attachment only being efficient for particularly cold clusters.

## 4.1.3 Rhodium

Rhodium is an inert transition metal and consists of only one naturally occurring isotope $^{103}Rh$. As it is resistant against corrosion it is used in high temperature and corrosion-resistive coatings. The main industrial application is catalytic conversion of automobile exhaust gases due to the catalytic activity of rhodium towards CO and NO.[88] In heterogeneous catalysis, rhodium nanoparticles complexed with organic ligands are utilised for several reactions such as hydroformylation of styrenes[89] and polymerisation of phenylacetylene[90] among others.

Investigation into the feasibility of generating larger clusters ($Rh_n$, n = 40-80) produced with the cluster source was conducted with **cationic rhodium clusters**. The mass spectrum which is presented below in Figure 4.4 contains a cluster size distribution ranging from $Rh^+$ up to $Rh_{88}^+$.

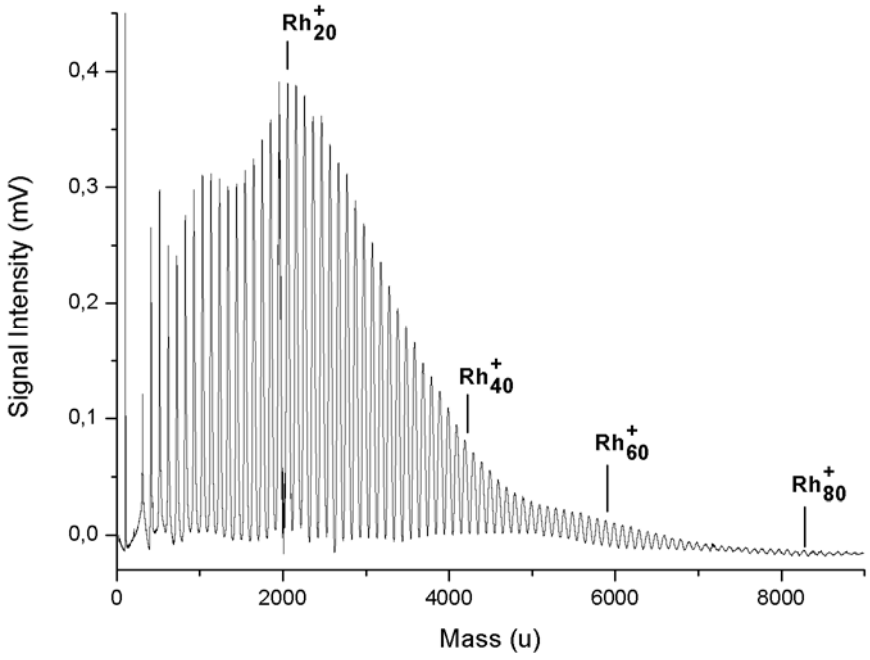


**Figure 4.4:** *Achievable mass range n=1-80 of cationic rhodium clusters.*

The higher mass range was considerably increased by adjusting the voltage applied to the deflector plates. This caused an enhancement of the number of heavier clusters reaching the detector. The signal for $Rh^+$ was cut off in the spectrum in order to ease viewing of the

cluster distribution. The most dominant cluster size following the monomer corresponds to $Rh_{20}^+$ with 0.37 mV signal intensity. A mass resolution of 56 (***M***($Rh_{19}^+$) = 1965.70 u, ***ΔM*** = 35.30 u) was measured for this experiment. The noise which appeared next to $Nb_{19}^+$ was caused by triggering of the TOF-MS electrodes (turning off). As $Rh_{88}^+$ has a mass of 9069.73 u (approximately $Au_{46}$) three crucial elements were successfully proven in this experiment: a) the formation of heavy metal clusters by the newly built cluster source via optimisation of the source settings, b) the steering of the heavy charged species via the implemented ion optics (i.e. Einzel lenses, TOF-MS electrodes), c) size selection via the TOF-MS.

A typical mass spectrum recorded for **anionic rhodium clusters** with a mass distribution of n = 3-26 is shown in Figure 4.5.

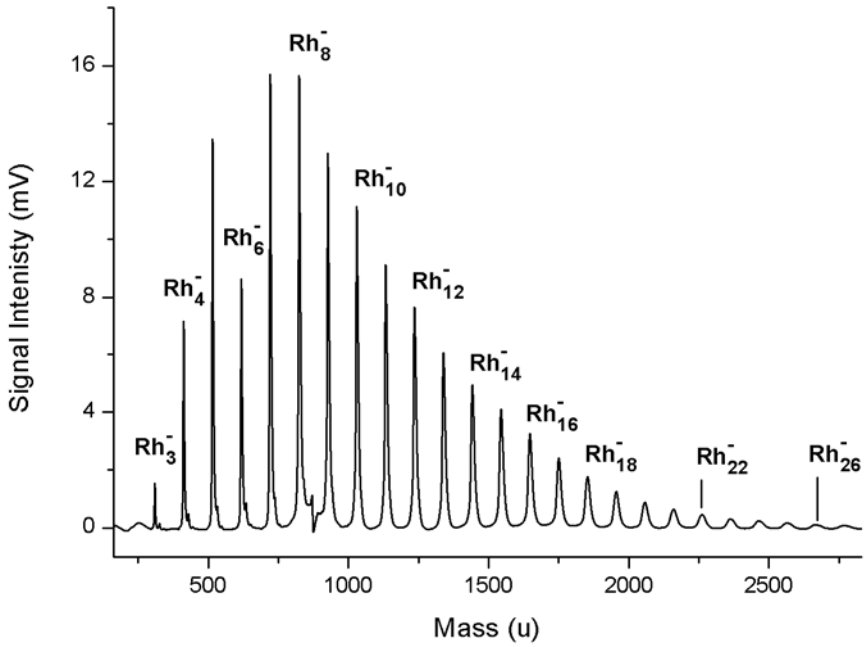


**Figure 4.5:** *Mass distribution of anionic rhodium clusters $Rh_n^-$, n=3-27.*

After optimisation of the source settings a maximum intensity of over 16 mV for $Rh_7^-$ was achieved. In general the cluster size distribution can be described as an asymmetric Gaussian-like shape with a steep signal increase up to the maximum at $Rh_7^-$ and a smooth decrease to higher masses. Small amounts of a signal artifact appeared next to $Rh_8^-$, which arose from the triggering of the TOF-MS electrodes. The intensity of $Rh_6^-$ was observed to be

characteristically lower than that of the neighbouring cluster signals. This phenomenon was observed regardless of the experimental settings used. The mass resolution was measured to be 102 ($\boldsymbol{M}(Rh_8^-)$ = 823.2 u, $\boldsymbol{\Delta M}$ = 8.07 u). This is exactly double the resolution of the cationic rhodium species that were observed. Again, as mentioned previously, anions might undergo a more efficient cooling, resulting in a better resolution in the mass spectrum. The signals of anionic rhodium clusters were in general more intense and better resolved than the cations. The time distribution of anionic clusters for both rhodium and tantalum was found to be shorter than for the cations. The term time distribution refers to a spread of the cluster beam over a certain time window, e.g. in the TOF-MS ion source. This could have originated from the manner of cluster extraction or the temporal spread of the cluster beam due to a broader velocity distribution.

## 4.2 Characterisation of the temporal distribution of the cluster beam

### 4.2.1 Characterisation by time-of-flight measurements

The time spread of the cluster beam at the position of the TOF-MS ion source was investigated by changing the TOF-MS delay times with respect to the time of cluster formation. Different time distributions were found for cationic and anionic clusters as mentioned previously in Chapter 4.1.2. A plot of several mass spectra recorded for cationic tantalum clusters at different TOF extraction times is presented below. The cluster source settings were held constant and the delay of the TOF-MS was changed over a range of approximately 2000 µs. The cluster source settings were originally optimised for $Ta_4^+$. Small signal intensities appeared at a TOF extraction delay time of 950 µs. By increasing the delay time up to 1400 µs the signal intensities for all clusters visible in the spectra increased significantly. Heavier clusters especially showed better defined peak shapes. Increasing the delay further caused a decline of the intensities for all cluster sizes. $Ta_8^+$ and heavier clusters

started to disappear completely at longer extraction delays. The normalised intensity progression of $Ta_4^+$ versus the TOF extraction time is shown in Figure 4.7.

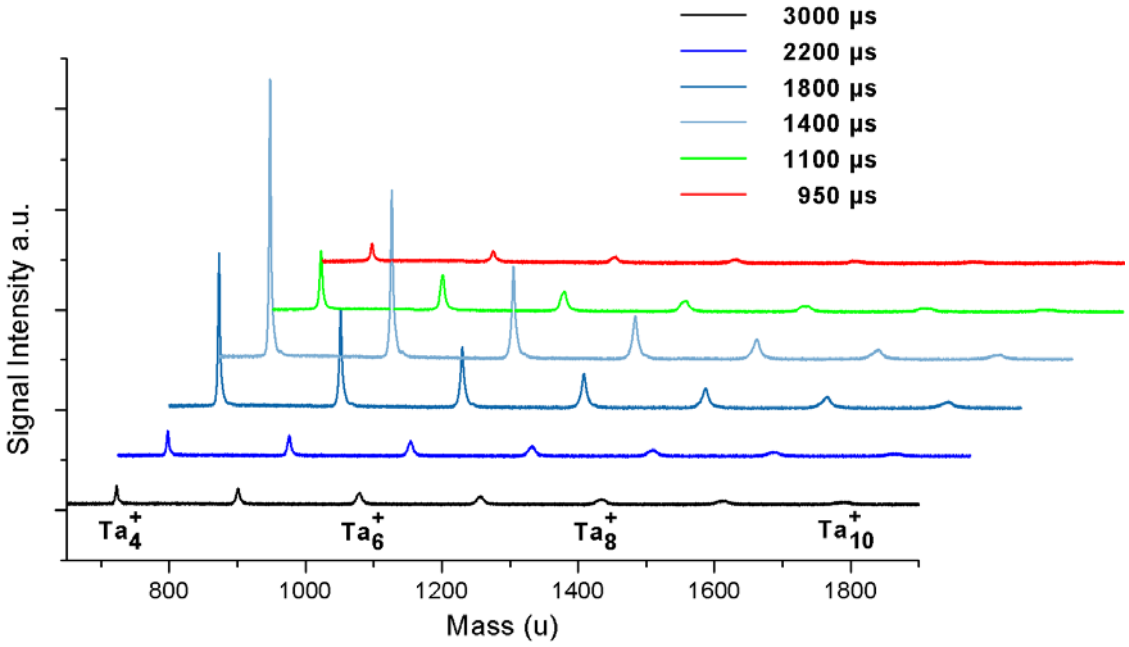


**Figure 4.6:** *Cluster size distribution of cationic tantalum clusters recorded at different TOF-MS delays.*

Three time regimes can be determined from Figure 4.7. From 950 µs up to 1400 µs the signal intensity showed a steep increase up to a maximum at 1400 µs. Increasing the delay further up to 2200 µs revealed a more gradual decay. For longer delay times the intensity plateaued and the amount of extracted clusters did not change significantly. This result showed that the density of the expanded cationic clusters did not remain constant over time. For certain cluster source settings the cluster density was enhanced for a certain TOF-MS extraction time, which could be seen as a peak-like temporal distribution. This experiment proved the long cluster beam time spread, approximately 1200 µs, of the cationic tantalum clusters. For anionic clusters a much shorter time distribution, approximately 500 µs, was observed during the optimisation of the experimental parameters during several experiments. The immense time spread of cationic clusters could originate from the expansion conditions in the cluster source or from an insufficient cooling by the helium carrier gas. The time spread can be influenced slightly by the settings of the cluster source. Nevertheless, time compression of the cationic species was not achieved.

The same phenomenon of different time spreads was observed for cationic and anionic rhodium clusters, and may occur for all metal clusters produced in this type of cluster source. Therefore, it can be concluded that the nature of cluster formation and expansion differs depending on the cluster type (cationic and anionic).

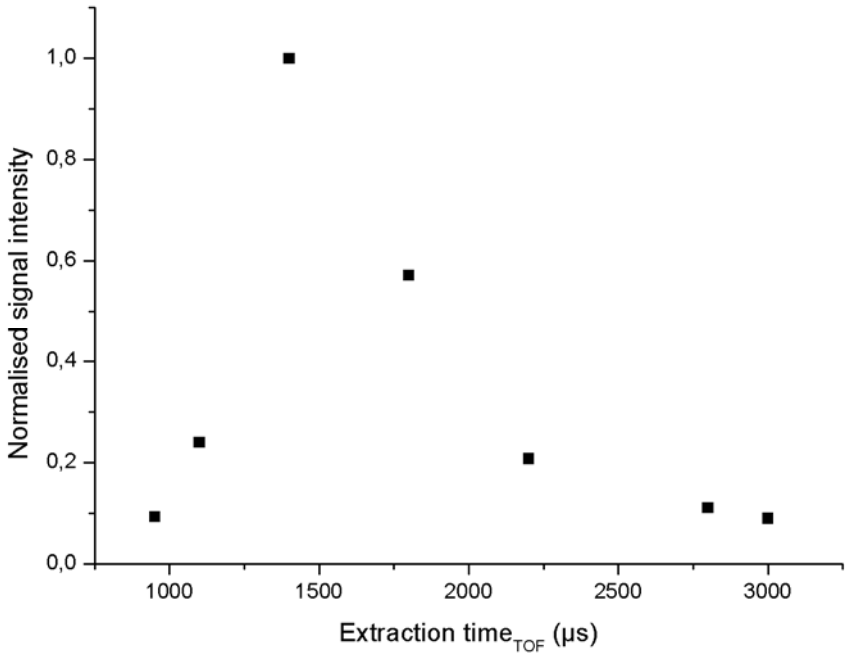


**Figure 4.7:** *Signal intensity of $Ta_4^+$ dependent on the delay of the TOF-extraction time.*

## 4.2.2 Characterisation by a capacitive decoupled device

A home built capacitively decoupled device (Figure 4.8) was used to measure and further investigate the time distribution of the nascent ions on the optical elements located before the TOF-MS assembly.

The idea of this device was based on the function of a picoammeter for optimising the cluster source conditions and ion guidance. A picoammeter is an instrument that is used to measure very low DC (Direct Current) electrical current in the picoampere range. By applying an adjustable voltage through the source connection on to the ion optical element, charged clusters are attracted and strike the element. The low current caused by the neutralisation of the cluster species on the ion optics can be measured.


**Figure 4.8:** *Home built capacitive decoupled device used to measure the time distribution of the cluster beam on every ion optic.*

The picoammeter was normally used to optimise and maximise the cluster current by changing the source settings, but did not provide information on the time distribution of the ions. In contrast to the picoammeter, the home built device can decouple the current via a capacitor and send the signal to an oscilloscope where a time dependent current signal was recorded. In Figure 4.9 time distribution spectra are shown for cationic niobium clusters which were measured on three successive einzel lenses (see Chapter 3.2). The centre plate of each einzel lens was connected to a power supply and several hundred volts of negative polarity (to attract the cationic species) were applied. For measurements on einzel lens number one all other einzel lenses were set to a zero potential. Measurements on the three other lenses were performed in the same manner but with voltages applied to the previous lenses to guide the cationic species towards the lens of interest.

The signal for einzel lens one shows a very steep increase during the first few microseconds. This could have originated from a high density of charged species due to the smaller distance to the nozzle of the cluster source. The appearance time of signal (A) was very early and cannot correspond to the cluster species. It has to originate from lighter species (i.e. $He^+$) created by the laser or species from the cluster source that are not entrained in the carrier gas pulse. After the signal increased a short plateau can be observed which leads to a second peak shaped signal (B) around 150 µs. The origin of this peak cannot be clarified, but could have a similar origin to that of the first peak. The most dominant peak (C) arises

around 300 µs. Due to the signal intensity and time of appearance this peak could correspond to the cationic niobium clusters. The peak width spreads from 200 µs to almost 800 µs. Changing the source settings did not have a significant impact on this distribution of 600 µs.

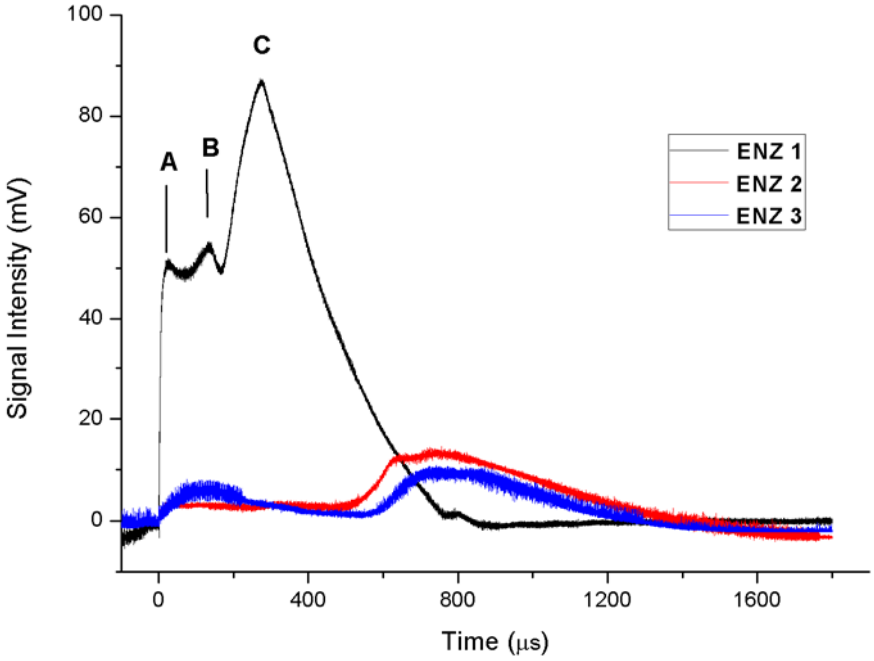


**Figure 4.9:** *Time distribution measurement of cationic niobium clusters via an in house built capacitively decoupled device on three successive einzel lenses (ENZ).*

The measurements performed on the three other lenses showed a much broader distribution in time than for einzel lens number one. Between 0 and 700 µs only a flat plateau is observed that showed nearly no signal intensity. A broad peak arose for einzel lens two and three. For lens two the peak was observed earlier than for lens three, which can be explained by the shorter distance between nozzle and einzel lens two. For both ion optics the time distribution spread out from 700 µs up to 1200 µs and the peak signal intensity is reduced considerably compared to the measurement on einzel lens one. At einzel lens one the time distribution at the maximum of the peak height was significantly shorter and narrower, whereas measurements on the successive lenses did not show such a feature. Manipulation of the source settings did not seem to affect on the time profile of the cation signal. The time shift for the signal maximum from einzel lens one to two measured about 400 µs while between lens two and three the shift was less than 100 µs. This

observation probably originated from applying high voltages onto the lens/lenses previous to the one on which the signal was measured, which caused a time spread of the cluster beam. The increasing time spread is in good agreement with the time-of-flight measurements which have been shown previously.

# 5. Adsorbate introduction

The precise control of catalyst design is an important strategy for industry as well as for fundamental research. Various different approaches are available today to produce a catalyst which fulfils special demands.[9] The creation of a highly enantioselective system is of special interest in heterogeneous catalysis.[7] In this chapter several test systems are presented which present a first example of the possibilities offered by the current experiment due to cluster–adsorbate interaction in the gas phase.

## 5.1 Introduction via piezo valve

Various molecule injection methods were explored during this work. The first adsorbate experiments were performed using the second piezo valve (see Chapter 3.1). The liquid organic compounds were stored in a glass ampoule which was connected directly to the gas line of the piezo valve. Before experiments with a new organic compound were performed the ampoule was cleaned with acetone, dried an then rinsed repeatedly with the new compound to remove contamination from the previous substance. For the first experiments organic chemicals with a high vapour pressure were chosen. The intended delivery mechanism was thought to be dominated by the equilibrium between the liquid and vapour phase of the organic compound. By operating the piezo valve the overall pressure in the gas phase line dropped until the vapour pressure of the liquid organic sample provided the dominant backing pressure. Thus, the phase equilibrium of the organic compound would have shifted towards the favour of a gaseous state. Therefore, a helium carrier gas was not required. Later on a bubbler with channelled helium carrier gas (see Chapter 3.1) replaced the glass ampoule in order to enhance dosing control of the adsorbate. Another important feature to be considered in choosing an organic compound is the molecular mass. If the masses of the clusters and adsorbate were too similar, an isobaric interference can result and therefore, a clear differentiation between bare metal cluster and cluster-adsorbate complex would be impeded.

## 5.1.1 Niobium clusters plus adsorbates

Niobium clusters (Nb = 93 u) were chosen as a first test system because the clustering process was simple to perform. In the first adsorbate experiments **acetone** was dosed onto the niobium clusters. Acetone (IUPAC nomenclature: 2-propanone, Figure 5.1) is an achiral substance which exists as a liquid at room temperature with a very high vapour pressure (0.246 bar at 20°C )[91] and a molecular mass of 58 u. A few millilitres of acetone were filled into the glass ampoule which was subsequently attached to the second piezo valve. The experiment was operated in cation mode with a positive polarity applied to the pulsed repeller and extractor plates used in the TOF-MS.

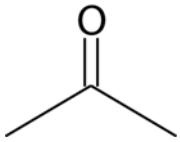


**Figure 5.1:** *Structure of acetone (58 u).*

The experimental settings were optimised for cationic metal species of $Nb_n^+$ with n = 1 – 2. In the experiments presented in the following paragraph the second piezo valve was triggered to pulse acetone vapour into the expansion channel of the nozzle. Adjustment of the pulse width and the voltage applied to the valve changed the mass spectrum considerably (Figure 5.2). The spectrum shows three main groups of signals, the bare monomer and dimer, metal oxide species and niobium with adsorbed fragments of acetone. The signal corresponding to the niobium atom retained a large intensity upon the addition of acetone, whereas the dimer almost disappeared. Through analysis of the data it was found that none of the masses corresponding to the metal–adsorbate complexes (highlighted with blue text in the spectrum) equal the molecular mass of acetone on niobium. The peaks assigned to masses of + 30 u and + 24 u can be linked to fragments of acetone that have lost one or two carbon atoms, respectively. A dehydrogenated $C_2$ unit can be assigned to the signal at + 24 u and the signal for + 30 u to ethane ($C_2H_6$) or methanal ($CH_2O$). A mass of + 40 u may correspond to propadiene ($CH_2CCH_2$). The higher signal intensities of the niobium-oxide species could be explained by deoxygenation of acetone. Niobium and niobium monoxide cations are known to undergo a **deoxygenation reaction**

with $CO_2$[77] ($Nb^+ + CO_2 \rightarrow NbO^+ + O + C$). This reaction could occur if the carbonyl group (CO) of the acetone interacts similarly as the CO unit in $CO_2$.

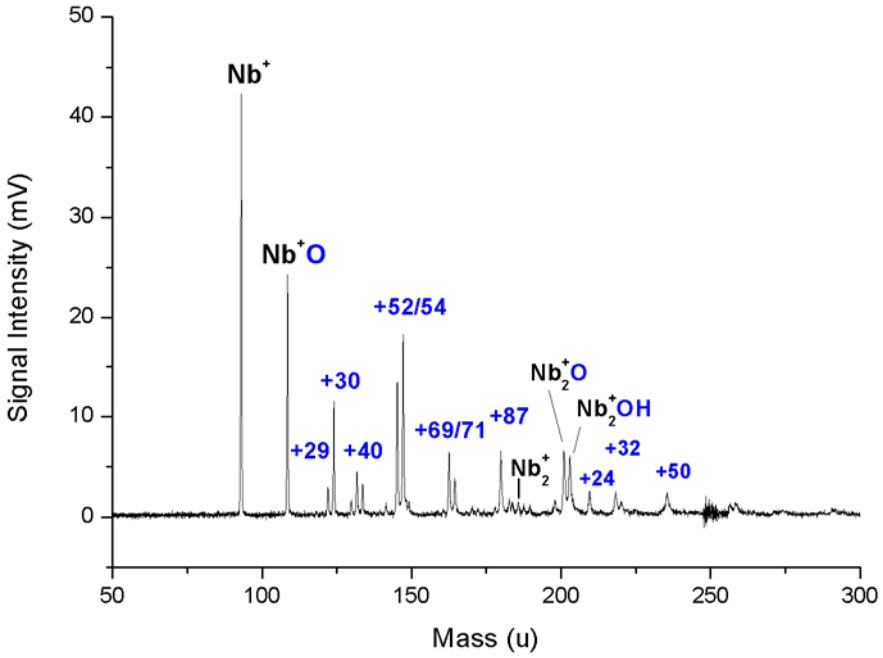


**Figure 5.2:** *Mass spectrum of $Nb^+$ and $Nb_2^+$ clusters with dosed acetone (58 u).*

*Castleman et al.*[92] investigated reactions of various niobium oxide clusters with acetone. It was shown that species like $Nb_3O_7^+$ have a strong reactivity towards the abstraction of one oxygen atom from oxygen–containing molecules such as acetone. Further oxidation is believed to originate from the metal rich character of the metal–oxide species. The niobium–oxygen bond strength is very high and the energy release from the formation of this bond might contribute to bond breaking in acetone. As the investigated clusters in this work were mainly bare metal clusters, the tendency for oxidation should be even higher than the species *Castleman et al.* worked on.

The signals which arose at masses of + 52/54 u can be assigned to **dehydrogenated** acetone fragments. According to the results in literature (see Chapter 2.5) niobium clusters have been shown to dehydrogenate a variety of species, i.e. primary alcohols[46] and benzene[93]. Dehydrogenation of acetone and its fragments could be caused by the electron deficit of niobium cations. When the adsorbate attaches to the metal C-H cleavage occurs. The signal group with mass + 52/54 u does not appear in the spectrum for $Nb_2^+$. As the signal

intensities on the dimer are low in comparison to the monomer, an accurate analysis of the adsorbate peaks is not feasible for the dimer.

Since a molecular attachment of acetone was not observed due to fragmentation and possible reactions with the cationic niobium species, another compound was used. **Ethanol** is a colourless liquid at room temperature with a molecular mass of 46 u and a vapour pressure of 58 mbar.[94]

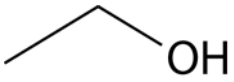


**Figure 5.3:** *Structure of ethanol (46 u).*

The experimental settings of the cluster source were optimised as described in Chapter 3.1 to control the amount of adsorbate vapour dosed into the cluster beam. One important adjustable setting in this regard is the pulse width of the second piezo valve, which can be varied as much as several hundreds of microseconds. Increasing the pulse width should cause an enhancement of the cluster–adsorbate species due to the higher number of molecules in a single pulse. Figure 5.4 shows a sample of mass spectra recorded with varied pulse widths for the second piezo valve. The optimised mass range is set to $Nb^+$ and $Nb_2^+$. By increasing the width a significant change in the spectra is observed. For a second piezo pulse width of 60 µs only one adsorbate signal, located at + 42 u appears. At longer pulse widths many more peaks corresponding to the adsorbed species arose. The peak at + 42 u could be assigned to adsorption of the dehydrogenated ethanol species CHCOH. As described for acetone previously, dehydrogenation of primary alcohols on niobium is well known in literature.[46] At 100 µs the signal intensity of $NbO^+$/OH increases considerably due to possible deoxygenation of the ethanol, caused by the high bond strength of Nb-O [46]. The signal group of + 34/35 u could possibly be connected to this assumption. The signals at + 34 u and 35 u can be assigned as two OH groups and OH plus $H_2O$, respectively. The most interesting feature of the spectra is the signal arising for molecularly adsorbed ethanol (+46 u) on the monomer for piezo pulse widths of 140 and 180 µs. It is the first time that a molecular attachment of an adsorbate was observed during this work. At a pulse width of 180 µs the Nb-ethanol cation is the dominant species in the spectrum.

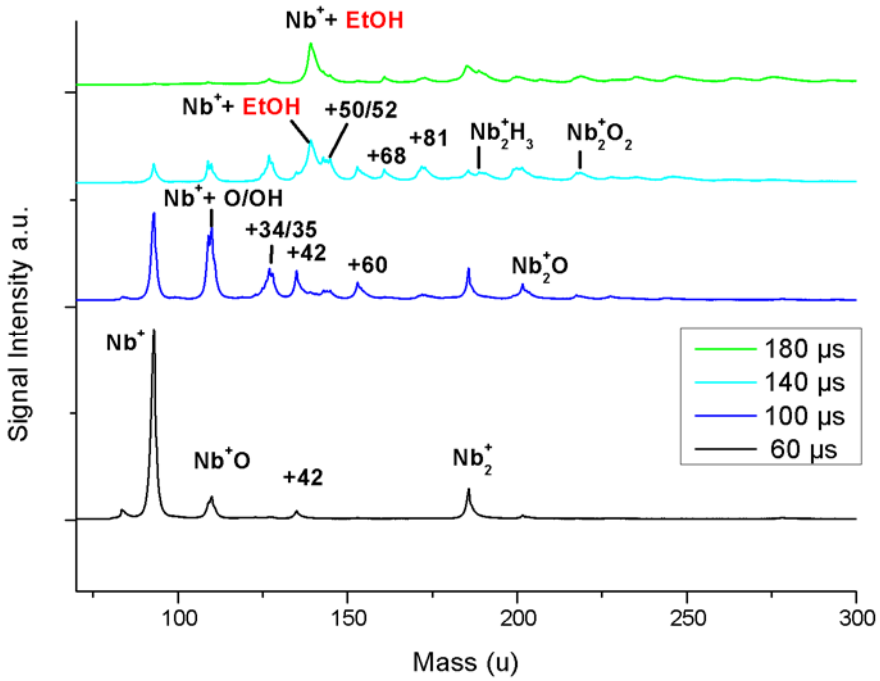


**Figure 5.4** *Mass spectra of $Nb^+$ and $Nb_2^+$ clusters with dosed ethanol (46 u) at different pulse widths for the second piezo valve.*

*Castleman et al.*[92] observed an increasing ratio of molecularly adsorbed species with increasing pressure of the neutral reactant. As the introduction of ethanol through the inlet valve only depended on the vapour pressure in this experiment, the pressure could not have been increased without heating the entire gas inlet assembly. However, the opening time of the piezo valve was adjustable, and could be used to create a gas volume which contained more ethanol molecules. The coordination of the monomer to ethanol occurs via the oxygen atom.[46]

While the adsorbed ethanol signal increased with longer pulse widths, the signals corresponding to $Nb^+$ and $Nb_2^+$ reduced in intensity. This observation was made in several experiments with this experimental setup. Due to the adsorbate introduction a quenching of the bare metal species in the cluster source might occur. Also neutralisation of the cationic monomer and dimer could take place, caused by the interaction with the adsorbate vapour or by collisions with the wall of the expansion channel. Changes in the cluster source settings and therefore, changes in the expansion conditions during the experiment cannot be excluded either.

At piezo pulse widths ≥ 100 µs peaks corresponding to adsorbate species that are heavier than ethanol appear. A mass of + 60 u could be correlated to $EtOH+CH_2$. The $CH_2$ unit could

originate from a C-C bond cleavage in an ethanol molecule and could potentially lead to the formation of methanol ($CH_3OH$). Nevertheless, a signal at a mass difference of 32 u was not observed. With the appearance of ethanol at a piezo pulse width of 140 µs several more signals arise. As all peaks are assigned to masses higher than a difference of + 46 u, it is probable that these peaks arise due to the adsorption of multiple ethanol molecules or corresponding fragments.

As described earlier, the signal intensity of the monomer nearly disappears with longer pulse width settings. Due to the increasing intensity of the ethanol peak it could be concluded that some of the intensity of the bare monomer species is transformed into intensity of the metal-adsorbate species. However, the signal increase seen for the cluster–adsorbate species is much less than the decrease of the monomer intensity. This would support the idea of the disruption of the cluster expansion. Increasing the pulse width up to 200 µs did not show an enhancement of the cluster-adsorbate species. If the piezo pulse width was set longer than 200 µs almost every species disappeared from the spectrum.

Adsorption experiments with acetone showed the first results of the interaction between metal cluster and organic molecule in the experimental setup. The observed fragmentation may have occurred due to the clustering conditions such as temperature or a less efficient pulsing of the acetone vapour to the cluster beam. Cationic niobium clusters were shown to adsorb ethanol molecularly when the pulse settings of the second piezo valve were increased above a certain threshold. This result emphasises the importance of the adsorbate valve settings.

## 5.1.2 Rhodium clusters plus adsorbates

To investigate adsorbate attachment dependence on the metal species, Rhodium was chosen as another target material. Rhodium clusters have a high potential for intrinsic chirality as a transition from 2D to 3D geometry has been observed for very small cluster sizes ($Rh_n^+$, n = 3 – 4).[32] Rhodium clusters are very stable and are similarly easy to produce as niobium clusters, even up to a size range of n=88 as shown in Chapter 4.2. A first

experiment with rhodium clusters was carried out with a racemic mixture of **2-butanol**. 2-butanol is one of the smallest chiral substances, with the chiral centre located at the carbon atom bound to the hydroxyl group (see Figure 5.5). It is a liquid with a mass of 74 u and a vapour pressure of 16.7 mbar at room temperature.[95]

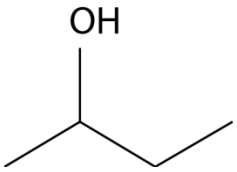


**Figure 5.5:** *Structure of 2-butanol (74 u) without stereo specific information.*

Figure 5.6 shows a typical spectrum of rhodium cations and the resulting adsorbed species after addition of 2-butanol. The dominant species observed for $Rh_2^+$ and $Rh_3^+$ are the hydroxyl complexes. As already seen for ethanol on niobium, the loss of the hydroxyl group is a main reaction path for the interaction of metal and alcohol.

One signal group with masses of + 44/46 u is observed for $Rh_n^+$, n=2-3. These signals may correspond to fragments of 2-butanol with a decreasing degree of dehydrogenation. The peaks with masses 44 u and 46 u more than the dimer would fit ethenone ($CH_2CO$) and acetaldehyde ($CH_3CHO$), respectively. Due to the optimisation of the cluster source settings for the rhodium dimer and trimer these signals are not visible for $Rh^+$. For the signal at an additional mass of 60 u the adsorbed species is assigned as the loss of a $CH_2$ unit from 2-butanol, similar to what was seen for niobium with ethanol. The added mass of 74 u could be assigned to an intact 2-butanol and is observed on $Rh_{1-3}^+$ whereas + 72 u is only visible for $Rh_2^+$ and + 76 u for $Rh^+$ and $Rh_2^+$. The signal at + 72 u could be caused by partial dehydrogenation of 2-butanol and + 76 u can be assigned to 2-butanol plus two additional adsorbed hydrogen atoms.

Dehydrogenation can be explained by the same mechanism as for niobium via C-H insertion. Mass differences higher than the mass of 2-butanol might belong to 2-butanol and co-adsorbed fragments. A clear assignment of these species is not feasible and would be very speculative. The observed reaction and fragmentation products might be caused by effects of cluster temperature. The coordination of 2-butanol to rhodium clusters may occur via the oxygen atom of the hydroxyl group according to literature.[96]

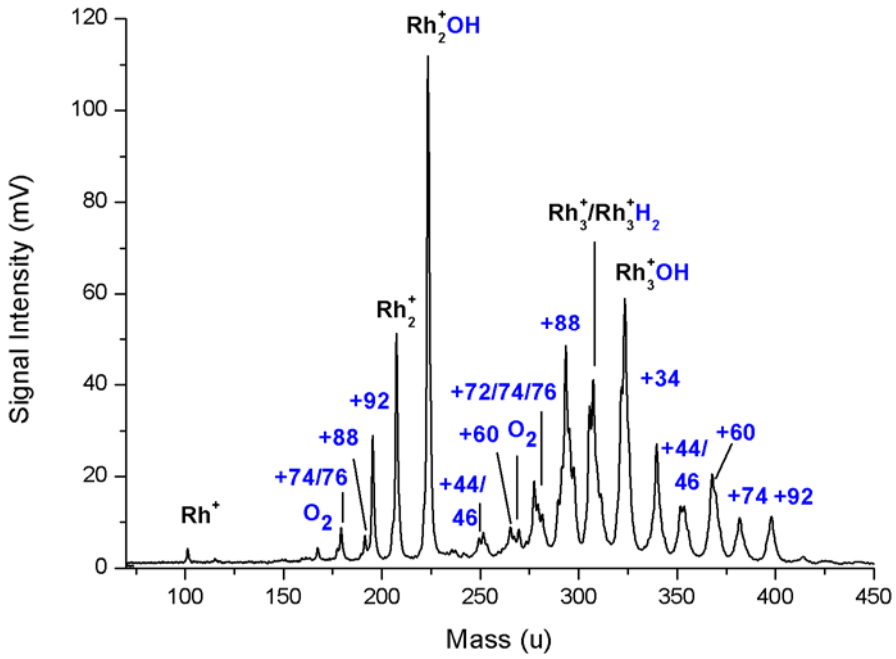


**Figure 5.6:** *Low mass range spectrum of $Rh^+$- $Rh_3^+$ with 2-butanol (rac., 74 u) added.*

The adsorption of molecular 2-butanol on cationic rhodium clusters is feasible, but significant fragmentation occurs in the investigated mass range. Dehydrogenation is observed, similar to what was seen for cationic niobium clusters. Therefore, it is quite possible for the stereochemical information for 2-butanol to be lost during this process.

Further adsorption experiments were performed with **(R)-(+)-limonene** (IUPAC: 1-methyl-4-(1-methylethenyl)-cyclohexene). Limonene (136 u) is a **chiral organic compound** with a vapour pressure of 1.9 mbar and exists as a liquid at room temperature and pressure.[97] Limonene was chosen because of its chirality, relatively high vapour pressure and more complex structure compared to 2-butanol.

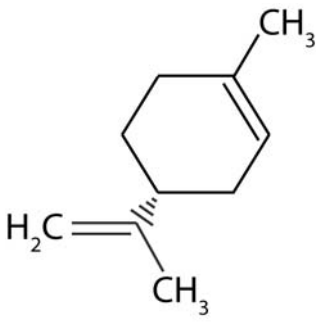


**Figure 5.7:** *Structure of (R)-+-limonene (136 u)*

The glass ampoule was filled with a few millilitres of (R)-(+)-limonene and channelled into the second piezo valve by a helium backing pressure of 2 bar. The recorded spectrum with a cluster size distribution of $Rh_n^+$, n = 3-11 is shown in Figure 5.8. Analysis of the mass spectrum indicates that no intact limonene molecules are attached on any considered cluster size.

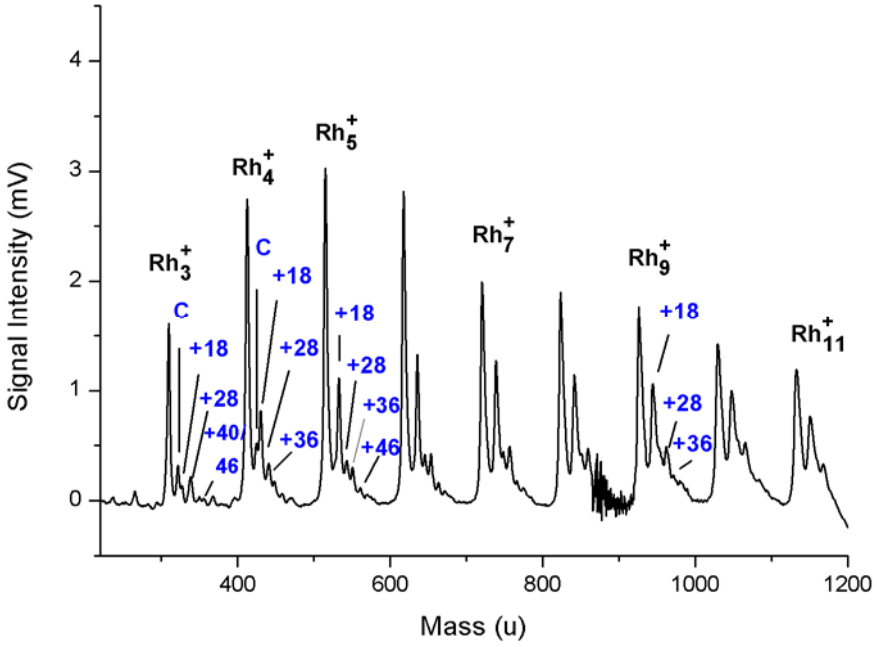


**Figure 5.8:** *Mass spectrum of cationic rhodium clusters n=3-11 with dosed (R)-(+)-limonene (136 u).*

If limonene (136 u) would be adsorbed on a rhodium cluster, the signal corresponding to this complex would appear at a mass difference of 33 u above than the next higher cluster (i.e. Rh = 103 u, limonene = 136 u). No signals corresponding to a mass of + 33 u were found. The signal analysis also showed a consistent adsorbate distribution. For almost every cluster size mass differences of + 18 u, + 28 u, + 36 u and + 40/46 u were observed. A mass of + 18 u would most likely correspond to adsorption of $H_2O$. This might have originated from impurities left in the ampoule after the cleaning procedure. A hint for dehydrogenation can be found at + 28 u (actual mass in the spectrum 130 u) which could correspond to a loss of five hydrogens from limonene. *Uggerud et al.*[57] showed that cationic rhodium clusters are able to dehydrogenate ethane and propane via a 1,1 - or 1,2 elimination mechanism. With increasing cluster size a signal of + 36 u appears and slightly increases. As this mass difference is slightly larger than for a possible adsorbed limonene (+ 33 u), a clear

assignment in this spectrum is not possible. Masses of + 40 u/46 u also could belong to adsorbed limonene plus a co-adsorbed fragment.

(R)-(+)-limonene is the first enantiopure compound used that possesses a higher structural complexity. Instead of molecular attachment, dehydrogenation and fragmentation were observed. Data analysis for higher masses was not possible due to insufficient mass resolution. Due to the absence of polar groups such as OH, SH or NH, which would enhance the adsorption strength to the cluster, (R)-(+)-limonene is not a suitable compound to study metal cluster-adsorbate interactions.

A second enantiopure substance was investigated during adsorption experiments with cationic rhodium clusters. **(R)-(+)-pulegone** (IUPAC nomenclature: (R)-5-methyl-2-(1-methylethyllidine)cyclohexanone, 152 u) is a liquid **chiral** organic compound that was chosen due to its high vapour pressure of 184 mbar at 25°C.[98]

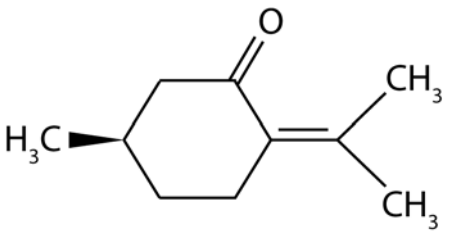


**Figure 5.9:** *Structure of (R)-(+)-*pulegone

A cluster size range of $Rh_n^+$, n = 2 - 10 was optimised in order to investigate the feasibility of adsorbed species on heavier clusters, which are more likely to be chiral than smaller clusters.

Figure 5.10 shows a spectrum of cationic rhodium clusters with dosed (R)-(+)-pulegone. At first the signals for the bare metal clusters from $Rh^+$-$Rh_5^+$ are the dominant peaks compared to the adsorbate species. From $Rh_6^+$ onwards the metal-adsorbate species intensities become increasingly dominant compared to the bare metal cluster intensities. By zooming into the spectrum several oxide species can be identified (see Figure 5.8 zoom of $Rh_5^+$ and $Rh_6^+$). The most dominant species are the rhodium dioxides followed by the tetraoxide species. The formation of various rhodium oxide species in an oxidative environment is a well known phenomenon described by Yeh *et al.*[99].

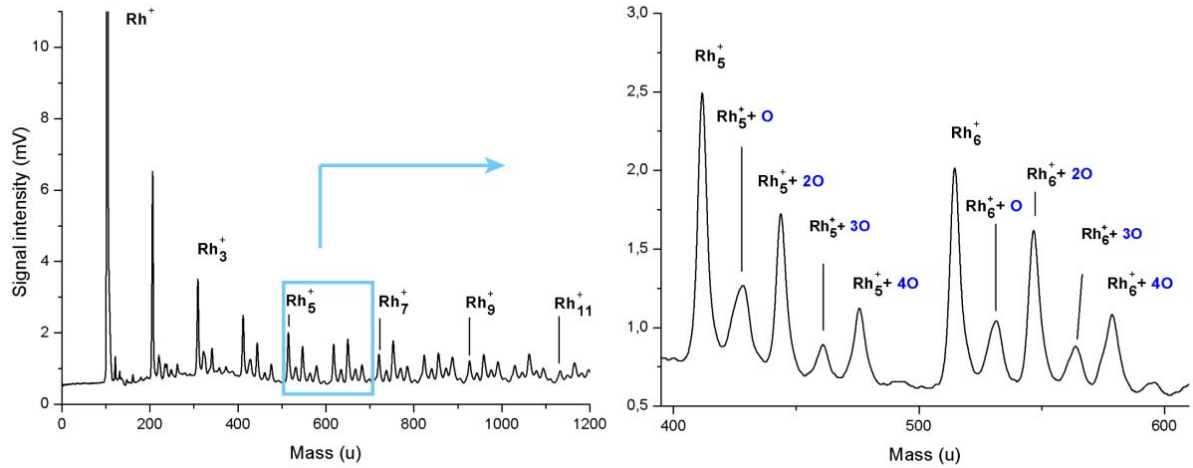


**Figure 5.10:** *Mass spectrum and zoom of cationic rhodium clusters with dosed enantiopure (R)-pulegone.*

For all considered cluster sizes the same adsorption signal pattern and no molecularly attached (R)-(+)-pulegone were observed. Only cluster-oxide species ($Rh_mO_n^+$ with n = 1-11 and m = 1-4) were found. An even/odd effect for the number of oxygen atoms is observed. As mentioned previously the dioxide and tetraoxide species showed a higher abundance than the monoxide and trioxide species. This might have been caused by the electronic and geometric properties of the rhodium oxide species. Structural studies of $Rh_6O_m^+$ (m =1-4) were performed by *Harding et al.*[55]. It was found that the oxygen atoms favoured binding on the bridging sites for most of the considered cluster sizes.

At higher cluster sizes all signal intensities decrease rapidly, but the dioxide species retain higher intensities than the bare clusters. For this experiment a high rate of cluster oxidation was observed. Fragmentation products, as were seen for 2-butanol, were not observed for experiments performed with pulegone, especially within the higher mass range.

A second piezo valve as a device to introduce organic molecules into the cluster beam is a capable and efficient tool. Several organic compounds were successfully attached to clusters of different sizes by using the piezo valve. Nevertheless, the signal intensities of the adsorbed species impeded the data analysis and concrete characterisation of the individual peaks. It is thought that the introduction of adsorbates inside the cluster source interferes with the cluster formation process and the supersonic expansion. Another drawback was caused by insertion of compounds with very high vapour pressures such as pulegone. When

the organic vapour reached the piezo housing a condensation of the vapour occurred. Interaction of the condensed vapour with the potential applied to the ceramic piezo disc caused arcing within the piezo housing and resulted in a higher amount of compound fragmentation. The piezo disc was also damaged during this event and was rendered inoperative.

## 5.2 Introduction via general valve

The implementation and utilisation of a general valve for adsorbate introduction originates from the experimental experiences made with the second piezo valve (see previous chapter). The construction was driven by the idea that adsorbate attachment would be enhanced by dosing outside of the cluster source, as the bare clusters undergo cooling during the gas expansion and therefore subsequently have less internal energy. Less fragmentation was expected by adding the organic molecule to the clusters outside of the cluster source. The pulsed valve was installed at the bottom side of the source chamber and therefore the general valve pulse was directed perpendicular to the cluster beam expansion.

### 5.2.1 Tantalum clusters plus aliphatic alcohols

The binding behaviour of tantalum clusters was investigated using four different aliphatic alcohols: methanol, ethanol, 1-propanol and 2-propanol (see Table 5.1 for the respective molecular properties).

**Table 5.1:** *List of utilised aliphatic alcohols and their properties*

| Alcohol | Formula | Molecular mass (u) | Vapour pressure at RT (mbar) |
|---|---|---|---|
| methanol | $CH_3OH$ | 32 | 132[100] |
| ethanol | $CH_3CH_2OH$ | 46 | 59[100] |
| 1-propanol | $CH_2OHCH_2CH_3$ | 60 | 19[100] |
| 2-propanol | $CH_3CHOHCH_3$ | 60 | 58[100] |

For the results presented in this chapter, several millilitres of alcohol were filled into the bubbler housing and subsequently connected to the helium gas line and the general valve gas line (see Chapter 3.1). The presented spectrum in Figure 5.11 shows a cationic tantalum cluster distribution of $Ta_n^+$, n = 4 - 7 as clusters in this size range showed high intensities and could be resolved well. All considered cluster sizes showed similar adsorbed species. No molecularly attached methanol was observed on any cluster size. One of the dominant adsorbed fragments for $Ta_n^+$, n = 4 - 6 is an OH-group which most likely originated from the hydroxyl group of methanol.

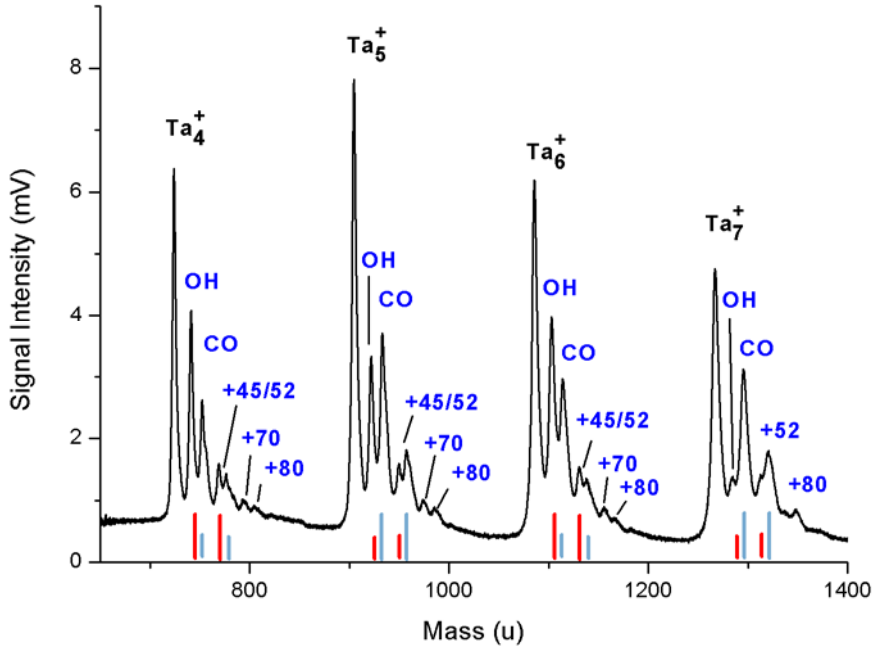


**Figure 5.11:** *Mass spectrum of $Ta_n^+$ clusters (n=4-7) with injected methanol (32 u). An even/odd effect was observed for the intensity ratios of + OH/CO and + 45/52 highlighted by red and blue bars.*

Carbon monoxide was the second most dominant adsorbate signal and arose due to the complete dehydrogenation of an adsorbed methanol. Catalytic dehydrogenation of alcohols by tantalum containing catalysts was described by Chihara *et al.*[101] and was already observed for niobium and rhodium clusters towards ethanol and 2-butanol in this work. The most interesting feature was observed for the ratio of both species, which showed an even/odd effect with cluster size. Clusters with an even number of tantalum atoms showed a larger amount of adsorbed OH than CO. The ratio was reversed for clusters with odd numbers of atoms. The coordination of OH occurred via the oxygen as described previously in Chapter 2.5.

The mass peak at + 45 u could correspond to OH with co-adsorbed CO according to the appearance of the individual signals for OH and CO. An adsorbed mass of + 52 u could correspond to CO plus two co-adsorbed carbon atoms, which would indicate a C-O bond cleavage. The ratio of both signals changes analogously to the OH/CO ratio. These results could indicate a size dependent reactivity of cationic tantalum clusters with methanol. Two possible mechanisms could have led to these observations. In one mechanism C-O bond cleavage is favoured, which leads to an enhancement of OH formation compared to CO. The other mechanism favoured the complete dehydrogenation of methanol and therefore, a C-H bond cleavage. The favoured mechanism was seen to depend on cluster size. Clusters with an even number of atoms showed favourable OH adsorption while "odd" clusters favoured CO adsorption. Mass + 70 u and + 80 u could be assigned to an adsorption of two methanol molecules which have been dehydrogenated or reacted in other ways.

The spectrum of cationic tantalum clusters with introduced **ethanol** (see Figure 5.12) illustrated similar fragmentation patterns as the spectrum for methanol for the same cluster size range ($Ta_n^+$, n = 4-6).

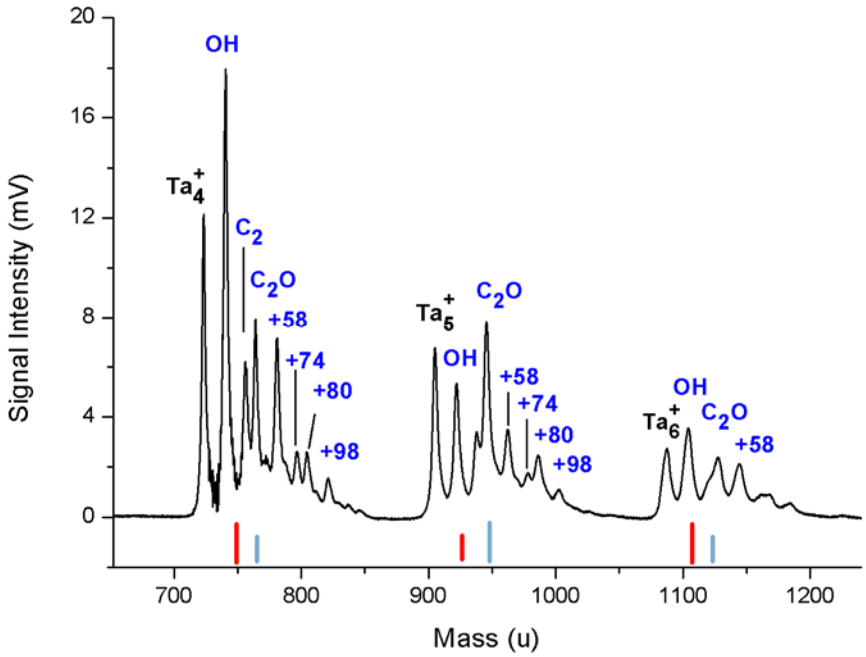


**Figure 5.12:** *Mass spectrum of $Ta_n^+$ clusters (n=4-6) with injected ethanol (46 u). An even/odd effect was observed for the intensity ratios of OH/$C_2O$ and is highlighted by red and blue bars.*

No ethanol was observed to molecularly adsorb on the clusters. The OH signal for $Ta_4^+$ is the most dominant adsorbed species in the spectrum. The signal for + 40 u was interpreted as a complete dehydrogenation of ethanol and + 58 u was linked to completely dehydrogenated ethanol plus co-adsorbed OH ($C_2O$ + OH). Discrimination between OH and $H_2O$ was not feasible with the available mass resolution. Although, due to the strong abundance of OH in the spectrum for all considered cluster sizes, a co-adsorbed OH was assumed to be more likely. Two adsorbed carbon atoms were only observed for the cationic tetramer and pentamer.

The intensity ratios of OH/$C_2O$ showed the same even/odd effect as in the methanol spectrum. Two mechanistic pathways for the reaction of cationic tantalum clusters with ethanol depending on the cluster size, were assigned. Even/odd effects for larger masses were not as significantly visible. The ratio of $C_2O$/+ 58 u remained almost the same for $Ta_4^+$ and $Ta_6^+$ but for $Ta_5^+$ the intensity of the peak assigned to + 58 u showed a considerable reduction compared to $C_2O$. Attached species with masses which are higher than the mass of ethanol can be assigned to multiple adsorptions of ethanol molecules which did undergo hydrogenation or C-O bond cleavage.

In Figure 5.13 the adsorbed species for the monomer, dimer and trimer are shown. Molecular ethanol was also not observed on any of the cationic tantalum species. The adsorbate signals for $Ta^+$ differed significantly from all other investigated cluster sizes. Adsorbed OH groups were still observed in this lower size regime, but signal groups of + 54 u, + 60 u, + 68 u and + 76 u only appeared on the monomer. A mass of + 34 u was only observed in the lower size regime and could correspond to two adsorbed OH groups. The intensity of this species decreased strongly for the dimer and trimer. For the monomer it was the most abundant species. Additional masses for species adsorbed on the monomer could correspond to carbon-hydrogen species as a fully dehydrogenated ethanol (+ 40 u) was not observed. This is a unique observation as all other cluster sizes considered showed fully dehydrogenated species. This observation can be assigned to a change in reactivity with ethanol depending on the cluster size and therefore probably on the geometric and/or electronic properties of the tantalum cations. The monomer appeared to be less reactive towards ethanol, especially for the dehydrogenation reaction.

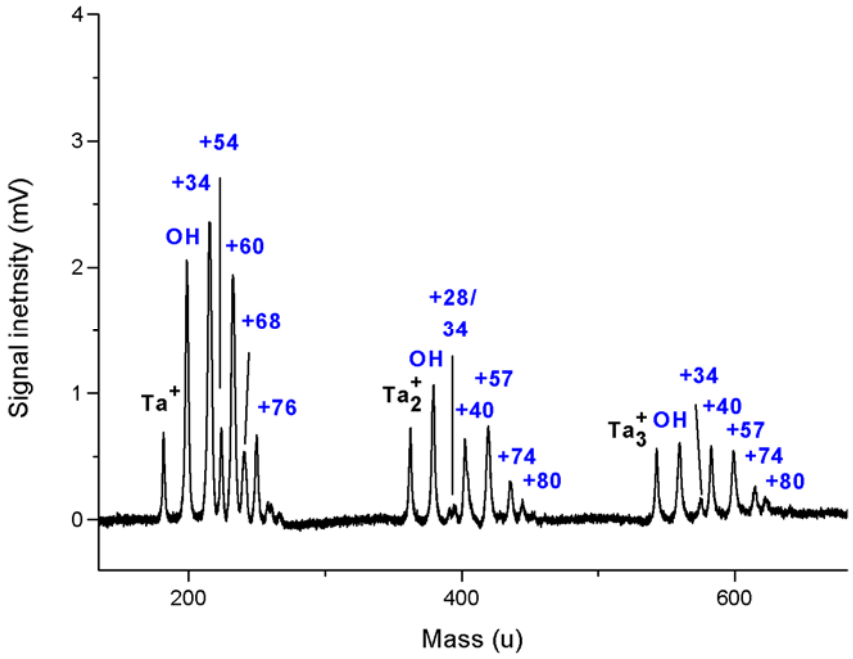


**Figure 5.13:** *Mass spectrum of $Ta_n^+$ clusters (n=1-3) with dosed ethanol (46 u).*

The intensity ratio of OH/$C_2O$ did not show a strong even/odd effect for the tantalum dimer and trimer as was seen for larger clusters. Still, for $Ta_2^+$ the signal corresponding to OH was considerably larger in intensity than $C_2O$. For $Ta_3^+$ the ratio of both species was approximately equal, but could not be investigated further due to the generally low intensities for this cluster size. The adsorbates corresponding to an additional mass higher than the mass of ethanol can be assigned to multiple adsorptions of ethanol fragments as for larger clusters.

In the next experiment **1-propanol** was investigated. Analogous to methanol and ethanol no individual molecular absorbed 1-propanol was observed in the spectrum (Figure 5.14). Complete dehydrogenation of 1-propanol occurred similar to what was observed for methanol and ethanol on every considered cluster size. The OH group was the dominant adsorbed species for $Ta_n^+$, n = 4, 5, 6, and 8. Only for $Ta_7^+$ and $Ta_9^+$ was the signal intensity for this peak seen to decrease considerably. An adsorbed dioxide species was observed for $Ta_4^+$, $Ta_5^+$, $Ta_6^+$ and $Ta_8^+$, but not for $Ta_{7,9}^+$. This indicates that oxygen contamination was present in this experiment.

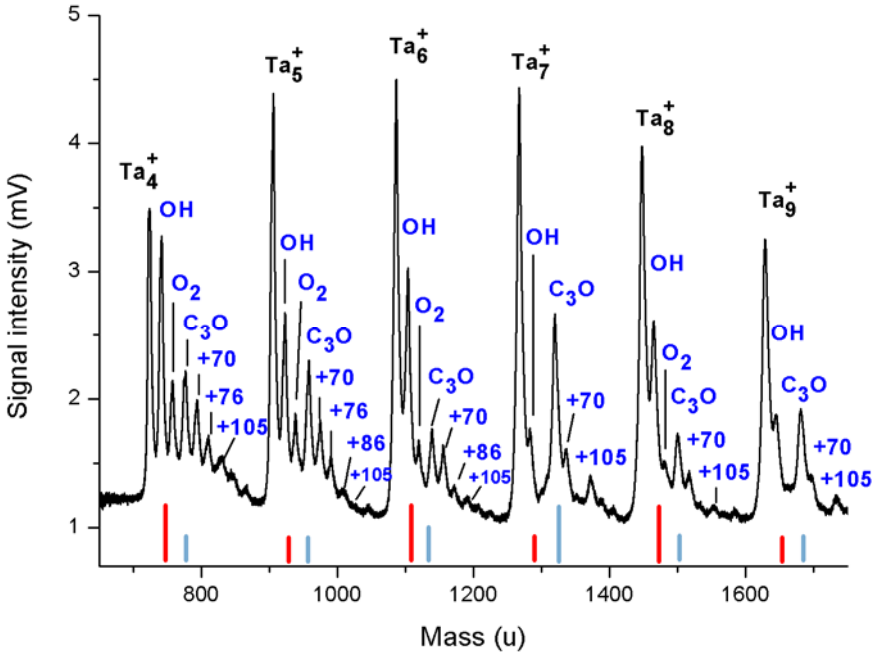


**Figure 5.14:** *Mass spectrum of $Ta_4^+$-$Ta_9^+$ with introduced 1-propanol (60 u). An even/odd effect was observed for the intensity ratios of OH/$C_3O$ u and is highlighted by red and blue bars.*

Also, the peak groups belonging to $Ta_{7,9}^+$ showed a different shape than the other investigated cluster sizes. No signal intensity was observed between the peaks of the adsorbed OH group and the adsorbed $C_3O$ group. The peak of the adsorbed $C_3O$ group also appeared to be broader than for the other clusters. Previous studies did not offer an explanation for a different reactivity of $Ta_7^+$ and $Ta_9^+$ with any organic compound, even though $Ta_7^+$ is seen as a magic number cluster.[86] As well resolved spectra of larger clusters were not feasible in this experiment, a clear size effect for those two cluster sizes cannot be clarified. Otherwise, an identical even/odd effect as for methanol and ethanol was observed for the ratio of OH/$C_3O$ on the cationic tantalum clusters towards 1-propanol. A feature which distinguished the tantalum-propanol spectrum from the two other alcohols was the appearance of a signal at 105 u. This signal group could be assigned approximately to two dehydrogenated 1-propanol molecules. Unfortunately, the lower size regime ($Ta_{1\text{-}3}^+$) was not visible for these particular experimental settings, so a comparison between the reactions of both alcohols with the monomer was not possible. Though it is assumed that the similarities observed in the cluster regime would carry through to the smaller tantalum cations.

To investigate if the structure of the adsorbate and therefore the position of the functional group influenced resulting adsorbate populations, **2-propanol** was utilised. In comparison to 1-propanol where the hydroxyl group is located on a terminal carbon, in 2-propanol the OH group is bound to the central carbon. The cluster sizes of the following spectrum extend from a lower to a higher size regime ($Ta_n^+$, n = 1- 8).

The spectrum (see Figure 5.15) showed less fragmentation products than the spectrum for 1-propanol. Again, no signal at + 60 u (2-propanol) appeared on the clusters. The intensities for $Ta_2^+$ and $Ta_3^+$ were similar to the respective peaks in the spectrum of ethanol showed previously. The hydroxyl group can be observed on every cluster size as well as a signal at + 54 u, which was assigned to partially dehydrogenated 2-propanol. In the spectrum of 1-propanol the mass of the dehydrogenated species appeared at + 52 u which indicated a full degree of dehydrogenation. 2-propanol seemed to be more stable towards dehydrogenation than 1-propanol. A different structure of the isomer could be the reason for the change in reactivity.

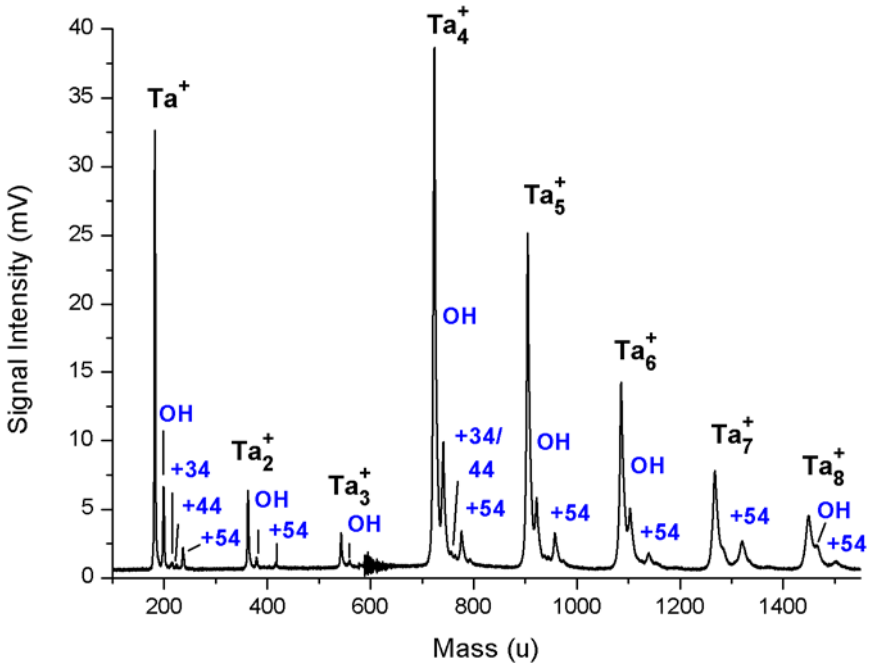


**Figure 5.15:** *Mass spectrum of $Ta^+$-$Ta_8^+$ with dosed 2-propanol (60 u)*

As the adsorbate signals had very small intensities an even/odd effect as recognised for all other alcohols was not observed for 2-propanol in this experiment. Though, ongoing

experiments which offer higher signal intensities predict the same even/odd effect observed for methanol, ethanol and 1-propanol.

The systematic investigation of the adsorption interactions between cationic tantalum clusters and aliphatic alcohols showed a distinct even/odd effect for the signal intensities corresponding to OH and the fully dehydrogenated alcohol $C_xO$. For a clarification of this effect, a rough estimation of the $C_xO$/OH ratios, based on the signal intensity heights, were plotted against the cluster size. Due to fluctuations of the cluster source conditions during the course of an experiment, an error of about 10 % for the calculated ratios was assumed. For the plot of 2-propanol, data were used, that were recorded after the experimental work for this thesis was completed. The resulted plots are shown in Figure 5.16.

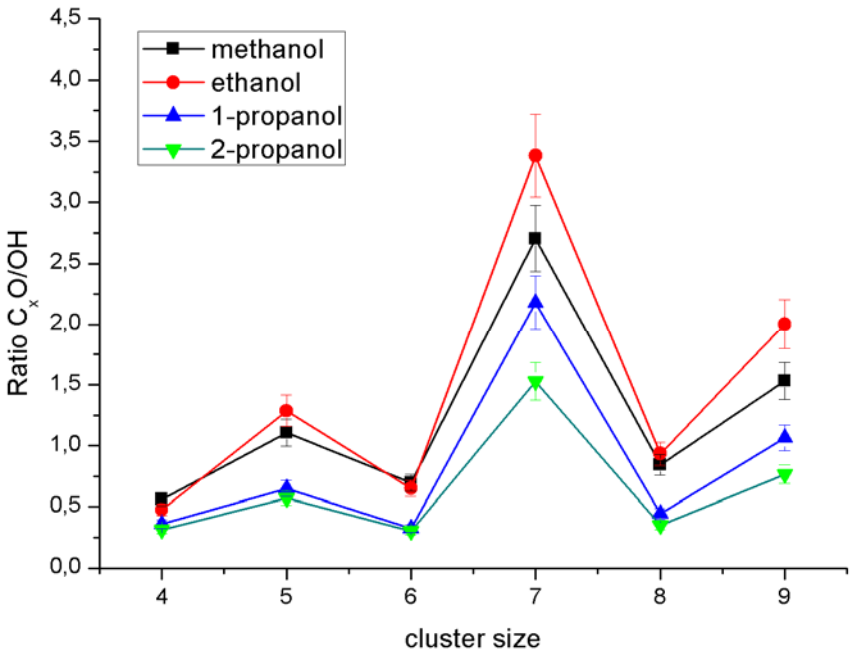


**Figure 5.16:** E*ven/odd effect for the ratio of $C_xO$/OH for all utilised aliphatic alcohols. The ratio is plotted against the number of atoms per cluster.*

A change of the ratio depending on the alcohol can be assigned to the change of the cluster source conditions for the individual experiments. The same even/odd effect depending on the cluster size, was observed for all utilised aliphatic alcohols. Two reaction pathways can be assigned by these results. One pathway prefers C-H bond cleavage which leads to complete dehydrogenation of the alcohol and the other favours C-O bond cleavage which

leads to a signal assigned to an OH group bound to the metal cations. Clusters with an even number of atoms show a lower ratio and therefore appear to preferentially follow the C-O bond breaking pathway. Clusters with an odd number of atoms show an increased ratio, which implies that the dehydrogenation reaction is favoured.

The highest amount of dehydrogenation relative to bare metal cluster intensity was observed for every alcohol on $Ta_7^+$. $Ta_7^+$ is known from literature[86] as a magic number cluster. Fielicke *et al.* [40] predicted the ground state of $Ta_7^+$ as a highly symmetric pentagonal bipyramid with $D_{5h}$ symmetry.

The difference in “even” and “odd” clusters could be assigned to the difference in electronic structure.

# 6. Laser spectroscopy methods

Discrimination and separation of chiral metal clusters by laser spectroscopy has been a focus of intense research in the last several years. A highly discrete method of analysis would open new strategies for a more precise control of synthesis and application of chiral catalysts in industry.

As described in Chapter 1.3, several different spectroscopic methods are suitable to fulfil the purpose of recognition of chiral compounds. A precise and sufficient discrimination of chiral metal–adsorbate complexes, as presented in the previous chapter, is still missing and has not yet been established. In this chapter the first results for the photoionisation and photodepletion of metal clusters using the current experimental setup are presented.

## 6.1 Photoionisation of tantalum at 355 nm

The specific suitability of the various laser spectroscopy techniques intended to be used for the identification of metal cluster-adsorbate diastereomers, have not yet been tested on such species. Therefore, photoionisation experiments were performed as a first test of the experimental setup.

### 6.1.1 Neutral tantalum clusters

The first non-resonant ionisation experiments were carried out for neutral tantalum clusters. The third harmonic (355 nm) of a 33 Hz triggered Nd:YAG laser with 30 mJ/pulse was guided by several high reflecting mirrors and periscope assemblies (see Chapter 3.6) into the ion source region of the TOF-MS (between the repeller and extractor electrodes) and irradiated the neutral cluster beam perpendicular to the beam direction. Charged clusters, which were formed in the cluster source, were deflected by applying a voltage of 70 V onto the ion filter electrode (see Chapter 3.3) in front of the expansion nozzle. This procedure enabled only the neutral clusters to pass through the ion filter. Subsequent ion

optics could not be used to guide the neutrals into the TOF-MS due to the missing charge. The 355 nm laser was set to fire approximately 500 ns after the TOF-MS electrodes were pulsed. In Figure 6.1 the two spectra of the original cationic clusters and the photoionised species were overlayed.

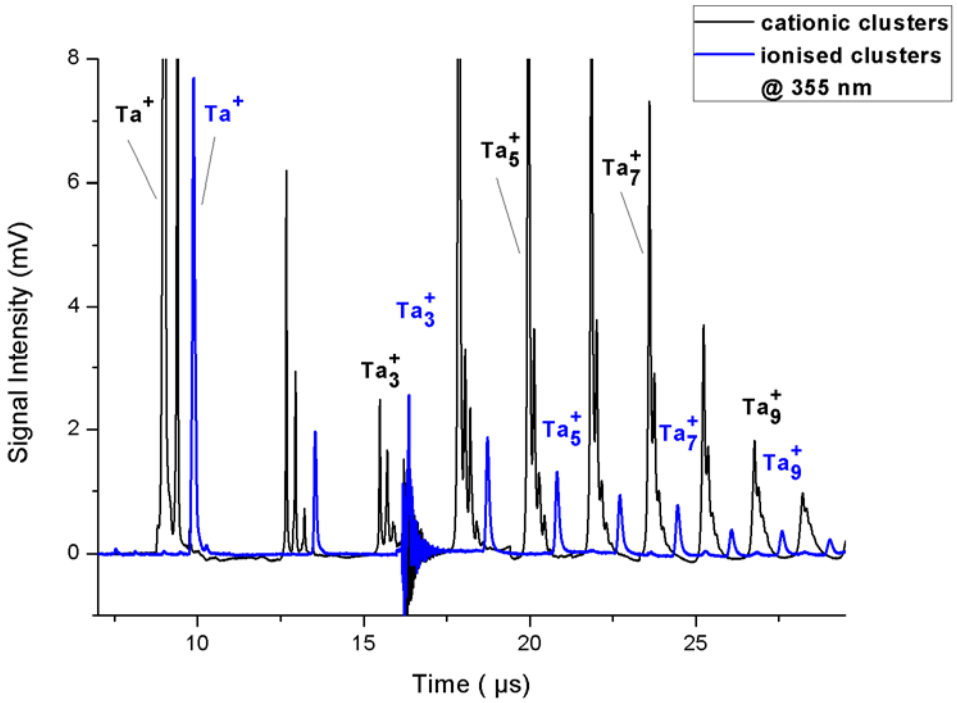


**Figure 6.1:** *Overlayed spectra of the original cationic tantalum clusters (n = 1-10, black) and the photoionised neutral species at 355 nm with 30 mJ/pulse (n = 1-10, blue). The ionised neutrals were shifted in time due to the delay time of the 33 Hz trigger.*

In comparison to the original cationic clusters the ionised neutral clusters showed significantly lower signal intensities, with the exception of $Ta_3^+$. The mass resolution for the cationic clusters was about 100 while the resolution for the ionised neutrals was measured to be approximately 60. This difference can be observed in the broadenss of the peaks corresponding to the ionised clusters. This reduction of mass resolution was seen for every ionisation experiment performed in this work. By reducing the power of the laser a narrowing of the peaks was expected, due to the decrease in the number of ions produced and therefore, the influence of the space-charge effects, but was not observed. The broadness of the peaks remained the same independent of the laser power.

The 355 nm laser beam (maximum diameter 2mm) was clipped by an iris. The signal intensities of the ionised species increased as the iris aperture was opened. At maximum

beam diameter the signals of all clusters were enhanced to the maximum values for a constant laser power. In the spectrum of the nascent cations, different oxide species were observed and were assigned to small amounts of contaminants in the vacuum system. Between $Ta_3^+$ and $Ta_4^+$ noise coming from the TOF-MS trigger signal was observed. The ionised $Ta_3^+$ lies on top of the noise. The spectrum of the ionised neutrals showed a similar cluster size distribution to that of the nascent cations, with $Ta^+$ the most abundant species (8 mV). Otherwise the signal intensity ratios of the dimer and trimer compared to $Ta_4^+$ differ significantly from the nascent cluster cations. As described previously in Chapter 4.2, the nascent $Ta_2^+$ and $Ta_3^+$ were observed with a much lower abundance than the next larger clusters. It was believed that these two species preferably undergo neutralisation reactions or dissociation processes in the cluster source. The spectrum presented above could provide the first evidence for this hypothesis, as the dimer and trimer show a similar or even higher (for the trimer) signal intensity when produced through laser ionisation. Otherwise, fragmentation of larger clusters as a consequence of the ionisation process could also lead to an enhanced intensity for n = 2 and 3. The ionisation potentials of neutral tantalum clusters were measured and investigated by Collings *et al.*[42] with 193 nm, 207.5 nm and 275 nm laser wavelengths produced by a frequency doubled excimer pumped dye laser. The ionisation potentials that are presented in Table 6.1 showed a non-monotonic pattern, especially for clusters with less than 20 atoms. This suggests that clusters in this size regime show distinct geometrical and electronic properties.

**Table 6.1:** List of *ionisation potential values of $Ta_n$ clusters depending on the number of atoms.*

| Number of atoms | Ionisation potentials[42]/ eV | Corresponding wavelength/ nm |
|---|---|---|
| 1 | 7.89 | 157.14 |
| 2 | 5.98-6.42 | 193.12-207.33 |
| 3 | 5.58 | 222.19 |
| 4 | 5.78 | 214.51 |
| 5 | 5.18 | 239.35 |
| 6 | 5.08 | 244.06 |
| 7 | 5.17 | 239.81 |
| 8 | 5.22 | 237.51 |

| | | |
|---|---|---|
| 9 | 5.06 | 245.02 |
| 10 | 5.09 | 243.58 |

As is visible in the Table 6.1, a wavelength of 355 nm (3.49 eV) is not sufficient to ionise neutral tantalum clusters with a single photon. All observed cationic species (in blue) in Figure 6.1 except $Ta^+$ were produced by two photon processes. Due to the large ionisation potential, $Ta^+$ originates from a three photon process. The probability of a three photon ionisation process is strongly reduced compared to a single photon or two photon processes. The high abundance of the tantalum monomer created by a three photon process could indicate that a large amount of neutral atoms were produced in the cluster source. Another explanation could be given by different possible dissociation pathways of larger neutral and cationic clusters that might fragment into atomic cations and other species (i.e. $Ta_2^+$ and $Ta_3^+$).

Spectra (see Figure 6.2) were recorded at different laser pulse energies. By increasing the laser pulse energy up to 80.8 mJ the intensity of the ionised cluster species was considerably enhanced. Further increasing the energy input up to 99 mJ did not cause further signal enhancement for tantalum species larger than the monomer. Instead a slight reduction in the intensity of these cluster sizes was found. Cluster sizes of $Ta_n^+$, n = 8 and 9 started to disappear completely when the laser pulse energy was increased further.

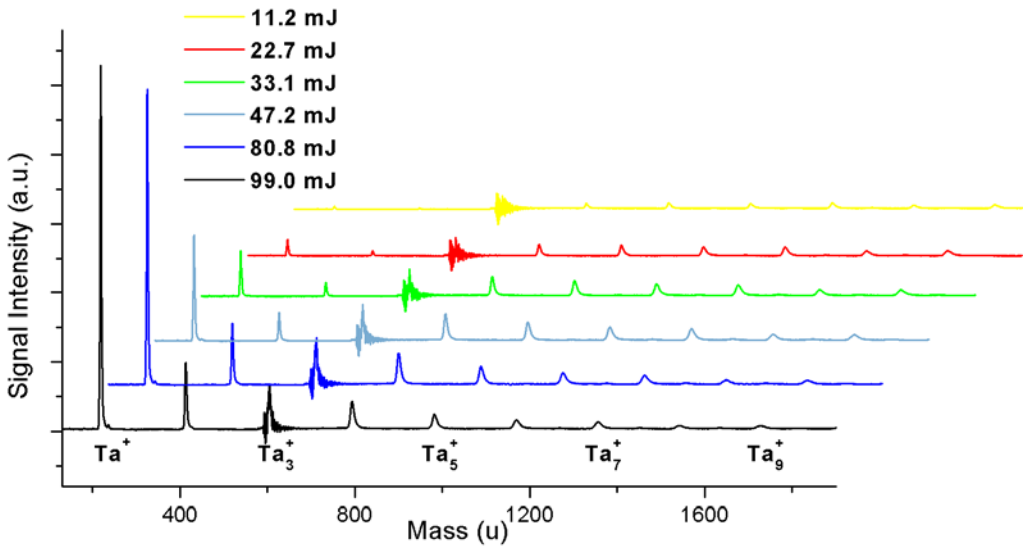


**Figure 6.2:** *Ionisation spectra of neutral tantalum clusters (n = 1 - 9) recorded at different laser pulse energies.*

The integrated peak areas for each cluster size are plotted against the laser pulse energy in a double logarithmic plot (see Figure 6.3).

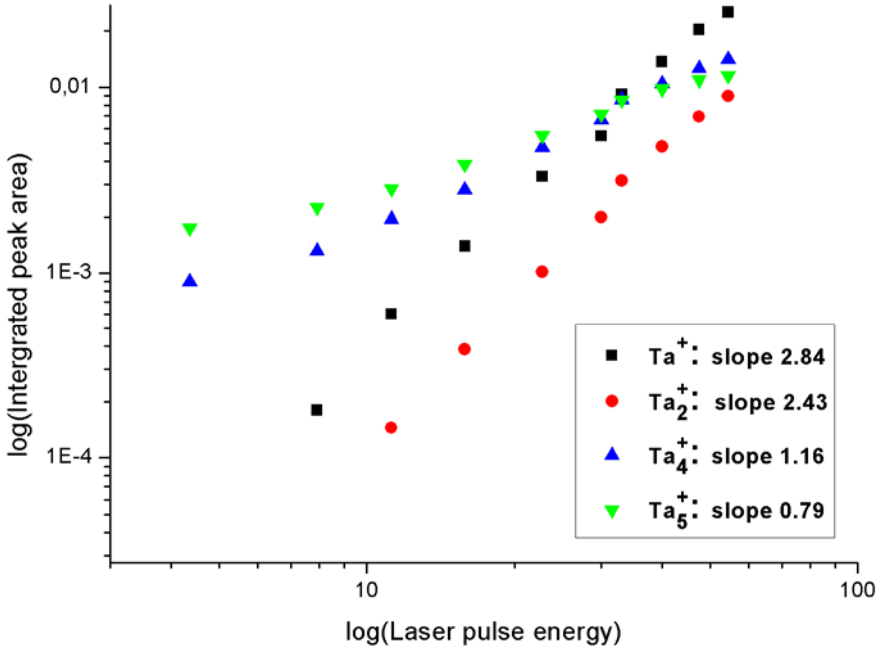


**Figure 6.3:** *Integrated peak area of $Ta_n^+$, n = 1, 2, 4, 5 in a double logarithmic plot against increasing laser pulse energy.*

By fitting straight lines to the data points in Figure 6.3 the resulting slope of the equation is proportional to the order of the ionisation process. For $Ta^+$ a slope of approximately 3 was found which indicates a 3 photon ionisation process. This is in excellent agreement with the expectations that at a laser wavelength of 355 nm, which offers a photon energy of 3.49 eV, ionises the neutral tantalum monomer via a three photon process due to the IP of 7.89 eV. For the dimer a two photon process was expected and is found to have a slope of 2.43 from the linear regression. $Ta_3^+$ was not included in this graph as the corresponding peak was overlayed by the trigger signal of the switching TOF-MS electrodes. Due to the IPs of $Ta_4$ and $Ta_5$ two photons of 3.49 eV are required to ionise these two species and all of the remaining larger cluster species that are seen in Figure 6.2. The slopes, found for $Ta_4$ and $Ta_5$ (1.16 eV and 0.79 eV, respectively), indicate a one photon process. These misleading results are caused by the shape of the two corresponding plots. For both species the plot first increases linearly and then forms a slight plateau. This change in the plot trend depending on the laser pulse energy is an indication for photodissociation and photofragmentation of the cluster

species and also saturation effects in the experiment. By further increasing the laser power no enhancement of the ionisation yield is achieved. Instead, due to the higher energy input, fragmentation of the clusters occurs. Therefore, a clear observation of the two photon process for $Ta_4$ and $Ta_5$ in the plotted data is not feasible.

These non-resonant ionisation experiments were the first laser spectroscopic results obtained with the experimental setup. Another goal, which is necessary to characterise metal cluster-adsorbate complexes by REMPI spectroscopy, is to investigate the ionisation behaviour of such complexes. As a first system cationic tantalum clusters and 2-propanol was chosen to be studied.

### 6.1.2 Tantalum + 2-propanol

The interaction between organic compounds and metal clusters can be influenced by the charge state of the cluster. Kaldor et *al.*[102] presented reaction kinetics studies of neutral and ionic niobium clusters with $D_2$. It was found that cations and anions did not differ significantly in their reaction rates for the majority of the clusters investigated. The maximum uptake of $D_2$ by niobium clusters was found to be independent of the charge state, but varied strongly with cluster size. Otherwise, the reactivity of ions was generally within a factor of 2.5 higher than the corresponding neutrals.

1-propanol was used to investigate the adsorption behaviour of tantalum clusters depending on the cluster charge. A spectrum (see Figure 6.4) for nascent cationic tantalum clusters was recorded in the cluster size range of n = 1-5 with 1-propanol introduced via the general valve. Subsequently, the ion filter in front of the nozzle was set to 70 V to deflect all charged species coming from the cluster source. The general valve remained in operation and the 355 nm laser beam was directed into the TOF between the repeller and extractor electrodes and irradiated the neutral cluster beam. A second spectrum was recorded and is also presented in Figure 6.4. The spectrum originating from the nascent cationic clusters showed strong fragmentation patterns similar to those presented previously in Chapter 5.2. The monomer is the dominant species in the spectrum. The signal intensities dropped

rapidly with increasing cluster size. Therefore, a clear analysis of the adsorbate signals on cationic tantalum species larger than the monomer could not be performed. The signal intensities in the laser ionised spectrum were considerably larger, especially for the monomer, dimer and trimer. In comparison to the minimal fragmentation patterns of the neutral clusters, the cationic species showed a stronger binding affinity towards different fragment species. The OH peak on the neutral monomer was found to be significantly smaller than for the cationic monomer.

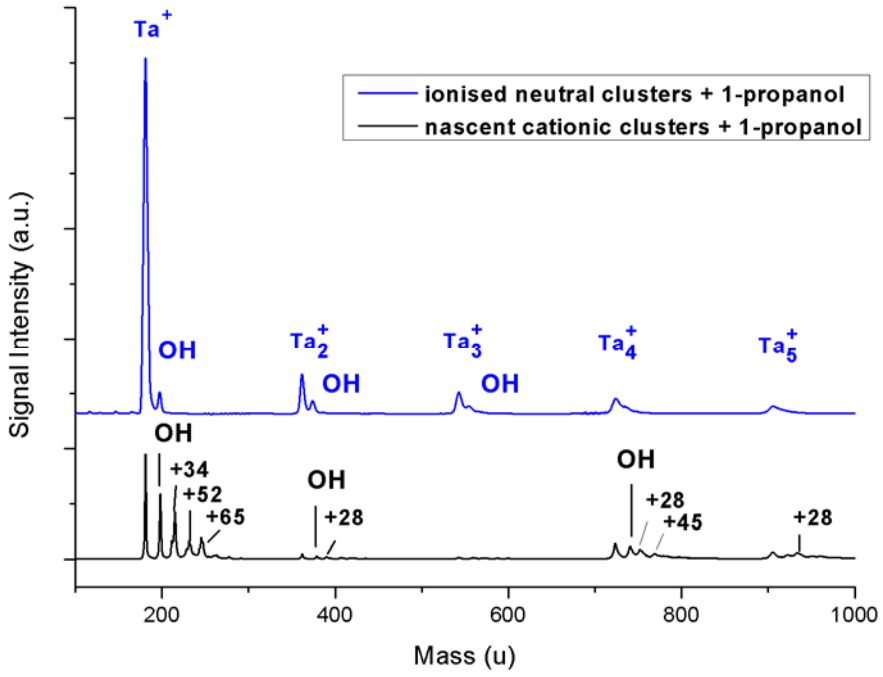


**Figure 6.4:** *Mass spectra of nascent cationic tantalum clusters (n= 1-5) and at 355 nm ionised tantalum clusters with dosed 1-propanol.*

Besides the adsorption of OH on nascent cationic clusters, a fragment with a mass of + 34 u was observed on the cluster, which was assigned to the adsorption of two OH groups. An adsorbate mass of + 52 u can be linked to a fully dehydrogenated propanol, as described previously in Chapter 5.2. Similar to the results of alcohol adsorption on tantalum clusters presented in Chapter 5.2, no single molecularly attached 1-propanol was observed on the cationic species. The appearance of an adsorbate of mass + 28 u that was assigned to CO, was found on all nascent cationic clusters in the investigated mass range, except for the monomer. This might be caused by differences in electronic and geometric structures of the different cluster sizes. The formation pathway of the observed tantalum-hydroxyl complex is

not clear. One pathway could start from the neutral tantalum species onto which 2-propanol adsorbs. This complex is ionised by the 355 nm laser beam. Due to this ionisation C-O bond cleavage in 2-propanol could take place and OH is the only species left adsorbed on the tantalum species. Another probable pathway could also start from the neutral tantalum species with adsorbed 2-propanol and subsequently is in a first step ionised with 355 nm, which leads to a cationic tantalum-adsorbate species. A second photo adsorption step could then lead to the fragmentation of 2-propanol.

## 6.2 Photodepletion of rhodium anions at 355 nm

Photodepletion experiments on rhodium clusters were carried out in the anion mode of the experiment. The experimental settings were optimised for a cluster size range of $Rh_n^-$, n = 3-14. A reference spectrum of the nascent anionic rhodium clusters was recorded (see Figure 6.5, black line).

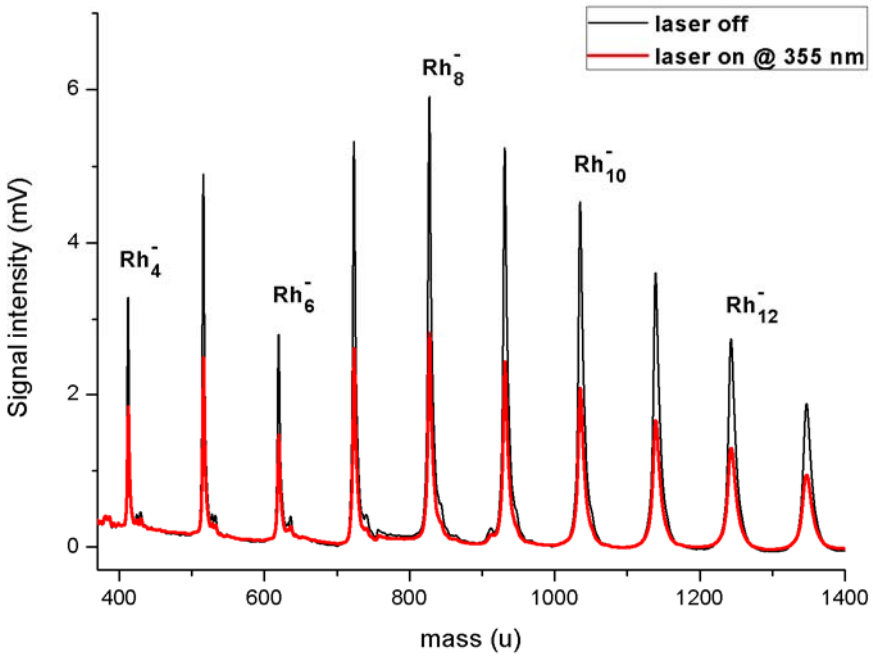


**Figure 6.5:** *Mass spectrum of anionic rhodium clusters (n = 3-13, black line) with superposed depletion spectra (red line) @ 355 nm.*

The most intense signal corresponded to $Rh_8^-$ with an intensity of 6 mV. Several oxide species and other contaminations were found on clusters up to $Rh_6^-$. The third harmonic (355 nm) of a Nd:YAG laser irradiated the anion beam perpendicular to the expansion direction of the beam and was positioned between nozzle and skimmer in the cluster source vacuum chamber. The laser beam excited anionic rhodium clusters and led to the photodetachment of electrons. Therefore, as expected, the signal intensities of the anionic clusters were seen to decrease. Depletion of the cluster signals was maximised by adjusting the timing and the position of the 355 nm laser beam. The individual signals were integrated for the depletion spectrum and compared with those for the nascent anionic species. A signal depletion of about 33 % for $Rh_4^-$ and about 48 % for $Rh_{13}^-$ were found and are shown along with data for the other cluster sizes in Figure 6.6.

During the following experiments the output of a dye laser operating with Coumarin 307 was used. The pulse energy was held at a constant value of 6.6 mJ while the wavelength was scanned from 485 nm to 520 nm in 5 nm steps. A selection of the resulting depletion values, including the ones measured for 355 nm, are presented in Figure 6.6

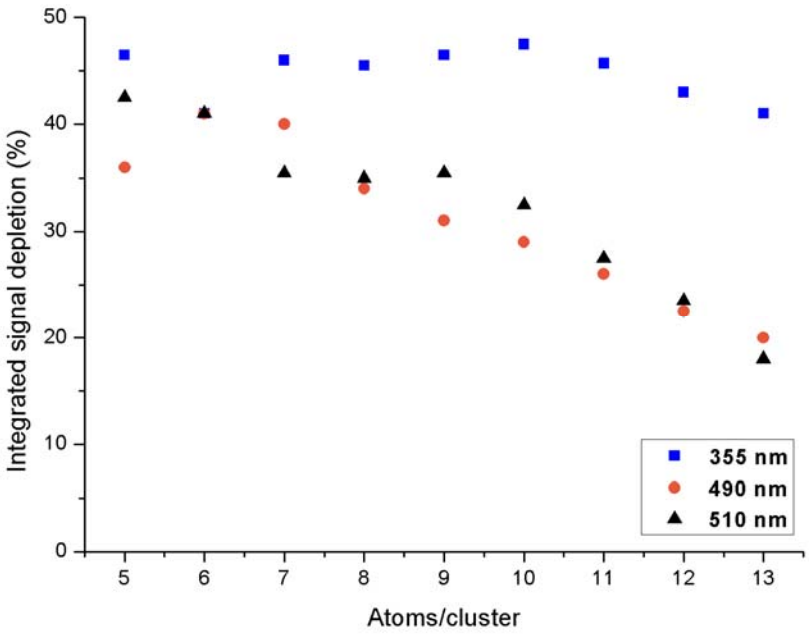


**Figure 6.6:** *Comparison of the signal depletion of anionic rhodium clusters through excitation with photodepletion wavelength of 355 nm, 490 nm and 510 nm.*

It was observed that the amount of signal depletion for 355 nm did behave quite consistently with cluster size. The depletion amount varied slightly by less than 10 %. For 490 nm the decrease in the depletion amount from $Rh_6^-$ on shows a constant trend. A similar trend is found for depletion at 510 nm. There the amount of depletion reaches a short plateau for $Rh_7^-$ - $Rh_9^-$ and then follows a linear decrease, as seen for 490 nm.

The vertical and adiabatic detachment energies have been shown (see Chapter 2.4) to increase with the size of the anionic rhodium clusters.[30] Therefore, a considerable decrease of the signal depletion was expected above a certain cluster size. For example, the vertical detachment energy of $Rh_9^-$ was reported as 2.4 eV.[30] Photons of 520 nm laser wavelength have only 2.38 eV. If depletion occurred at this wavelength, then a two photon process must have taken place. Though, the reduced probability of such a process should result in considerably less signal depletion compared to a one photon process. To reduce the probability of a two photon process the laser intensity was decreased. However, such a sharp reduction of signal depletion for heavier clusters did not occur, but a general trend in less depletion for larger clusters was observed for 490 nm and 510 nm.

In further depletion experiments the signal depletion was found to be not as constant. Fluctuations in the cluster formation process might account for this. Due to these fluctuations spectra were averaged over 1000 shots. This caused a significant time delay between the recording of a reference spectrum and a depletion spectrum. Due to this delay a shift in the optimised cluster size distribution might have occurred. As a consequence “pseudo depletion” was observed, which meant that the signal intensities decreased due to fluctuations in the amount of the nascent tantalum anions produced in the source, rather than from photodepletion processes in the laser beam. The observed “pseudo-depletion” was of the same order of magnitude (20 %) as the actual depletion caused by laser excitation. To overcome this issue a different method of data acquisition needs to be implemented. As described previously in Chapter 3.6, the laser used for the depletion experiments was triggered at 33 Hz, whereas the ablation laser was triggered at 100 Hz. Thus, a reference spectrum could potentially be recorded every first or second laser shot, corresponding to the emission of the 33 Hz spectroscopy laser. Long term fluctuations of the signal intensity could then be avoided and the actual signal depletion could be obtained. Significant modification of the oscilloscope functions would be demanded for this purpose and as such this was not feasible during this work.

The experiments did show the possibility of performing spectroscopy on the nascent anions generated within the metal cluster source and could be used to improve the functionality of the spectroscopic setup.

# 7. Conclusion and Outlook

During this work an experimental setup was built, which enables the investigation of metal cluster-complexes in the gas phase using time-of-flight mass spectrometry laser spectroscopy. A high frequency (100 Hz) laser vapourisation cluster source, based on the design used by Heiz *et al.* ,[63] was built and utilised to produce **cationic, anionic and neutral metal clusters** from different metal targets (niobium, tantalum, rhodium). Size regimes from single atoms, dimers and trimers up to over 80 atoms per cluster in the case of cationic rhodium clusters (see Chapter 4.1.3) were obtained. The cluster source settings were optimised to achieve signal intensities of several 100 mV (corresponds to ~ 50.000 ions) for cationic tantalum clusters (see Chapter 4.1.2). The temporal distribution of cationic niobium clusters were measured by time-of-flight experiments and with an in-house build capacitive decoupled device. It was found by the TOF measurements that cationic niobium clusters showed a time spread of 1.2 ms, and for anionic clusters the time spread was found to be significantly shorter (about 500 µs).

In order to produce **metal cluster-adsorbate complexes** a unique modification of the cluster source was realised. A second pulsed piezoelectric valve was added to the cluster source to introduce organic compounds to the cluster beam inside the expansion channel (see Chapter 3.1). By operating and synchronising the second piezo valve with the source and laser settings (see Chapter 3.7) adsorption spectra were obtained and recorded for several organic compounds (see Chapter 5.1). Successful intact molecular adsorption was observed for ethanol on the cationic niobium monomer and dimer and 2-butanol on the cationic rhodium monomer, dimer and trimer. By increasing the pulse width of the second piezo valve all nascent ion signals started to disappear. This phenomenon was observed for many different adsorbate experiments and can be assigned to the interference of the cluster formation process in the cluster source caused by the introduction of an adsorbate into the expansion channel. Adsorption experiments with rhodium clusters were performed as an early transition (clusters with 3-4 atoms) from 2D to 3D structures can lead to the potential for intrinsic chirality in small clusters. Cationic rhodium clusters with dosed enantiopure

organic compounds ((R)-(+)-limonene and (R)-(+)-pulegone) showed no molecular attachment of the compound on the cluster.

The control of the organic molecule adsorption process was improved by the implementation of a pulsed magnetic general valve (see Chapter 3.1), installed outside of the cluster source. It was utilised for adsorption experiments on cationic tantalum clusters and offered better control of the adsorbate dosing process. By dosing aliphatic alcohols (MeOH, EtOH, 1-propanol) onto cationic tantalum clusters no molecular attachment of the alcohols was found but a significant size effect for adsorbed alcohol fragments was observed. These fragments were assigned to two main signal groups, **OH** and **$C_xO$**, which showed a strong even/odd effect depending upon the number of atoms per tantalum cluster (see Chapter 5.2). The OH signal showed a higher intensity compared to the $C_xO$ signal for even clusters and the reverse for odd clusters. Two competitive mechanisms could have caused these observations: a) **C-O bond cleavage** was favoured for even cluster sizes, which resulted in a higher abundance of tantalum hydroxide reaction products and b) **C-H bond cleavage**, caused by dehydrogenation reactions, which was favoured for odd cluster sizes and resulted in a higher abundance of $C_xO$ bound to the clusters.

With these results it is shown that the dosing of organic compounds onto metal clusters leads to the successful formation of cluster-adsorbate complexes in good yields. For experiments involving dosing aliphatic alcohols on tantalum clusters, significant size selectivity was found for every alcohol attempted. Two different reaction pathways were assigned to the corresponding signal groups, which might depend on electronic and/or geometric properties of the metal clusters.

**Photoionisation and photodetachment experiments** on tantalum and rhodium clusters were performed to study the potential for probing chiral metal clusters using laser spectroscopy. Non-resonant photoionisation of tantalum clusters was investigated using the third harmonic (355 nm) of a Nd:YAG laser (*Innolas Spit Light*, 120 mJ/pulse). The laser beam was guided into the TOF-MS chamber and irradiated the cluster beam between repeller and extractor electrode. To distinguish between ionised neutrals and cations coming from the cluster source, the circular electrode in front of the expansion nozzle was set to 70 V and deflected the nascent charged clusters from the cluster source. The ionisation yield increased for every considered cluster size by increasing the laser power per pulse. With a

wavelength of 355 nm (photon energy of 3.49 eV), multiphoton processes must have led to the observed ionisation of neutral clusters. By a double logarithmic plot of the integrated peak area of the individual cluster sizes against laser power, where the slope is an indication of the order of the multiphoton process, it was found that the neutral tantalum monomer underwent ionisation via a three photon process and the dimer by a two photon process. This is in good agreement with results of IPs found in literature.[42] For larger tantalum clusters the plot showed a slight discrepancy with the literature data, with the order measured to be one, instead of the expected two. This difference is assigned to the dissociation and fragmentation of these clusters at high laser powers of > 50 mJ/pulse, which leads to the measurement of ion signals that are lower than expected, when only the ionisation pathway is considered.

Photodetachment of anionic rhodium clusters by irradiation with 355 nm was performed between nozzle and skimmer in the cluster source vacuum chamber. Signal depletion of up to 50 % for $Rh_{13}^-$ was observed. By using a dye laser working with Coumarin 307, a wavelength scan (485-520 nm) at constant laser power of 6.6 mJ/pulse was performed. A clear trend in signal depletion depending on the wavelength and cluster size was observed, but the signal intensities were also found to decrease due to fluctuations of the cluster source output.

The performed adsorbate and spectroscopic experiments build the basis for further experiments, which should lead to the formation, characterisation and discrimination of chiral metal-adsorbate complexes. By achieving this goal a breakthrough in chiral recognition for heterogeneous catalysis would be realised. Further experiments with different organic compounds and evolution of the experimental setup are demanded to reach this goal.

The results presented in Chapter 5 showed that discrimination between the different adsorbate species attached to smaller metal clusters was feasible. For larger clusters the mass resolution of the TOF-MS was limited. Therefore, a first important step is the **installation of a reflectron** to increase the mass resolution, especially for larger species. The installation of the reflectron was performed after the experimental work for this thesis was completed. A reflectron is a type of TOF-MS that consists of an ion source, a field free drift region and an ion detector (see Chapter 2.1). The main difference from a linear TOF-MS is

the existence of a so-called ion mirror reflector in the Reflectron TOF-MS setup (see Figure 7.1). The ions penetrate the reflector after passing a field free drift region that follows the initial TOF-MS extraction stage. Ions with higher kinetic energy arrive first at the reflector but penetrate deeper into its electric field. This causes these ions to follow a longer path length within the reflector. Ions with lower kinetic energy arrive later at the reflector but penetrate less deeply, which leads to a shorter flight path. Due to these flight paths in the reflector, caused by reversing the direction of travel of the ions, ions with the same mass arrive simultaneously at the detector. The enhancement in mass resolution occurs due to an increase in the flight time of the ions and compensation of the initial kinetic energy distribution.[103]

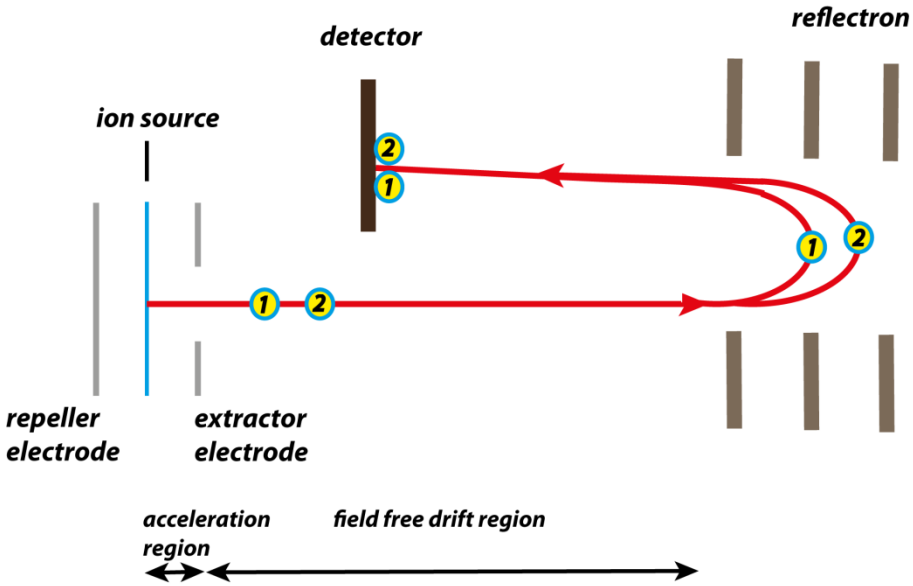


**Figure 7.1:** *Scheme of a Reflectron-TOF-MS with the ion mirror (reflectron), which reverses the initial extraction direction of the ions and accelerates them towards the detector.*

Due to the non-molecular adsorptions observed for many organic compounds, especially on tantalum clusters, a change of the metal target material is recommended to meet the goals of the project. First experiments with 2-butanol dosed onto cationic rhodium clusters showed a reduced reactivity to dehydrogenation and less fragmentation. Therefore, rhodium clusters might be a system that is well suited to perform **further adsorption experiments** on. An even less reactive metal target could be used instead, such as gold, which is the least reactive metal towards atoms or molecules.[104] Small gold clusters with less than 8 atoms were found to show almost no reaction for CO oxidation on surfaces[2].

Therefore, the dosing of organic compounds on small gold clusters in the gas phase could result in more molecular adsorption and less reaction pathways, such as dehydrogenation. Higher signal intensities for the cluster-adsorbate species could then be achieved, which is a fundamental need for future spectroscopy experiments. The results presented in Chapter 5 mostly involved primary alcohols as adsorbates, with a hydroxyl unit as the functional group. Other functionalities like amines or thiols are also of interest. Studies known from literature show that cationic rhodium clusters, especially $Rh_6^+$, show a high ability to activate NO. Up to four NO molecules were found to adsorb dissociatively on $Rh_6^+$.[88] Using the strong ability of rhodium clusters to bind nitrogen containing adsorbates could enhance the adsorption strength and might lead to a molecular attachment. Thiol containing ligands (i.e. 2-phenylethnethiol) are well known for the stabilisation of gold clusters in solution.[105] Introduction of thiol-containing adsorbates might be impeded by the low vapour pressures, but the use of an improved injection system, where the pulsed valve for example could lead to the formation of cluster-adsorbates with good yields.

To find a compound which offers a chiral structure, a sufficiently strong interaction with the clusters, molecular attachment, and a high vapour pressure, is the most challenging task for future studies.

In regards of **laser spectroscopy**, utilisation of resonant multiphoton ionisation (REMPI) spectroscopy to probe the metal-adsorbate species is the main goal. Compared to non-resonant photoionisation, resonant ionisations techniques, especially REMPI, are more often used in laser spectroscopy studies. REMPI is a species selective spectroscopic technique, because specific neutral intermediate states can be probed. Additionally, soft ionisation and controlled fragmentation are achievable.[21] The probability of ionisation is significantly higher than for non-resonant multiphoton processes, where higher laser power intensities are needed to achieve good signal to noise ratios for the ionised species.

One-colour two photon ionisation studies were performed on molecular complexes by *Filippi et al*.[23] These molecular complexes consisted of two chiral organic compounds (diastereomers). Differences in the spectral shift depending on the enantiomers used were observed.[23] By adapting this technique to the metal-adsorbate complexes the shift of the electronic state of the adsorbate caused by the interaction with the metal cluster could be investigated. It is thought that for two enantiomers of a chiral molecule a different

ionisation scheme applies, and therefore a difference in the spectral shift should be observed.

The metal-adsorbate complexes could also be probed by photodissociation spectroscopy. Discrimination between two enantiomers of chiral molecules adsorbed on the chiral metal cluster is feasible. Depending on the electronic and geometric structures of the clusters, one organic enantiomer might bind more strongly to one particular enantiomer of the chiral cluster than the other. Photodissociation followed by mass selection could then be used to produce an enantiomeric excess, which could in turn be used in further reactivity studies.

# 8. Bibliography


1. Mingos, D.M.P., Wales, D. J. *Introduction to cluster chemistry*. (Engelwood Cliffs, N.J., 1990).

2. Sanchez, A. *et al.* When Gold Is Not Noble : Nanoscale Gold Catalysts. *J. Phys. Chem.* **103,** 9573–9578 (1999).

3. Rupprechter, G. *Catal. Today* 1263 (2007).

4. Shiju, N. R. & Guliants, V. V. Recent developments in catalysis using nanostructured materials. *Appl. Catal. A Gen.* **356,** 1–17 (2009).

5. McCrea, K. R. & Somorjai, G. a. SFG-surface vibrational spectroscopy studies of structure sensitivity and insensitivity in catalytic reactions: cyclohexene dehydrogenation and ethylene hydrogenation on Pt (1 1 1) and Pt (1 0 0) crystal surfaces. *J. Mol. Catal. A Chem.* **163,** 43–53 (2000).

6. Wilson, O. M., Knecht, M. R., Garcia-Martinez, J. C. & Crooks, R. M. Effect of Pd nanoparticle size on the catalytic hydrogenation of allyl alcohol. *J. Am. Chem. Soc.* **128,** 4510 (2006).

7. Kore, A. R. & Shanmugasundaram, M. Highly stereoselective palladium-catalyzed Heck coupling of 5-iodouridine-5’-triphosphates with allylamine: a new efficient method for the synthesis of (E)-5-aminoallyl-uridine-5’-triphosphates. *Tetrahedron Lett.* **53,** 2530–2532 (2012).

8. Kardanpour, R. *et al.* Highly dispersed palladium nanoparticles supported on amino functionalized metal-organic frameworks as an efficient and reusable catalyst for Suzuki cross-coupling reaction. *J. Organomet. Chem.* **761,** 127–133 (2014).

9. Tada, M. & Iwasawa, Y. Advanced chemical design with supported metal complexes for selective catalysis. *Chem. Commun.* 2833 (2006).

10. Mertens, P. G. N. *et al.* Au0 nanocolloids as recyclable quasihomogeneous metal catalysts in the chemoselective hydrogenation of α,β-unsaturated aldehydes and ketones to allylic alcohols. *Catal. Today* **122,** 352–360 (2007).

11. Lorenzo, M. O. *et al.* Creating Chiral Surfaces for Enantioselective Heterogeneous Catalysis : R , R -Tartaric Acid on Cu ( 110 ). 10661–10669 (1999).

12. Tamura, M. & Fujihara, H. Chiral bisphosphine BINAP-stabilized gold and palladium nanoparticles with small size and their palladium nanoparticle-catalyzed asymmetric reaction. *J. Am. Chem. Soc.* **125,** 15742–3 (2003).

13. Izumi, Y. *Adv. Catal.* 215 (1983).

14. Webb, G., Wells, P. B.. *Catal. Today* **12,** 319 (19992).

15. Sawai, K., Tatumi, R., Nakahodo, T. & Fujihara, H. Asymmetric suzuki-miyaura coupling reactions catalyzed by chiral palladium nanoparticles at room temperature. *Angew. Chem. Int. Ed. Engl.* **47,** 6917–9 (2008).

16. Gautier, C. & Bürgi, T. Chiral N-isobutyryl-cysteine protected gold nanoparticles: preparation, size selection, and optical activity in the UV-vis and infrared. *J. Am. Chem. Soc.* **128,** 11079–87 (2006).

17. Hofer, W. a., Humblot, V. & Raval, R. Conveying chirality onto the electronic structure of achiral metals: (R,R)-tartaric acid on nickel. *Surf. Sci.* **554,** 141–149 (2004).

18. Bürgi, T. & Baiker, A. Heterogeneous enantioselective hydrogenation over cinchona alkaloid modified platinum: mechanistic insights into a complex reaction. *Acc. Chem. Res.* **37,** 909–17 (2004).

19. Lechtken, A. *et al.* $Au_{34}^-$: a chiral gold cluster?, *Angew. Chem. Int. Ed. Engl.* **46,** 2944–8 (2007).

20. Santizo, I. E., Hidalgo, F., Pe, L. A., Noguez, C. & Garzo, I. L. Intrinsic Chirality in Bare Gold Nanoclusters : The $Au_{34}^-$ Case. *J. Phys. Chem.* 17533–17539 (2008).

21. Boesl, U., Bornschlegl, A., Logé, C. & Titze, K. Resonance-enhanced multiphoton ionization with circularly polarized light: chiral carbonyls. *Anal. Bioanal. Chem.* **405,** 6913–24 (2013).

22. Li R., Sullivan R., Al-Basheer W., Paqni R.M., C. R. N. Linear and nonlinear circular dichroism of R-(+)-3-cyclopentanone. *J. Chem. Phys.* **125,** 144304 (2006).

23. Filippi, A. *et al.* Chiral discrimination of monofunctional alcohols and amines in the gas phase. *Int. J. Mass Spectrom.* **210-211,** 483–488 (2001).

24. Zehnacker, A. *Chiral recognition in the Gas Phase*. (Taylor and Francis Group, 2010).

25. Boesl, U., Ba, C. & Ka, R. Time-of-flight mass analyser for anion mass spectrometry and anion photoelectron spectroscopy. *Int. J. Mass Spectrom.* **206,** 231–244 (2001).

26. Wiley, W. C. & McLaren, I. H. Time-of-Flight Mass Spectrometer with Improved Resolution. *Rev. Sci. Instrum.* **26,** 1150 (1955).

27. Boesl, U., Weinkauf, R., Weickhardt, C. & Schlag, E. W. Laser ion sources for time-of-flight mass spectrometry. *Int. J. Mass Spectrom. Ion Process.* **131,** 87–124 (1994).

28. J.M. Hollas. *Modern Spectroscopy*. (Wiley, 2010).

29. J.W. Rabalais. *Principles of ultraviolet photoelectron spectroscopy*. (Wiley, 1977).

30. Beltrán, M. R. *et al.* Ab initio and anion photoelectron studies of $Rh_n$ (n = 1 − 9) clusters. *Eur. Phys. J. D* **67,** 63 (2013).

31. Harding, D. J. *et al.* Probing the structures of gas-phase rhodium cluster cations by far-infrared spectroscopy. *J. Chem. Phys.* **133,** 214304 (2010).

32. Da Silva, J. L. F., Piotrowski, M. J. & Aguilera-Granja, F. Hybrid density functional study of small $Rh_n$ (n=2−15) clusters. *Phys. Rev. B* **86,** 125430 (2012).

33. Weck, P. F., Kim, E., Poineau, F. & Czerwinski, K. R. Structural evolution and properties of subnanometer $Tc_n$ (n = 2-15) clusters. *Phys. Chem. Chem. Phys.* **11,** 10003–8 (2009).

34. Fielicke, A., Ratsch, C., von Helden, G. & Meijer, G. The far-infrared spectra of neutral and cationic niobium clusters: $Nb_5^{0/+}$ to $Nb_9^{0/+}$. *J. Chem. Phys.* **127,** 234306 (2007).

35. Kietzmann, H. *et al.* Photoelectron Spectra and Geometric Structures of Small Niobium Cluster Anions. *Phys. Rev. Lett.* **77,** 4528–4531 (1996).

36. Kietzmann, H., Morenzin, J., Bechthold, P. S., Ganteför, G. & Eberhardt, W. Photoelectron spectra of $Nb_n$ clusters: Correlation between electronic structure and hydrogen chemisorption. *J. Chem. Phys.* **109,** 2275 (1998).

37. Lineberger,W.C. , Ervin, K.M. , Ho, J., *J. Chem. Phys.* **30,** 6987 (1990).

38. Knickelbein, M. B. & Yang, S. Photoionization studies of niobium clusters: Ionization potentials for $Nb_2$–$Nb_{76}$. *J. Chem. Phys.* **93,** 5760 (1990).

39. Wu, Z. J., Kawazoe, Y. & Meng, J. Geometries and electronic properties of $Ta_n$, $Ta_nO$ and $TaO_n$ (n=1–3) clusters. *J. Mol. Struct. THEOCHEM* **764,** 123–132 (2006).

40. Gruene, P., Fielicke, A. & Meijer, G. Experimental vibrational spectra of gas-phase tantalum cluster cations. *J. Chem. Phys.* **127,** 234307 (2007).

41. Fa, W., Luo, C. & Dong, J. Coexistence of ferroelectricity and ferromagnetism in tantalum clusters. *J. Chem. Phys.* **125,** 114305 (2006).

42. Callings, B. A., Rayner, D. M. & Hackett, P. A. Ionization potentials of tantalum clusters with three to 64 atoms ’. *Int. J. Mass Spectrom. Ion Process.* **125,** 207–214 (1993).

43. Wang, B., Zhai, H.-J., Huang, X. & Wang, L.-S. On the electronic structure and chemical bonding in the tantalum trimer cluster. *J. Phys. Chem. A* **112,** 10962–7 (2008).

44. Aguilera-Granja, F., Balbás, L. C. & Vega, a. Study of the structural and electronic properties of $Ru_N$ clusters (N < 20) within the density functional theory. *J. Phys. Chem. A* **113,** 13483–91 (2009).

45. Calamincini,P., Vasquez-Perez, J. M. A density functional study of $Rh_{13}$. *Can. J. Chem.* **91,** 591–597 (2013).

46. Jackson, P., Fisher, K. J. & Willett, G. D. The catalytic activation of primary alcohols on niobium oxide surfaces unraveled : the gas phase reactions of $Nb_xO$ clusters with methanol and ethanol. *Chem. Phys.* **262,** 179–187 (2000).

47. Sievers, M. R., Chen, Y.-M. & Armentrout, P. B. Metal oxide and carbide thermochemistry of $Y^+$, $Zr^+$, $Nb^+$, and $Mo^+$. *J. Chem. Phys.* **105,** 6322 (1996).

48. Berg, C. *et al.* Effect of charge upon metal cluster chemistry: Reactions of $Nb_n$ and $Rh_n$ anions and cations with benzene. *J. Chem. Phys.* **108,** 5398 (1998).

49. He, S.-G., Xie, Y., Dong, F. & Bernstein, E. R. Reaction of niobium and tantalum neutral clusters with low pressure, unsaturated hydrocarbons in a pickup cell: from dehydrogenation to Met-Car formation. *J. Chem. Phys.* **125,** 164306 (2006).

50. Buckner, S. W., Macmahon, T. J., Byrd, G. D. & Freiser, B. S. Gas-Phase Reactions of Nb and Ta with Alkanes and Alkenes. *Ionorganic Chem.* **28,** 3511–3518 (1989).

51. Zemski, K. a., Bell, R. C. & Castleman, a. W. Reactions of Tantalum Oxide Cluster Cations with 1-Butene, 1,3-Butadiene, and Benzene. *J. Phys. Chem. A* **104,** 5732–5741 (2000).

52. Cox, D. M., Reichmann, K. C., Trevor, D. J. & Kaldor, A. CO chemisorption on free gas phase metal clusters. *J. Chem. Phys.* **88,** 111 (1988).

53. Tian, F.-Y. & Shen, J. Density-functional study of CO adsorbed on $Rh_N$ (N = 2–19) clusters. *Chinese Phys. B* **20,** 123101 (2011).

54. Parry, I. S. *et al.* Collisional activation of $N_2O$ decomposition and CO oxidation reactions on isolated rhodium clusters. *J. Phys. Chem. A* **117,** 8855–63 (2013).

55. Harding, D., Ford, M. S., Walsh, T. R. & Mackenzie, S. R. Dramatic size effects and evidence of structural isomers in the reactions of rhodium clusters, $Rh_n^{+/-}$, with nitrous oxide. *Phys. Chem. Chem. Phys.* **9,** 2130–6 (2007).

56. Adlhart, C. & Uggerud, E. C-H activation of alkanes on $Rh^+_n$ (n=1-30) clusters: size effects on dehydrogenation. *J. Chem. Phys.* **123,** 214709 (2005).

57. Adlhart, C. & Uggerud, E. Mechanisms of catalytic dehydrogenation of alkanes by rhodium clusters $Rh_n^+$ probed by isotope labelling. *Int. J. Mass Spectrom.* **249-250,** 191–198 (2006).

58. Robbins, E. J., Leckenby, R. E. & Willis, P. The ionization potentials of clustered sodium atoms. *Adv. Phys.* **16,** 739–744 (1967).

59. Henkes, W. *Zeitschrift Fur Naturforsch. Part a-Astrophysik Phys. Und Phys. Chemie* **16,** 842 (1961).

60. Leckenby, R.E., Trevalion, P.A., Robbins, E. J. *Proc. R. Soc. London Ser. a-Mathematical Phys. Sci.* **280,** 409 (1964).

61. Grabar, K. C., Freeman, R. G., Hommer, M. B. & Natan, M. J. Preparation and Characterization Monolayers. **67,** 1217–1225 (1995).

62. Dietz, T. G. Laser production of supersonic metal cluster beams. *J. Chem. Phys.* **74,** 6511 (1981).

63. Heiz, U., Vanolli, F., Trento, L. & Schneider, W.-D. Chemical reactivity of size-selected supported clusters: An experimental setup. *Rev. Sci. Instrum.* **68,** 1986 (1997).

64. Proch, D. & Trickl, T. A high-intensity multi-purpose piezoelectric pulsed molecular beam source. *Rev. Sci. Instrum.* **60,** 713 (1989).

65. Judai, K., Sera, K., Amatsutsumi, S., Yagi, K. A soft-landing experiment on organometallic cluster ions : infrared spectroscopy of V $(benzene)_2$ in Ar matrix. **334,** 277–284 (2001).

66. Echt, O., Dao, P. D., Morgan, S. & Castleman, A. W. Multiphoton ionization of ammonia clusters and the dissociation dynamics of protonated cluster ions. *J. Chem. Phys.* **82,** 4076 (1985).

67. D. Dao, S. Morgan and A.W. Castleman Jr., Resonance-Enhanced Multiphoton Ionization of Van Der Waals molecules, *Chem. Phys. Lett.* **111,** 38-46(1984).

68. Kerns, K. P., Guo, B. C., Deng, H. T., Jr, A. W. C. & Castleman, A. W. Collision induced dissociation of titanium – carbon cluster cations. *J. Chem. Phys.* **101,** 8529 (1994).

69. Bergeron, D. E., Jones, N. O., Khanna, S. N. Association of $C_3H_6$ to aluminum cluster anions. *Chem. Phys. Lett.* **415,** 230–233 (2005).

70. Kooi, S. E., Dehydrogenation of ammonia by early transition metals : formation of metal nitride clusters. *Chem. Phys. Lett.* **315,** 49–54 (1999).

71. Deng, H. T., Kerns, K. P., Bell, R. C., Oxidation induced ionisation and reactions of metal-carbide clusters. *Int. J. Mass Spectrom. Ion Process.* **168,** 615–625 (1997).

72. Cox, D. M., Reichmann, K. C., Trevor, D. J., Kaldor, A. CO chemisorption on free gas phase metal clusters. *J. Chem. Phys.* **88,** 111 (1988).

73. Cox, D.M., Trevor, D.J., Whetten, R.L., Kaldor, A. Aluminum Clusters: Ionization Thresholds and Reactivity toward Deuterium, Water, Oxygen, Methanol, Methane, and Carbon Monoxide. *J. Phys. Chem.* 421–429 (1988).

74. Zakin, M.R., Cox, D.M., Kaldor, A. Reaction of Niobium Clusters withe Benzene. *J. Phys. Chem.* **91,** 5224–5228 (1987).

75. Powers, D. E., Hansen, S. G., Geusic, M. E., Michalopoulos, D. L. & Smalley, R. E. Supersonic copper clusters. *J. Chem. Phys.* **78,** 2866–2881 (1983).

76. Hinterberger, F. Ion optics with electrostatic lenses, S. 27–44

77. Sievers, M. . & Armentrout, P. . Gas phase activation of carbon dioxide by niobium and niobium monoxide cations. *Int. J. Mass Spectrom.* **179-180,** 103–115 (1998).

78. Kiessig, H., Essmann, U. *Scr. Metall.* **19,** (1985).

79. Zemski, K. A., Bell, R. C. & Jr, A. W. C. Reactivities of tantalum oxide cluster cations with unsaturated hydrocarbons. *Int. J. Mass Spectrom.* **184,** 119–128 (1999).

80. Wu, Q. & Yang, S. Reactions of niobium cluster ions $Nb^{+}_{x}$ ( x б 2 – 16 ) with $NO_2$ and NO . *Int. J. Mass Spectrom.* **184,** 57–65 (1999).

81. *Compr. Anal. Chem.* **30,** 695–698 (1996).

82. http://en.wikipedia.org/wiki/Tantalum.

83. Budoace, S. *et al.* Chemoselective oxidation of 2-thiomethyl-4,6-dimethyl-pyrimidine on nanostructured tantalum oxides. *Catal. Today* **91-92,** 219–223 (2004).

84. Kumar Yadav, M. & Mookerjee, A. Nitrogen absorption and dissociation on small Tantalum clusters. *Phys. B Condens. Matter* **405,** 3940–3942 (2010).

85. Nemana, S. & Gates, B. C. Silica-supported tantalum clusters: catalyst for alkane conversion. *Chem. Commun. (Camb).* 3996–8 (2006). doi:10.1039/b608794a

86. Sakurai, M., Watanabe, K., Sumiyama, K. & Suzuki, K. Magic numbers in transition metal (Fe, Ti, Zr, Nb, and Ta) clusters observed by time-of-flight mass spectrometry. *J. Chem. Phys.* **111,** 235 (1999).

87. Wang, H. *et al.* Absorption and Raman spectroscopy of mass-selected tantalum tetramers in argon matrices. *J. Chem. Phys.* **103,** 3289 (1995).

88. Ford, M. S. *et al.* Reactions of nitric oxide on $Rh_6^{+}$ clusters: abundant chemistry and evidence of structural isomers. *Phys. Chem. Chem. Phys.* **7,** 975–80 (2005).

89. Uh, Y.-S. *et al.* Rhodium phosphino-enolate complexes as chemo- and regioselective catalysts for the hydroformylation of styrenes. *J. Organomet. Chem.* **695,** 1869–1872 (2010).

90. Falcon, M., Farnetti, E. & Marsich, N. Stereoselective polymerization of phenylacetylene promoted by rhodium catalysts with bidentate phosphines. *J. Organomet. Chem.* **629,** 187–193 (2001).

91. http://en.wikipedia.org/wiki/Acetone.

92. Deng, H. T., Kerns, K. P. & Castleman, A. W. Formation , Structures , and Reactivities of Niobium Oxide Cluster Ions. *J. Phys. Chem.* **3654,** 13386–13392 (1996).

93. Zakin, M. R., Cox, D. M. & Kaldor, A. Reaction of Niobium Clusters with Benzene-$h_6$ and -$d_6$ : Evidence for Cluster-Induced Dehydrogenation. *J. Phys. Chem.* 5224–5228 (1987).

94. http://en.wikipedia.org/wiki/Ethanol.

95. http://en.wikipedia.org/wiki/2-butanol.

96. Comelli, G., Scpa, S. T., Park, A. S., Trieste, B. & Tascinfm, L. Oxygen and nitrogen interaction with rhodium single crystal surfaces. *Surf. Sci. Rep.* 165–231 (1998).

97. http://en.wikipedia.org/wiki/Limonene.

98. http://en.wikipedia.org/wiki/Pulegone.

99. Hwang, C.-P., Yeh, C.-T. & Zhu, Q. Rhodium-oxide species formed on progressive oxidation of rhodium clusters dispersed on alumina. *Catal. Today* **51,** 93–101 (1999).

100. Nasirzadeh,K.,Zimin, D. Vapor-Pressure Measuremnets of Liquid Solutions. *Journaol Chem. English Data* **49,** 607–612 (2004).

101. Kamiguchi, S. & Chihara, T. Catalytic dehydration of alcohol to olefin and ether by halide clusters of Nb , Mo , Ta and W possessing an octahedral metal core. *Catal. Letters* **85,** 97–100 (2003).

102. Zakin, M. R., Brickman, R. O., Cox, D. M. & Kaldor, a. Dependence of metal cluster reaction kinetics on charge state. I. Reaction of neutral ($Nb_x$) and ionic ($Nb^+_x$, $Nb^-_x$) niobium clusters with $D_2$. *J. Chem. Phys.* **88,** 3555 (1988).

103. Boesl, U., Weinkauf, R. & Schlag, E. W. Review Reflectron time-of-flight mass spectrometry and laser excitation for the analysis of neutrals , ionized molecules and secondary fragments. **112,** 121–166 (1992).

104. Hammer, B., Norskov, J. K. Why gold is the noblest of all the metals. *Nature* **376,** 238–240 (1995).

105. Farrag, M., Tschurl, M., Dass, A. & Heiz, U. Infra-red spectroscopy of size selected $Au_{25}$, $Au_{38}$ and $Au_{144}$ ligand protected gold clusters. *Phys. Chem. Chem. Phys.* **15,** 12539–42 (2013).

# 9. Appendix

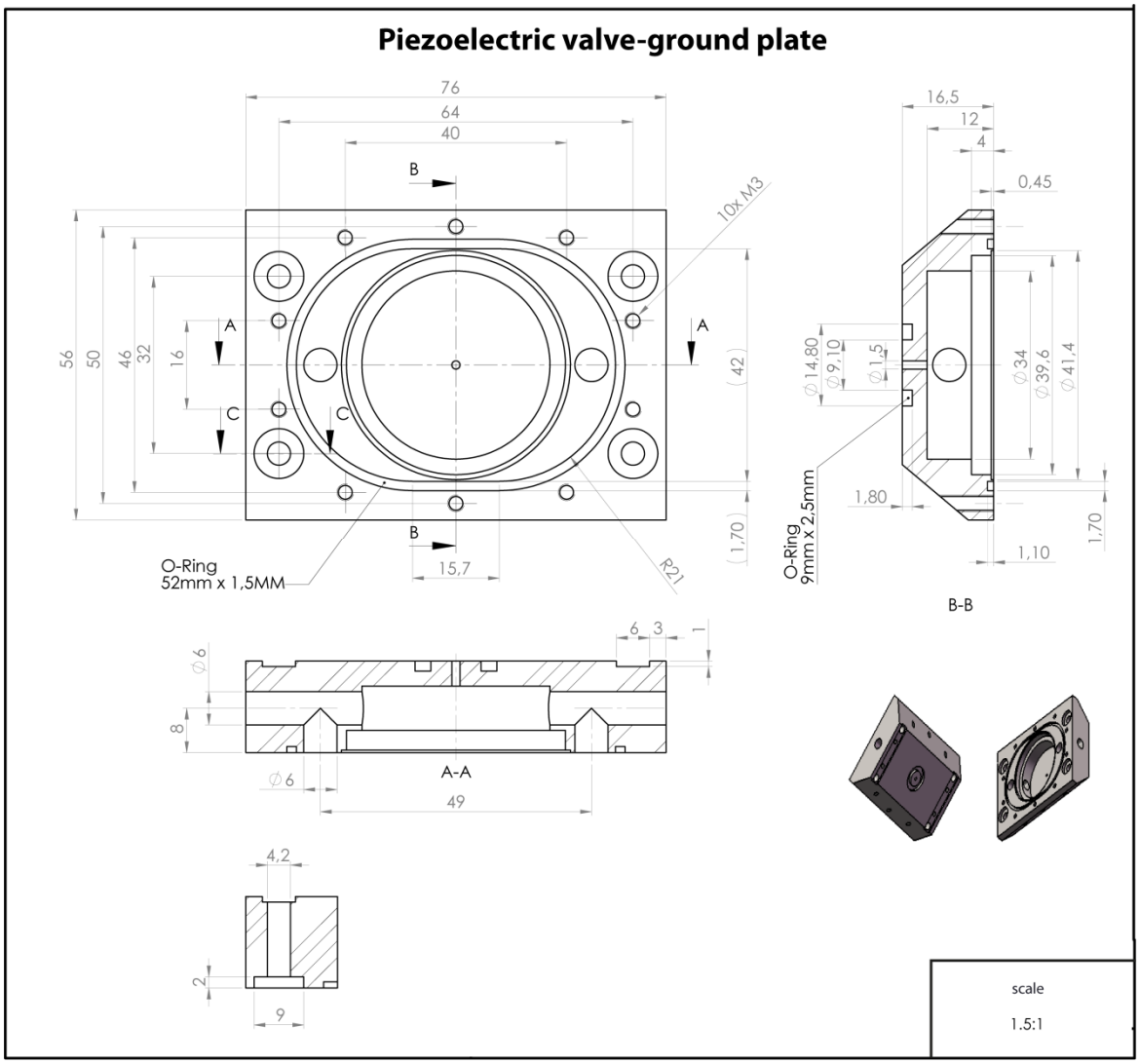
Piezoelectric valve-ground plate
76
64
40
B
10x M3
A
C
56
50
46
32
16
42
1,70
O-Ring
52mm x 1,5MM
15,7
R21
16,5
12
4
0,45
O-Ring
9mm x 2,5mm
1,80
1,10
1,70
B-B
6
3
1
8
A-A
49
4,2
2
9
scale
1.5:1

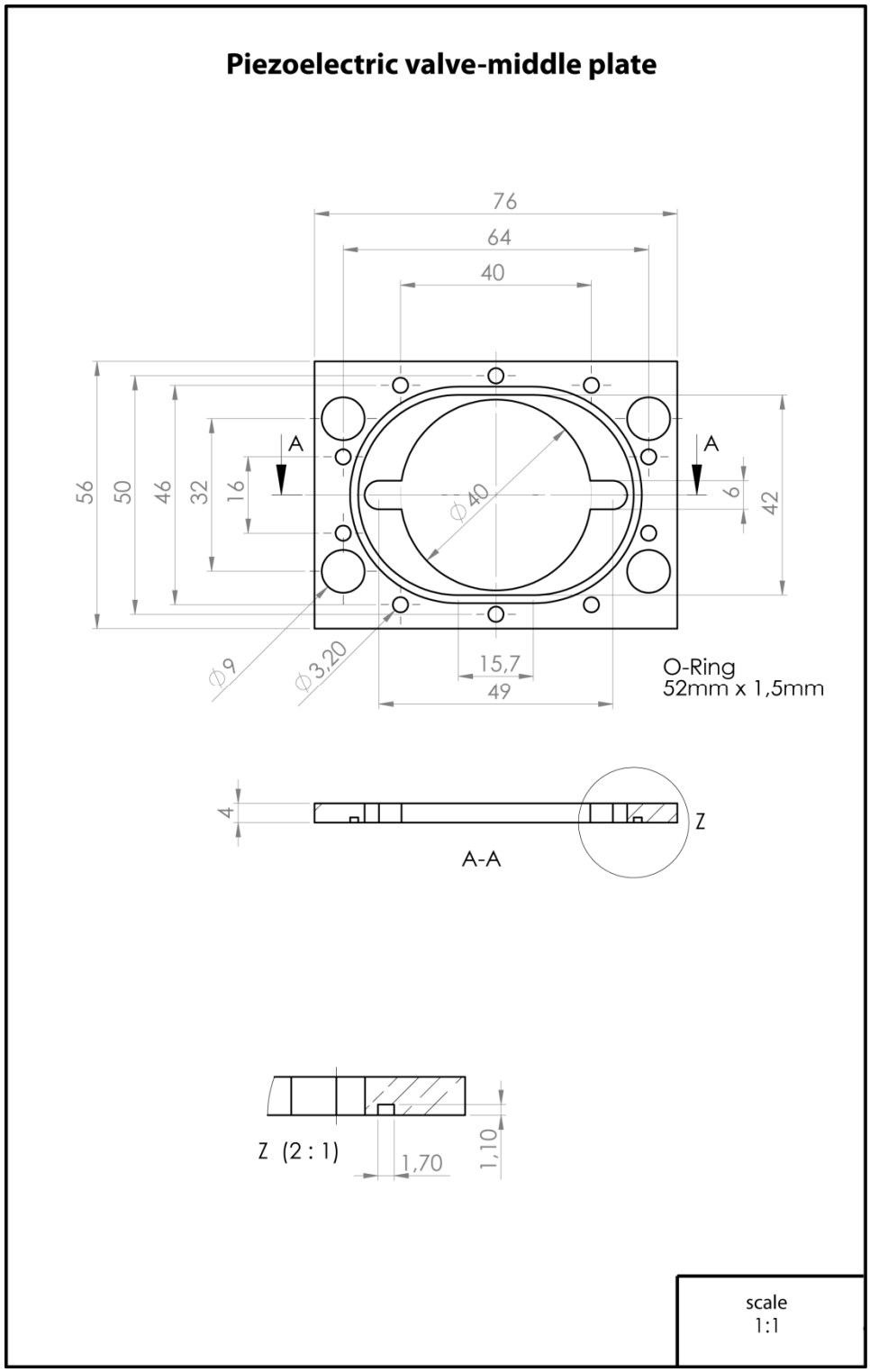
Piezoelectric valve-middle plate
76
64
40
56
50
46
32
16
A
A
6
42
Ø40
Ø9
Ø3,20
15,7
49
O-Ring
52mm x 1,5mm
4
Z
A-A
Z (2 : 1)
1,70
1,10
scale
1:1

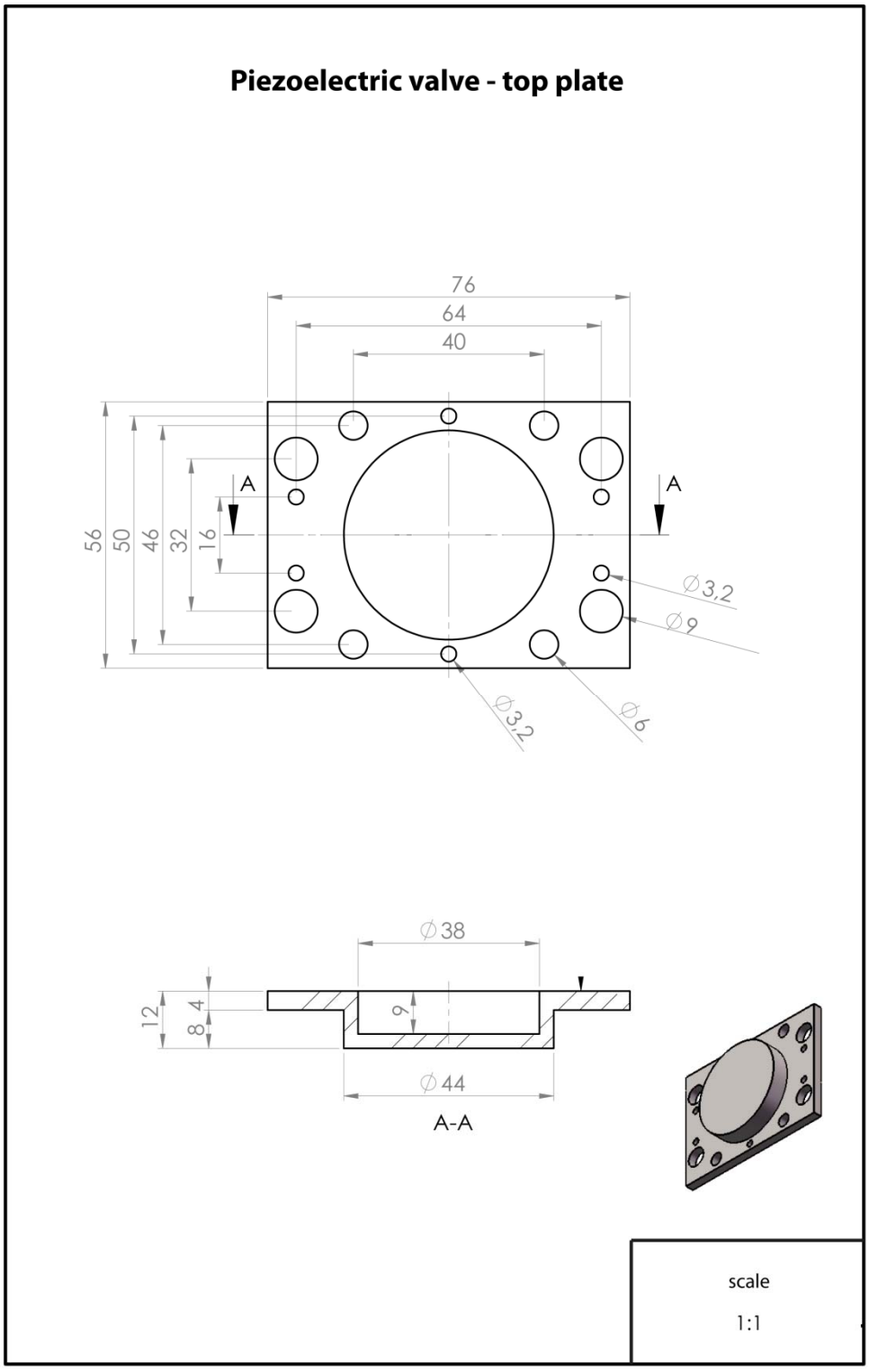
Piezoelectric valve - top plate
76
64
40
A
A
56
50
46
32
16
∅3,2
∅9
∅3,2
∅6
∅38
12
8
4
9
∅44
A-A
scale
1:1

## Circular electrodes for ion deflection

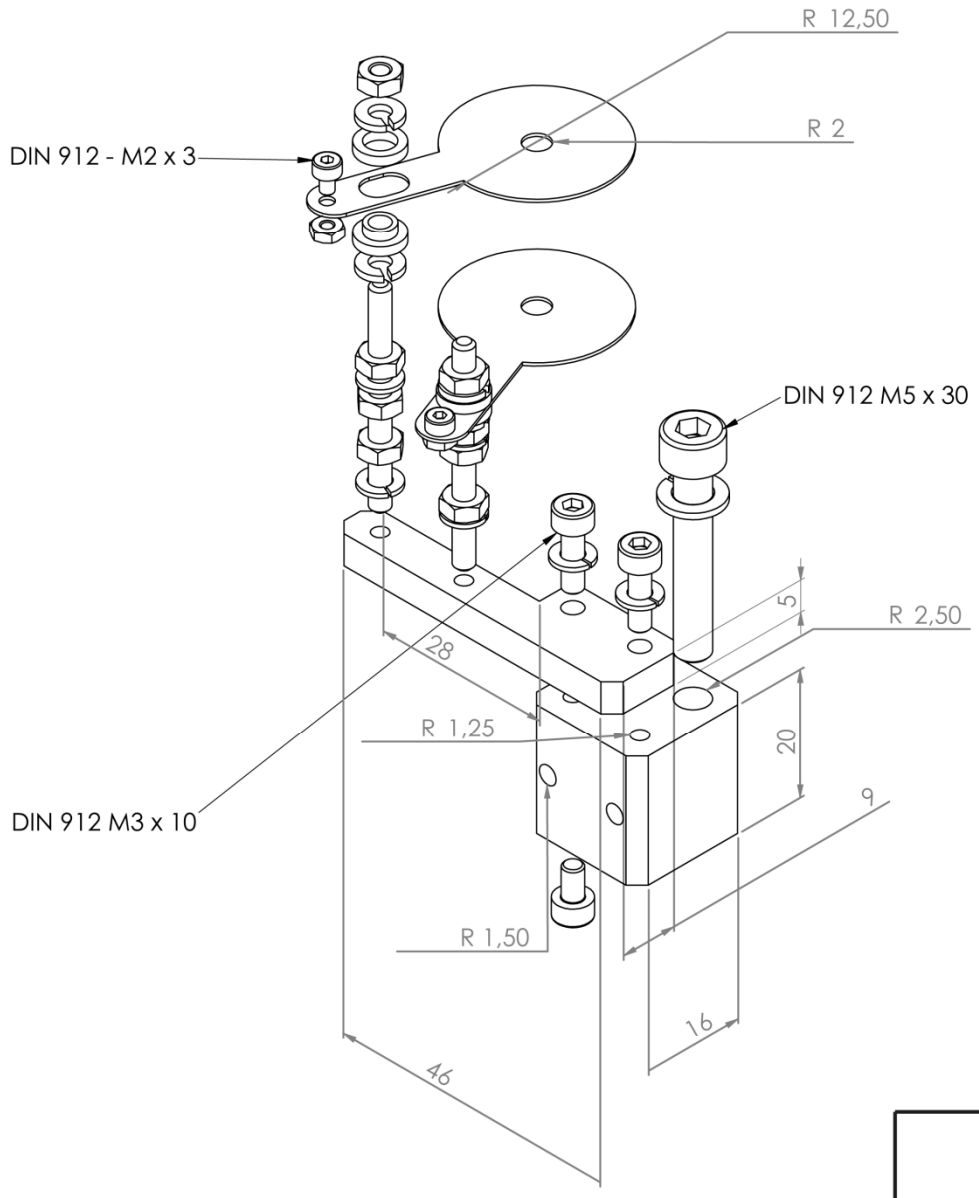


scale

1.5:1